The Frontier of Modern Calorimetry: Hardware Advances and Application in Particle Physics Analysis

Tatiana Medvedeva

A Dissertation
Presented to the Faculty
of Princeton University
in Candidacy for the Degree
of Doctor of Philosophy

Recommended for Acceptance
by the Department of
Physics
ADVISER: Christopher G. Tully

September 2014

Abstract

While the last missing components of the SM puzzle seem to be successfully found, particle physicists remain hungry for what might be there, beyond the cosy boundaries of the well studies elementary particle world. However, the sophisticated technique of data analysis and acute Monte Carlo simulations remain fruitless. It appears that the successful intrusion into the realm, in which we were not welcome so far, may require a very different implication of effort. All those results might suggest, though banal, that we need an improvement on the hardware side. Indeed, the hadronic calorimeter of CMS is no competitor to its other state-of-art components. This obstacle in many cases significantly complicates the flow of the physics analysis. Besides, the era of high luminosity LHC operation in the offing is calling for the same. After exploration of the analysis debri with 8 TeV collision data, we investigate various approaches for better calorimetry for the CMS detector.

Acknowledgements

This work would have been unthinkable without many people who supported and guided me over the years.

First of all, I would like to express my deep gratitude to my advisor, Christopher Tully, for numerous things I've learned from him as well as for his attentive guidance throughout many years of my work in Princeton High Energy Experiment team. I am especially grateful for lifting the veil on research and development in detector technology.

My further education and progress in this field would not be possible without Arjan Heering, Dmitri Konstantinov and Dragoslav-Laza Lazic. I have also learned a lot from the discussions with Christian Joram, Thomas Schneider and Miranda Van Stenis. My knowledge of accelerators and experience with beam lines would not be possible without the expertise of Per Grafström, Lau Gatignon and Ilias Efthymiopoulos. I am very grateful to Andrea Benaglia, Marco Lucchini and Kristof Pauwels for pleasant and productive collaboration and express my deep gratitude to Etiennette Auffray and Paul Lecoq for their invaluable insight and guidance. I was lucky to work side by side with too many outstanding physicists to list here. I am thankful to the members of the SUSY Physics Analysis Group of the CMS experiment, as I've learned a great deal from them. I owe my knowledge of calorimeters to many experts of the electromagnetic and hadronic calorimeter teams.

The years I've spent at CERN I was delighted to share a pleasant and friendly atmosthere of the big Princeton office with Edmund Berry, Phil Hebda, Davide Gerbaudo, Edward Laird, Paul Lujan, Michael Mooney, Xiaohang Quan, Halil Saka and Andrzej Zuranski.

I would also like to thank Kimberly Dawidowski who was a lifesaver in so many practical matters. I am grateful to the administrators of Physics Department, Jessica Heslin,

Regina Savadge and Karen Kelly for their help with numerous issues without which this work would not have been completed. I also owe gratitude to Daniel Marlow and Pierre Piroue who were offering a helping hand in a broad spectrum of life situations. I am thankful to Sune Jakobsen for his readiness to discuss the broad variety of technical subjects, including my – sometimes crazy – hardware-related ideas.

Finally, I would like to take advantage of an oppotunity to thank my friends for their invaluable support. In particular I am thankful to (in alphabetical order) Dmitry Chechenev, Denis Derkach, Anastasia Dolya, Olga Driga, Viacheslav Duk, Dmitry Dylov, Maria Filippova, Nikolay Groshkov, Tatiana and Maxim Gouzevitch, Vadim Jelezniakov, Anton Karneyeu, Mikhail Kirsanov, Irina and Oleksiy Kononenko, Viktoriya Kononova, Maxim Konyushikhin, Konstantin Kravtsov, Uliana Makarova, Ekaterina Mehnert, Vasily Pestun, Olga and Yury Polyanskiy, Yaroslava Profantilova, Andrei Rachkov, Roman Rafikov, Eugene Sedykh, Anastasia Solodko-Magazinik and Evgeny Solodko, Roman Sorokoletov, Nikolai Yampolsky, Konstantin Zhukov. I was incredibly lucky to have them all by my side.

Contents

Chapter 1

Introduction

Particle physics predates all other branches of physics since the fundamental building blocks of matter have been of great interest to people for ages. As early as in the 5^{th} century B.C. Greek phylosophers have already proposed an idea of "atoms" as elementary, indivisible constituents of all material objects. But ever since the understanding of the origins of matter have barely evolved and this realm of physics remained in almost embryonic state. Thus even though the atomistic theory was not only widely accepted but also strongly supported with the discoveries in the realm of chemistry, it was not until the last decade of the 19^{th} century that the first truly elementary particle has been detected[1].

This discovery proved that the atoms are not the smallest imperishable constituents of matter and set an important milestone in the development of physics. In subsequent decades many experimental advances and observations and theoretical breakthroughs provided a solid ground for developing a self-consistent paradigm of fundamental particles

[1] In 1896 J. J. Thomson and his colleagues have measured the mass and the electric charge of "cathode particles" - electrons - and showed that their charge to mass ratio was independent of cathode material. In 1906 Thomson was awarded the Nobel Prize in Physics for the discovery of the electron and for his work on the conduction of electricity in gases.

and interactions – the Standard Model.

1.1 Standard Model

The Standard Model summarizes modern vision of the realm of fundamental elementary particles and interactions. It is built as a synthesis of special relativity and quantum mechanics and forms a renormalizable relativistic quantum gauge field theory. Fundamental particles are hence interpreted as excitations of relativistic quantum fields (bosonic and fermionic), and their behaviour is governed by the Lagrangian which is a function of those fields.

The roles of fermionic and bosonic fields are different. While fermions form ordinary matter, bosons of spin 1 are the mediators of fundamental interactions - weak, electromagnetic and strong. Gravity is not incorporated into the model, yet theoretical considerations suggest that it should be mediated by massless quanta of gravitational field of spin 2, gravitons[1].

The Standard Model includes 12 fermions of spin $\frac{1}{2}$. For every particle there is a corresponding antiparticle which possesses the same mass and spin, but opposite charges. It is convenient to aggregate the fermions into three groups called generations which exhibit similar proterties. Each generation then consists of four particles: two quarks with fractional electric charges of $+\frac{2}{3}$ and $-\frac{1}{3}$ and two leptons with integral electric charges equal to -1 and 0. Charged leptons are electron (e^-), muon (μ^-) and tau-lepton (τ^-). Neutral leptons are called neutrinos (ν_e, ν_μ, ν_τ) and are massless. Each member of higher generation has a greater mass than the corresponding member of the lower generation(s). Higher generation charged particles are unstable and ultimately decay into particles of the first generation which are stable and hence form all ordinary matter.

The mediators of fundamental interactions, 12 gauge bosons of the model, are all spin 1 particles.

Photons (γ) are the carriers of the electromagnetic force affecting all electrically charged

[1] Gravitons have to be massless, since gravitational forces are effective over an unlimited range. The spin value follows from the fact that it is the stress-energy tensor that gives rise to gravity which this is a second-rank tensor.

particles. They are massless in full accord with infinite action range of electromagnetic forces. All fermions but neutrinos interact electromagnetically.

The $W^{\pm}$ and Z^0 bosons mediate the weak interaction, their masses are quite significant (80.4 and 91.2 GeV, respectively) and account for the short range of the weak interaction. Both leptons and quarks interact by means of weak forces, in other words, all fermions possess a quantum number, related to the weak interaction – the weak isospin. Since weak interaction admits not only neutral current (Z^0 exchange), but also charged currents ($W^{\pm}$ exchange), they hence admit the change of fermion flavors[1].

The strong interaction is caused by the exchange of electrically neutral massless gluons. Quarks are the only fermions which carry a threefold color charge (anti-quarks carry corresponding anti-color charges) and hence participate in the strong interaction. Due to phenomenon of color confinement quarks do not exist as free particles but rather are bound into color singlet combinations, hadrons. There are two options for forming a color singlet state: three quarks (or antiquarks) with different color charges form a baryon or quark-antiquark pair with color-anticolor charges makes up a meson.

Because of a threefold nature of a color charge there exist 9 possible combinations of color charge-anticharge pairs for the interaction carriers, but there is one linear combination of those which is color-symmetric and hence the number of interaction carriers is reduced to eight gluons[2]. Since gluons themselves possess color charge not only they mediate the interaction, but, unlike photons, can also be its source: gluons can be emitted and absorbed by other gluons.

If one attempts to build a consistent gauge field theory which includes exclusively the above mentioned fields, the only way to succeed is to put up with the fact that all gauge bosons in the model are massless particles: the addition of add hoc mass terms into the Lagrangian would spoil the gauge invariance and make theory non-renormalizable. While there is nothing wrong with massless interaction carriers for electromagnetic and strong forces, one cannot go along with it in case of weak interaction. The generally acknowledged

[1] Strictly speaking, SM allows for the flavor-changing neutral currents (FCNCs) too, but only beyond the tree-level, and such processess are strongly suppressed by the GIM mechanism.

[2] Such symmetric combination is a color singlet. Hadrons, formed by quarks, are color singlets too and can only interact with other color singlets. So, if color singlet gluons existed, there have to be a long-range strong interaction by means of such gluons, but as we know, strong interactions are short-range.

method to cure this problem is to introduce a scalar field that permeates all space and whose vacuum state does not share the symmetry of the Lagrangian, leading to spontaneous symmetry breaking. It is this phenomenon that is not only responsible for the non-zero masses of $W^{\pm}$ and Z^0 bosons, but also gives rise to the massive scalar Higgs boson(s). Once introduced into the model, Higgs field can interact with the fermionic fields and thereby generate fermion masses[1].

This mass generation mechanism is justified by the experiment: while electromagnetic and weak interactions are revealed very differently on an everyday energy scale, once the energy exceeds the "unification energy" which is of the order of $100\,\mathrm{GeV}$, they appear to be a single unified electroweak interaction with four gauge bosons: $W^{\pm}$, W^0 of weak isospin and B^0 of weak hypercharge. The spontaneous symmetry breaking results in amalgamation of the W^0 and B^0 bosons into Z^0 boson, and photon γ:

$$\begin{pmatrix} \gamma \\ Z^0 \end{pmatrix} = \begin{pmatrix} \cos\theta_W & \sin\theta_W \\ -\sin\theta_W & \cos\theta_W \end{pmatrix} \begin{pmatrix} B^0 \\ W^0 \end{pmatrix},$$

where θ_W is the Weinberg angle. From this mixing between W^0 and B^0 it follows, that the mass of a neutral boson Z^0 differs from that of $W^{\pm}$: $m_Z = \frac{m_W}{\cos\theta_W}$.

The Standard Model is so far the most precisely tested theory in history. Such discoveries of great importance as neutral currents (1973, Gargamelle experiment at CERN), bottom quark (1977, E288 experiment at Fermilab), observation of $W^{\pm}$ and Z^0 bosons (1983, UA1 and UA2 experiments at CERN) and measurement of their masses, top quark (1995, CDF and D$\emptyset$ experiments at Fermilab), tau neutrino (2000, DONUT experiment at Fermilab) with the observation of a Higgs boson in 2012 as the grand finale are all falling into the list of SM predictions.

And yet the Standard Model cannot pretend to be a complete theory of fundamental interactions. To begin with it fails to incorporate gravity. It does not provide an explanation for matter-antimatter imbalance in the Universe - a so called baryon asymmetry problem. There is no satisfactory dark matter candidate in the model to account for the non-baryonic

[1] Fields of matter are Yukawa-coupled to the Higgs field; once the spontaneous symmetry breaking occurs, each Yukawa term is split in two parts – the true interaction term and the fermion field mass term.

matter. It does not accomodate the phenomenon of the accelerating expansion of the Universe. There is no mechanism to generate neutrino masses. Aside from the questions beyond the scope of the Standard Model it also suffers from the internal problems. It contains 19 external parameters which cannot be calculated. Those are usually taken to be 9 fermionic masses, 3 coupling constants, 4 parameters of the quark mixing matrix, masses of Z and H and a phase allowing for the violation of a combined charge-conjugation and parity-inversion symmetry in strong interactions. Not only we don't understand what dictates the values of those parameters, but the span of parameters over 32 orders of magnitude gives rise to hierarchy problem and inconsistency with aesthetical naturalness principle. This broad list of drawbacks of the existing working model persistently intensifies the déjà vu of the "Nineteenth Century clouds" of Lord Kelvin encouraging the search for possible extensions and generalizations of the Standard Model.

1.2 Beyond the SM

1.2.1 Grand Unified Theories (GUT)

After the successul unification of weak and electromagnetic interactions, the possibility of further unification with strong interaction was a very natural assumption.

According to the Grand Unified Theories based on that idea, strong, weak and electromagnetic interactions are merged into a single fundamental interaction above a certain energy scale of the order of $\sim 10^{15}$ GeV[1]. At the energies above that threshold the gauge couplings α_S, α_W, α_{em} become equal to a unique gauge coupling α_{GUT}. Ultra-massive quanta of the field of this universal interaction, X, set the scale of GUT, M_X: above that scale this gauge symmetry is unbroken, while below it undergoes spontaneous breaking and gauge couplings evolve independently.

Precise values of the GUT scale vary from theory to theory, but one thing remains

[1]However, it is worth mentioning that this number comes from the extrapolation of running gauge couplings to the point of their unification which is many orders of magnitude away from the energy scale currently studied. Therefore such estimates of GUT scale strongly rely on an assumption that new unknown processes do not come into play, as this would affect the evolution of the gauge coupling and hence the GUT scale as well.

unshakable: the energies corresponding to the Grand Unification are not only outside the reach of the accelerators for any foreseeable future, but are also unheard of as it comes to the cosmic rays – the ultimate source of highest energy particles. However, the processes governed by the unified interaction should exhibit themselves at the whole range of energies. Even though this gauge symmetry is strongly broken at the accessable energy range, it should mix quark and leptons by means of their interactions with gauge bosons of the GUT field. As a consequence the transitions between quarks and leptons would be possible and imply non-conservation of baryon and lepton numbers.

The important signature of GUT is the decay of the proton. The predictions for lifetime of protons depend on the model with typical values of the order of 10^{30} years. Hence an experiment in search of such events should be sensitive to single acts of such decays within the hundred of tons of monitored material.

The Grand Unification is attractive not only due to the elegance of underlaying concept, but also due to impressive results in predicting some values the SM fails to predict. For instance, the simplest GUT based on $SU(5)$ symmetry follows the value of $\cos^2\theta_W$, parameter of the electroweak theory, which cannot be derived from the SM and is determined from experimental data. The same unification model also predicts the values of electrical charges of quarks and the difference in the electric charge among the leptons of the same generation.

But GUT did not evade their intrinsic problems. The presence of two mass scales, M_W and M_X, separated by many orders of magnitude gives rise to the hierarchy problem. The mass of the Higgs boson corresponding to electroweak symmetry breaking should be on the mass scale M_X for the cancellation of diagrams in perturbation theory to happen at sufficiently low energy to satisfy unitarity. In its turn, the Higgs particle of symmetry breaking at GUT scale is responsible for giving the mass M_X to the bosons of GUT and hence should posess the mass of the order of M_X. To achieve such hierarchy of vacuum expectation values, the parameters of a scalar potential would have to be fine-tunned with a breathtaking accuracy in each and every order of perturbation theory, which seems unplausible.

1.2.2 Supersymmetry (SUSY)

Hierarchy problem can be elegantly solved if the corrections coming from boson and fermion loop diagrams cancel out. This is possible in case if bosons and fermions have identical couplings to the Higgs boson and implies a boson-fermion symmetry – supersymmetry, which is broken on the habitual everyday energy scale.

In its simplest form SUSY requires doubling the number of particles of the SM: each SM particles acquires a superpartner: a particle with the same electric, weak and strong charges, but with the spin differing by half a unit.

All supersymmetric particles are denoted by the tilde. Superpartners of SM fermions are named by prefixing the names of particles with s: squarks $\widetilde{q}$, sleptons $\widetilde{l}$ (selectrons $\widetilde{e}$, etc.), sneutrinos $\widetilde{\nu}$. The names of SM bosons end with "-ino": wino $\widetilde{W}^{\pm}$, $\widetilde{W}^{0}$, bino $\widetilde{B}$, higgsino $\widetilde{H}$. After electroweak symmetry breaking, wino, zino and photino are not the mass eigenstates. Neutral gauginos mix with neutral higgsinos to form four neutralinos $\widetilde{\chi}_i^0$. Charged winos mix with charged higgsinos to form two charginos $\widetilde{\chi}_i^{\pm}$. The common convention is that the mass of charginos and neutralinos increases with the index. At the same time three of eight degrees of freedom of the Higgs field become longitudinal modes of $W^{\pm}$ and Z^0 bosons, and the other five form Higgs scalars h^0, H^0, A^0 and $H^{\pm}$.

However, SUSY by construction does not require baryon and lepton number conservation. To impose such property, the SUSY model has to obey the conservation of R-parity, which can be defined as follows:

$$P_R = (-1)^{3(B-L)+2s} \quad ,$$

where B and L represent baryon and lepton numbers, respectively, and s is the spin. Therefore all SM particles and all Higgs bosons have even R-parity, while sparticles have odd. Not only R-parity eliminates baryon and lepton number violation, but it also ensures that all the interaction vertices involves an even number of sparticles. In particular, the sparticles are pair-produced in collisions of particles and all non-stable sparticles decay into an odd number of sparticles. As the lightest supersymmetric particle (LSP) cannot decay into SM

particles in accord with this requirement, it should be stable. If this particle is electrically neutral, it also makes a candidate for dark matter.

Chapter 2

Input of the HEP Studies – What Do We See?

Armed with the theoretical description of the elementary particle zoo, one now has to apply this knowledge to the observables, provided by the experiment. Unfortunately some properties of particles cannot be measured directly, others strongly rely on our knowlendge of their other properties. Hence for the species of particle to be determined, the simultaneous presence of several various detectors in the setup is required. Even the members of the same four-momentum vector, energy and three-momentum of the particle, require two fundamentally different ways of measuring.

While precise determination of the energy implies that the particle is completely stopped by the material of the detector and the energy discharged is collected, momentum measuring is conducted based on the curvature of the charged particle's trajectory in the magnetic field and hence benefits from the minimal impact on the particle. From this point of view all detectors can be characterized as performing destructive or (almost) non-destructive

measurements.

The first challenge is thus the decision about the combination and order of the detectors in which they would provide the most information and as far as possible wouldn't harm all the other ongoing measurements.

The direct detection is only possible for (electrically) charged particles and is based on ionization or excitation of the atoms of the detector material by the passage of charged particles or the radiation those particles emit under certain circumstances. The neutrals are registered only mediately, based on their interactions, which give rise to charged particles.

The main components of a general purpose hermetic detector are covered below.

2.1 Biometrics of Individual Particles

The information from different particle detectors does not come in terms of properties of particles and global characteristics of an event. In its raw form it is a collection of signals from many of the readout channels of the detectors of different nature. A many-stage reconstruction process is required to aggregate it into high-level compound objects. Let's follow the same logic and start by considering the systems which allow to reconstruct the basic characteristics of individual particles.

2.1.1 Trackers: Charge and Momentum

Measurements of particles' charge and momentum are based on the Lorentz force which in the presence of constant magnetic field compels electrically charged particles to deflect from straight lines and follow helical trajectories. The direction of the trajectory curving then suggests the sign of electical charge the outgoing particle possesses and the momentum measurement comes from the curvature of track, which has to be reconstructed. In general case the helical trajectory is defined by five parameters; they are to be defined from the spartial coordinates of those channels along the particle trajectory which happened to detect its interaction with the material of the detector. Since many particles are traversing the volume of the detector at the same time, the hits that neighbouring tracks leave behind should be associated with the proper tracks for the correct reconstuction, and increasing

the number of channels would simplify such pattern-recognition problem. There is however a trade-off. As it was mentioned above, momentum measurements require minimal impact on the particle's properties, and therefore independently on what particular kind of detector technology is used for the tracker, whether it is wire chamber of some kind or a semiconductor-based sensor, the amount of the material in the tracker should be minimized. The main source of energy loss by electrons and positrons in matter is Bremsstrahlung: as a result of a Coulomb interaction with the electric fields of the atomic nuclei, electrons and positrons emit photons. Depending on the energy and direction of the emitted photon, the radiating particle itself undergoes more or less substantials deviation from the initial trajectory – multiple scattering. This process hence contributes a constant term (A) into a fractional transverse momentum resolution of a tracking system. The second term is proportional to the momentum of the particle and comes from the finite resolution of the track curvature (C). For the particles with very high momentum their trajectories will appear in the tracking system as straight lines, which cannot be used to determine the curvature and hence the momentum. The overall fractional resolution for the transverse momentum hence can be expressed as:

$$\frac{\sigma_{p_T}}{p_T} = A \oplus C \cdot p_T.$$

2.1.2 Calorimeters

As it was mentioned above, measurement of energy is a destructive measurement, which results in stopping the particle in the material of a detector – calorimeter. For this reason the measurement of the energy is conducted after the measurement of the momentum is done, i. e. the calorimeters are positioned behind the tracking system. The characteristic scale for the electromagnetic interaction is set by the radiation length, X_0, which defines how far on average an electron, positron or photon travel through the given material before going through the interaction process. The interaction of hadrons with matter at the same time is characterized by the nuclear interaction length, λ_I.

Electromagnetic Calorimeters

If the tracker presents less that one radiation length of the material to the outgoing particles, then the first acts of Bremsstrahlung and pair production, which are the dominant processes of electron, positron and photon interaction with matter at high energies, will occur in the electromagnetic calorimeter, then those processes will repeat with all the particles in the cascade, which still have sufficient energy for the multiplication. In a simplified model of such electromagnetic cascade, when the energy is split in half between the daughter particles in a multiplication process, the number of particles will basically double after every radiation length of the material. Once the energy of individual particles drops below the multiplocation process threshold, the number of particles in the cascade starts to go down, as now particles loose energy by other means and are shortly fully stopped in the material. The depth of the material required to stop a particle is then a logarithmic function of the energy of a particle. Therefore, an electromagnetic calorimeter with the depth of 15-30 X_0 should be sufficient for most of the applications. The transverse dimensions of electromagnetic shower are given by the Molière radius, which is commonly defined as a radius of a cylinder in which 90% of the electromagnetic shower is deposited and is expressed as:

$$R_M = 0.0265\, X_0 \cdot (Z + 1.2).$$

While all electrically charged particles interact electromagnetically and hence can loose energy through the same radiative processes as electrons and positrons, those radiative losses are negligible for heavier particles, as the radiation length scales like a squared mass of the incident particle. Therefore, already for a muon, which is roughly 200 times heavier than an electron, a single act of Bremsstrahlung would require on average traversing the depth of the material which is $\sim$40000 thicker than what is required for an electron. Therefore it does not make any sense to even attempt stopping muons in the electromagnetic calorimeter. Hadrons, which are also sufficiently heavier than electrons, also barely interact within the electromagnetic calorimeter by means of the described above mechanisms.

The formation of the electromagnetic cascade is a random process, and the number of

particles in the cascade will fluctuate as the square root of the number of particles. This gives rise to a stochastic term (S) in a fractional energy resolution, which is inversely proportional to the square root of the energy. Other contributions to the fractional energy resolution come from the electronics noise (N) of the channels contributing to the energy calculation (inversely proportional to energy) and from the systematic, or constant, term (C), which reflects the intrinsic non-uniformities of the detector and any inaccuracy in inter-calibration of the channels. The overall fractional energy resolution can then be expressed as:

$$\frac{\sigma_E}{E} = \frac{S}{\sqrt{E}} \oplus \frac{N}{E} \oplus C.$$

Electromagnetic calorimeters can be either completely made of a sensitive material, such as heavy scintillating crystals or Cherenkov radiators (homogeneous calorimeter), or out of layers of heavy material – absorber – interleaved with layers of sensitive material, such as plastic scintillators (sampling calorimeters).

For heavy materials the approximations for radiation and nuclear interaction lengths are:

$$X_0\ \rho = 120\,\frac{g}{cm^2}\,Z^{-\frac{2}{3}},$$

$$\lambda_I\ \rho = 37.8\,\frac{g}{cm^2}\,A^{0.312}.$$

For many of the heavy crystals used as active materials the X_0 has values of the order of 1 cm, while the nuclear interaction length, λ_I, is signifficantly larger (compare for example 0.89 cm and 20.3 cm for $PbWO_4$, 1.12 cm and 22.3 cm for BGO crystals)[1]. In case if the depth of the material will not exceed one nuclear interaction length, the hadrons impinging through the electromagnetic calorimeter will not loose much energy there, while electrons, positrons and photons will be fully stopped. Hence the name "electromagnetic". The electrons and positrons can then be identified by the energy deposits they produce in the electromagnetic calorimeter with the charged track in the tracking system pointing to those energy clusters. Photons, as they do not possess electrical charge, do not produce signals

[1] In general case this is however not true. For example for the concrete used for shielding this difference is barely a factor four: $X_0 = 11.55\,cm$, $\lambda_I = 42.39\,cm$.

in the tracking system and are identified as solitary energy clusters in the electromagnetic calorimeter.

Hadronic Showers and Calorimeters

Hadrons, although start loosing energy in electromagnetic calorimeters[1], and can produce some signal there, deposit most of their energy in the hadronic calorimeter that follows.

At first glance development of a hadronic and electromagnetic showers may seem very much alike. Indeed, in both cases particles, produces by the governing interaction, can further loose energy by ionization losses or in the new acts of multiplication processes. Hence, the number of particles in the cascade keeps on growing for several interaction lengths. Later on, as the energy of individual particles in the cascade drops below critical energy, the absorbtion of particles in the material leads to decreasing the particle multiplicity. But the very nature of strong interactions results in tremendous complexity of hadronic showers compared to electromagnetic ones.

First of all, while strong interaction processes have no analog in the development of the electromagnetic shower, hadronic showers do contain electromagnetic showers developed by decaying π^0 and η.

Besides while in electromagnetic cascades all energy deposited in the calorimeter is eventually used to ionize the absorbing material and hence can be measured, hadronic showers deposit a significant fraction of its energy in a fundamentally undetectable form, and its fraction fluctuates in a very wide range from event to event.

As this phenomenon has important consequences for hadron calorimetry, let's discuss it in more detail.

As a hadron projectile traverses the detector medium, it encounters the atomic nucleus and initiates a spallation process. The incoming particle undergoes a series of collisions with nucleons inside of the nucleus. In its turn those nucleons collide with the others. In the acts of collisions pions and other hadrons are produced. Hence the intra-nuclear cascade of fast nucleons develops; some of those showering particles escape the atom and

[1] As it follows from the numbers and formulas above, electromagnetic calorimeters normally present about one nuclear interaction length of material for projectiles.

contribute into the visible part of the hadronic shower, while others get caught inside of the nuclear boundary and loose the excess energy by distributing it among other nucleons. The nucleus which ends up in an excited state undergoes a slow de-excitation process by means of ”evaporation” of several nucleons. The remaining excitation energy, which is less than binding energy of a single nucleon, is dumped in form of γ radiation.

The binding energy of the nucleons, released in this process, cannot be measured. The second source for undetectable energy is introduced by the leptonic decay of π and K mesons, when the energy is carried away by the neutrinos and muons.

Those two mechanisms contribute to the so-called invisible energy. On average it accounts for 30-40% of the non-electromagnetic energy of the shower. One of the immediate consequences for calorimeters is that the calorimeter response to hadrons (h) is lower than that for the photons and electrons (e). The invisible energy fluctuates in a wide range, depending on the underlying processes in the hadronic shower development. As a result, the energy resolution of the hadronic calorimeters is sufficiently, roughly an order of magnitude, worse than that of the electromagnetic ones.

The calorimeters with $\frac{h}{e} < 1$ are referred to as non-compensating. As non-compensation causes many undesired effects, there have been many attempts to overcome this problem. One of the approaches is a controlled degrading of the electomagnetic response by using the low Z cladding of the absorber layers, which results in stopping a fraction of low energy γ's. Another approach was based on selective increase of the energy deposits from the hadronic showers by introducing depleted uranium (^{238}U) as an absorber: nuclear fission would contribute extra energy to the non-electromagnetic part of the shower, primarily as soft neutrons and nuclear γ's[1]. However a more elegant approach suggests the use read-out by two systems with signifficantly different $\frac{e}{h}$ [2]. So far this approach was exploited in full only by the DREAM collaboration[3].

2.1.3 Muon Detectors

As it was described above, muons do not loose much energy in the calorimeters. They do not interact strongly, as for the electromagnetic interactions, the radiation length for the

muons is somewhat 40000 larger than that for electrons. With the typical materials used for the calorimeters it would then require hundreds of meters of detector depth. Muons pass through the entire traking and calorimetric systems experiencing only minimum ionizing energy losses which add-up to about 2 GeV in total. Therefore the main goal of the muon system is to register the particle escaping from the calorimeters and, as far as possible, contribute into the tracking hence improving the resolution of the central tracking system.

2.2 Collective Information

Although individually reconstructed particles provide a lot of information about the event, some compound objects also deserve apt attention. Below there is a description of a few of them of special importance.

One or several of the detector subsystems described above are used in construction of those objects.

2.2.1 Vertexing – Back to the Origin

In high energy experiments one of the most important characteristics of the particles' interaction is the position of the interaction point (IP), or primary vertex. Even for fixed target experiments the IP position is not constant and varies from event to event with transverse position within the beam spot of a high energy beam on the target and longitudinal position depending on the material of the target and the energy of the incident beam. In a colliding beam experiment the position of the IP is delimited by the region of beam crossing[1].

Not only precise determination of the IP simplifies reconstructing the trajectories of the outcoming particles, but also it is important for other reasons. First of all, in high luminosity machines several interactions can take place during a single bunch crossing, and if in case of Tevatron experiments it was a few, ATLAS and CMS detector at the LHC witness a couple of dozens and more. It is therefore very important to segregate particles originating from different interactions; and it is the easiest to do so by tracking them back

[1] The size of the beam crossing region in turn depends not only on the size of the bunches, but also on the conditions of their crossing, such as the use of crab cavities for bunch rotation.

to the origin. One more good motivation is the potential for heavy flavor identification. As for B-mesons $c\tau_B < 500\,\mu$m, a decay of its b-quark will typically happen only few millimeters away from the IP. This would produce a secondary vertex. The detector for IP measurements should therefore possess appreciable spatial resolution, but nonetheless cannot be placed so close to the beam.

Typical vertex detector is made of several layers of silicon pixel sensors, providing several 3D-measurements for impinging particles. At the same time, as those sensors are thin enough, they do not introduce too much of the material on the way of particles and do not corrupt the momentum measurement by tracking systems. Once extrapolated into the interaction region, the hits left in the vertex detector by two of more particles provide measurements of primary and secondary vertices with the required precision.

2.2.2 Undetectables

Neutrinos are electrically neutral and weakly interacting. They can be exclusively detected by dedicated experiments operating with large volumes of material and patiently awaiting for extremely rare events of neutrino interaction with matter. But at general purpose detectors they escape detection by all of the subsystems. However some information about neutrinos (and other weakly interacting non-SM particles, if those happen to be produced in the event) is retained in the form of a transverse energy imbalance, $\overrightarrow{\not{E}}_T$. It is basically the negative of the vector sum of the transverse momenta of all the particles in the detector. However, more sophisticated calculation schemes can be employed to improve the resolution.

2.2.3 Jets

Jets reveal the strongly interacting partonic origin of the final state particles and hence grant an insight into short distance dynamics. Jets are clusters of particles produced in the hadronization of the initial partons – quarks and gluons – and moving in the similar direction.

The longitudial momentum of a jet is defined by the initial parton, while transverse

momenta of the final state hadrons is mainly due to the soft processes and thus remains small, which leads to collimated structure of the jets. While there is a certain flexibility in the definition of jet, it still has to be treated with caution. To begin with, the partons which give rise to the jets are color-charged, while the final state particles are not. Hence there can be no unique association between the former and the latter. If one wishes to employ the apparatus of perturbative QCD for calculation of jet-related quantites, such as cross sections, then definitions of the jets should be insensitive to the effects of soft particles emission and collinear splittings. In addition, the definition and treatment of jets depends on the type of colliding particles.

Electron-positron and hadron-hadron collisions

The global event structure is quite different in case of electron-positron and hadron-hadron collisions. Since the whole initial state in case of electron-positron collision is purely electromagnetic, all particles of the final state can be associated with the hard scattering process.

This is not the case for hadron-hadron collision where only one parton from each incident hadron participates in the hard scattering. As a result the final state contains the products of soft interactions of the remaining partons (underlying event) along with the particles originating from hard scattering process and initial state Bremsstrahlung from the partons participating in the hard scattering. The underlying event along with this initial state radiation form the so called "beam jets" composed by particles with small transverse momenta. This intrinsic difference between the event structure in e^+e^- and hadron-hadron collisions has of course to be accounted for when the definition of jets is given in both cases.

Jets in electron-positron collisions

The electron-positron collisions feature rotational invariance. Hence the natural choice of variables to operate with are the polar angles (θ_i, ϕ_i) and energies E_i. Since there is no underlying event envolved, every final state particle is associated uniquely with one of the jets. One then studies the exclusive cross sections – the production of exactly n jets and

nothing else.

First jet related studies were conducted for back-to-back events in e^+e^- collisions, where the finding of an axis of the event was sufficient. Therefore what served as a first handle for jet reconstruction, was a collection of variables defining the shape of the event.

For each event one can calculate a sphericity tensor:

$$S^{\alpha\beta} = \sum_i p_i^\alpha p_i^\beta / \sum_i |\mathbf{p}_i|^2,$$

where α and β run over the three space coordinates, and i over all reconstructed particles. As this tensor is normalized, the sum of its eigenvalues equals unity.

If now $\lambda_1 \geq \lambda_2 \geq \lambda_3 \geq 0$ are the eigenvalues of this tensor, then sphericity is defined as $S = \frac{3}{2}(\lambda_3 + \lambda_2)$. Sphericity is close to 1 for spherical events, it is approximately 3/4 for flat events and tends to zero for collinear events. The aplanarity is defined as $A = \frac{3}{2}\lambda_3$. A is small for coplanar, and in particular collinear event topologies.

Despite providing a clear signature of a back-to-back topology, the above mentioned event-shape variables are not fully satisfactory – in the first place, because of the quadratic form of the original tensor. This form leads to exaggerated effects from the contributions of unusually fast particles and is unsafe against collinear splittings – a collinear quark-gluon pair would contribute to this tensor differently than a single quark with the same momentum. Variables which are linear in particle momenta do not reveal such shortcomings.

Thrust, one of such variables, is defined as follows:

$$T = \max_{\mathbf{n}_T} \frac{\sum_i |\mathbf{p}_i \cdot \mathbf{n}_T|}{\sum_i |\mathbf{p}_i|},$$

where the numerator is maximized over directions of the unit vector $\mathbf{n}_T$ and the sum is taken over all final-state hadron momenta p_i (whose three-vectors are $\mathbf{p}_i$ and energies are E_i). The resulting $\mathbf{n}_T$ is known as the thrust axis. In the limit of two narrow back-to-back jets $T \to 1$, while its minimum value of 1/2 corresponds to events with a uniform distribution of momentum flow in all directions.

The search for gluon's manifestation as three-jet events at PETRA and further studies

of those events after successful discovery of gluon jets in 1979, required a satisfactory measure of three-jet topology. Such shape variables can be constructed by generalization of the thrust variable. A dedicated variable, titled tri-jettiness, was also introduced in [4]. However, the complexity of corresponding algorithms grows dramatically with the number of jets and the generalization to the case of higher jet-multiplicities becomes less evident.

Therefore jet finding was further developed in a different direction. Instead of asigning a set of variables to the entire event and then discriminating it by their means as satisfying of non-satisfying the n-jet hypothesis, a pattern-recognition approach was adopted, which allowed instead to identify individual jets and compute various jet-related quantities for further implementation in the analysis.

The algorithms for jet finding in this case naturally use a set of reconstructed particles, or tracks and calorimetric clusters, as input pseudo-jets and then merge those proto-jets based on some measure of closeness. Two techniques for jet finding, which significantly differ, are of the cone-finding type and sequential clustering type.

The algorithm would then iterate the procedure, using the newly formed compound pseudo-jets for further merging, reducing the number of proto-jets by one at a time. The process is repeated until it either ends up with a set of jets which are separated better that a pre-defined separation value (number of final jets is not fixed), or achieves a grouping of all reconstructed hadrons into exactly n sets – final jets for n-jet imposed topology.

Jets in hadron-hadron collisions

While all the jet-reconstruction algorithms for hadron-hadron colliders have their roots in one or another algorithm from the e^+e^- experiments, it is important to keep in mind that despite many similarities, there are also significant differences between these two situations, and they have to be respected for the successful migration of the algorithm.

In the case of hadron-hadron collisions, rotational invariance is no longer present. In fact, since every parton only carries a fraction of the total momentum of the original hadron, the center of mass reference frame (CMRF) of the partons participating in the hard scattering is moving along the beam direction with respect to the CMRF of colliding hadrons. Then a logical choice of variables which emphasizes the invariance under boosts along the

beam direction includes pseudo-rapidity $\eta = -\ln(\tan(\theta/2))$, azimuthal angle ϕ and transverse momenta p_T (or the corresponding transverse energy $E_T = E\sin\theta$). An attempt to work with the exclusive cross section of n-jet production, similar to the case of e^+e^- events, would inevitably require dealing with the beam jets of the underlying event which is usually undesirable. Therefore it is reasonable to measure the inclusive cross sections of high p_T jet production instead.

Below is the brief overview of the jet algorithms.

Cone-Based Algorithms

The forebear of all cone-based algorithms was proposed in the work [5] by defining two back-to-back jets as collections of particles within a pair of back-to-back cones with a certain angular openning, which carried $1-\epsilon$ or higher fraction of the energy in the event. It was free of any ambiguity due to infrared radiation or collinear splitting. It was useful therefore for the theoretical versus experimental comparison of di-jet production. However it was impossible to adopt for the case of arbitrary jet multiplicity, which gave rise to the whole cohort of cone-based definitions, many of which were adopted by experiments at hadron machines.

Fixed-cone approach is the simplest implementation of a cone-finding idea. It takes the hardest particle in the event and uses it as an axis of a cone of a fixed aperture; then all the particles inside of this cone are assigned to the same jet. The procedure is then repeated with the hardest particle which is not yet assigned to any of the jets. It is possible, that some of the cones derived with this procedure can overlap. One of the possible cures for this complication is a progressive removal (PR) approach: once the cone is formed, all its constituents are removed from the event before the search for the new cone starts. This approach, obviously, suffers from collinear splitting unsafety: if some hard particle undergoes collinear splitting, then the order (and hence the content) of the cones might change.

Iterative-cone approach , on the opposite, does not fix the axis of the jet to the most energetic particle and are more flexible in this respect. The seed track only defines the initial cone. Then the momentum of all the particles, contributing to the cone, is calculated (normally as a simple vector sum), and the axis of the cone is moved to match the direction of the integral momentum. As the cone moves, some particles escape it, while some others now fall into geometical acceptance. On each stage the momentum is recalculated. The cycle continues until the cone becomes stable. The same mechanism of PR can be employed to avoid ambiguous particle assignement. Collinear unsafety is present here as well. Instead of PR, one can make use of the ”split-merge” (SM) or ”split-drop” (SD) approaches to cure the overlapping cones. In a nutshell, the idea is, for the overlapping cones to calculate the fraction of energy of the less energetic cone, which is due to the shared particles, and if it is above some threshold, merge the cones into one jet, else either split shared particles between the jets based on the proximity to the jet (SM) or assign all shared particles to the harder jet and discard all others (SD). This kind of cone separation technique, however, introduces the infrared unsafety. Partial recovering from infrared unsafety can be achieved by including the middlepoint search: after all the stable cones are found based on the set of seeds, use middlepoints between the pairs of stable cones as seeds for extra cones. However, it does not solve the problem completely, and so far there are no seeded cone-based algorithms which would be completely free of both infrared emittion and collinear splitting unsafety.

Seedless cone algorithm, which does not start with a particular set of seeds, but instead finds all possible stable cones, would be free of the IRC-unsafety: collinear splitting do not have any effect at all, as the order of cone finding is irrelevant, and the emission of soft particles would only lead to formation of extra cones with no hard particles in them. However, for a long time these kinds of algorithms were not applicable for events with a large number of particles, as the computation time was an exponential function of particle multiplicity. Only recently the solution which takes polynomial time, was found. It is currently implemented in the SISCone algorithm[6].

Succesive Recombination Algorithms

LUCLUS LUCLUS is probably the oldest of the algorithms still in use. Based on binary joining with additional preclustering and particle reassignment, it was introduced in 1983[7].

It starts by identifying the most energetic particle, which is used as a seed to form a cluster (of pre-defined size) around it. After that the procedure is repeated with all the particles not assigned to clusters. After the preclustering step is done, the clusters are merged based on the closeness measure:

$$y_{ij} = \frac{2|\boldsymbol{p}_i|^2|\boldsymbol{p}_j|^2(1-\cos\theta_{ij})}{(|\boldsymbol{p}_i|+|\boldsymbol{p}_j|)^2 E_{vis}^2}.$$

After the protojets are merged, it is possible that some particles on the far outskirts of the initial clusters will end up being closer to some other surounding clusters. Therefore the re-assignment of particles to clusters was done after every jet-merging.

The big advance of this clustering scheme is the use of transverse momentum measure, which allows better separation of perturbative and non-perturbative components of the QCD dynamics. Besides, unlike in the earlier algorithms, the number of output jets was not pre-defined.

JADE was based on binary joining without any preclustering or reassignment[8]. For all pairs of protojets {i,j} the distance measure

$$y_{ij} = \frac{2E_iE_j(1-\cos\theta_{ij})}{E_{vis}^2}$$

was calculated. If the minimal distance measure was below the resolution threshold, the corresponding protojets were replaced by the new, merged, protojet, and the process would repeat. This algorithm is IRC-safe, because both effects would be eliminated at the early stages of recombination. However, the E_iE_j product in the measure leads to recombination of back-to-back particles.

DURHAM (exclusive $\mathbf{k_\perp}$) algorithm is defined in a similar way to JADE, but with transverse momentum instead of the invariant mass in the distance measure[9] (by the time of its creation the studies showed that soft gluon emission exponentiate with ordering in transverse momentum, but not in invariant mass):

$$y_{ij} = \frac{2min(E_i^2,\ E_j^2)(1-\cos\theta_{ij})}{E_{vis}^2}.$$

Because the minimum of the two energies enters the distance measure instead of the product, two soft back-to-back objects do not get an advantage in merging over a pair of hard and soft objects. This algorithm soon became a standard jet finder in the era of LEP.

GENEVA algorithm is somewhat different from all recombination algorithms mentioned so far, as its dimensional measure was based only on the two objects combined, and not on the rest of the event (such as integral visible energy E_{vis})[10]. It was defined as follows:

$$y_{ij} = \frac{8}{9}\frac{E_iE_j(1-\cos\theta_{ij})}{(E_i+E_j)^2},$$

where the fator $\frac{8}{9}$ comes from the "synchronization" with JADE and DURHAM for the cutoff value for three jets from three partons ($y_{cut} = \frac{1}{3}$). While this algorithm strongly disfavors recombination of two soft objects with each other, thus providing a solution for the JADE problem, it is highly sensitive to energy mismeasurements, as integral visible energy present in the denominators of most of the distance measures is measured more precisely than the energies of individual objects.

Inclusive $\mathbf{k_\perp}$ algorithm is an adaptation of exclusive $k_\perp$ for experiments at hadron colliders[11]. It calculates the measure

$$d_i = E_{T,i}^2$$

for each proto-jet, and

$$d_{ij} = \frac{minE_{T,i}^2,\ E_{T,j}^2[(\eta_i-\eta_j)^2+(\phi_i-\phi_j)^2]}{R^2}$$

for each pair of proto-jets based on transverse energies E_T. If the minimal value of d corresponds to the pair of proto-jets, they are merged into a new proto jet with

$$E_{T,k} = E_{T,i} + E_{T,j},$$
$$\eta_k = \frac{E_{T,i}\eta_i + E_{t,j}\eta_j}{E_{T,k}},$$
$$\phi_k = \frac{E_{T,i}\phi_i + E_{t,j}\phi_j}{E_{T,k}}.$$

When the smallest values of d corresponds to an individual protojet, it is moved to the list of jets. While this algorithm is free of IRC problems and hence favored by the theorists, its experimental applications involved certain complications because of the irregular size and shape of the resulting jets.

Cambridge algorithm implements the same distance measure as DURHAM, but uses a different clustering procedure[12]. There are two different test variables which are used to decide, whether the proto-jets should be merged and which proto-jets should be considered next. The algorithms proceeds as follows: for all objects, values of the ordering parameter $v_{ij} = 2(1 - \cos\theta_{ij})$ are calculated, and for the pair of objects with minimal value of v_{ij} the DURHAM distance measure is calculated and compared to the cutoff value. If $y_{ij} < y_{cut}$, a new protojet is formed by merging i and j. Else the protojet with lower energy is saved as a final jet. Such angular ordering prevents "junk jet" formation in case of multiple soft gluon emission.

Cambridge/Aachen (C/A) algorithm is based on purely geometrical, angular ordering, measure defined by $R_{ij}^2 = \Delta\eta_{ij}^2 + \Delta\phi_{ij}^2$[13]. It was demonstrated that it is more sensitive to jet substructure than the others. Therefore its modifications were proposed as the basis for boosted top-jet tagging[14].

Anti-$\mathbf{k_T}$ algorithm uses the distance measure

$$d_{ij} = min\left(\frac{1}{k_{\perp i}^2}, \frac{1}{k_{\perp j}^2}\right)\frac{(y_i - y_j)^2 + (\phi_i - \phi_j)^2}{R^2},$$

which favors clustering of hard particles and is IRC safe[15]. The resulting jets are circular, which simplifies many detector-based and pileup corrections. Anti-$k_\perp$ hence became a standard for the LHC experiments.

Chapter 3

The LHC experimental facility

3.1 The accelerator complex

Remanent magnetic fields in the bending magnets do not allow to ramp an accelerator up from arbitrarily small field level. Therefore the acceleration to significantly high energies proceeds in stages by means of a chain of accelerators which gradually increase the particle energy.

Before being fed into the LHC, protons should undergo a sophisticated treatment in the injection chain: protons are extracted from hydrogen atoms and then preaccelerated in the chain of accelerators: Linear accelerator (Linac-2) – Proton Synchrotron Booster (PSB) – Proton Synchrotron (PS) – Super Proton Synchrotron (SPS) – each of which gradually increases their energy. For heavy ion beams the injection chain starts at a dedicated linear accelerator – Linac-3, which provides it with energy 3.2 MeV/nucleon. The ions are then directed into the Low Energy Ion Ring (LEIR), where they are accelerated to 72.2 MeV/nucleon before reaching the PS. The CERN accelerator complex also includes various

beam lines for fixed target physics and the Antiproton Decelerator (AD). The latter accumulated antiprotons, which arise from colliding of the PS proton beam with the block of metal. Antiprotons are then decelerated and used for the studies of antimatter. The structure of the CERN accelerator complex is shown on the Fig. **3.1**. The size of the synchrotrons is not drawn to scale. This section contains the broader description of the accelerators and beam lines involved in the LHC proton beam generation.

3.1.1 Proton Source – Duoplasmatron

Particle source is an inherent part of any accelerator complex and its importance should not be underestimated – in many cases the availability of the source dictates the acceleration scheme.

The proton source of the CERN accelerator complex is shown in Fig. **3.2**. It is the tank of hydrogen gas that gives rise to the protons to collide in the LHC[19]. The gas is fed into a plasma chamber of a duoplasmatron[20]. There a thermionic cathode emits electrons which are accelerated toward an intermediate electrode. On their way they bombard the molecules of gas forming plasma. The plasma chamber is surrounded by a magnetic coil which produces a field parrallel to the direction of plasma flow. This increases the path of electrons in the chamber by forcing them to follow helical trajectories. The plasma chamber is constricted towards the anode which increases the anode plasma density. The plasma is then extracted into an expansion cup through a small aperture and used for proton segregation. Protons which leave the duoplasmatron source have an energy of 90 keV. The beam current at this point is up to 300 mA.

3.1.2 Radio-Frequency Quadrupole

After leaving the duoplasmatron, protons are directed into the radio-frequency quadrupole (RFQ) via short (about 1 m long) low energy beam transport. The RFQ was completely designed and built at CERN and was installed in 1992-93 in the preparation for the LHC era replacing the 750 kV Cockcroft-Walton pre-injector. The RFQ consists of a cavity loaded with two pairs of opposing undulating vane electrodes with a radio frequency volt-

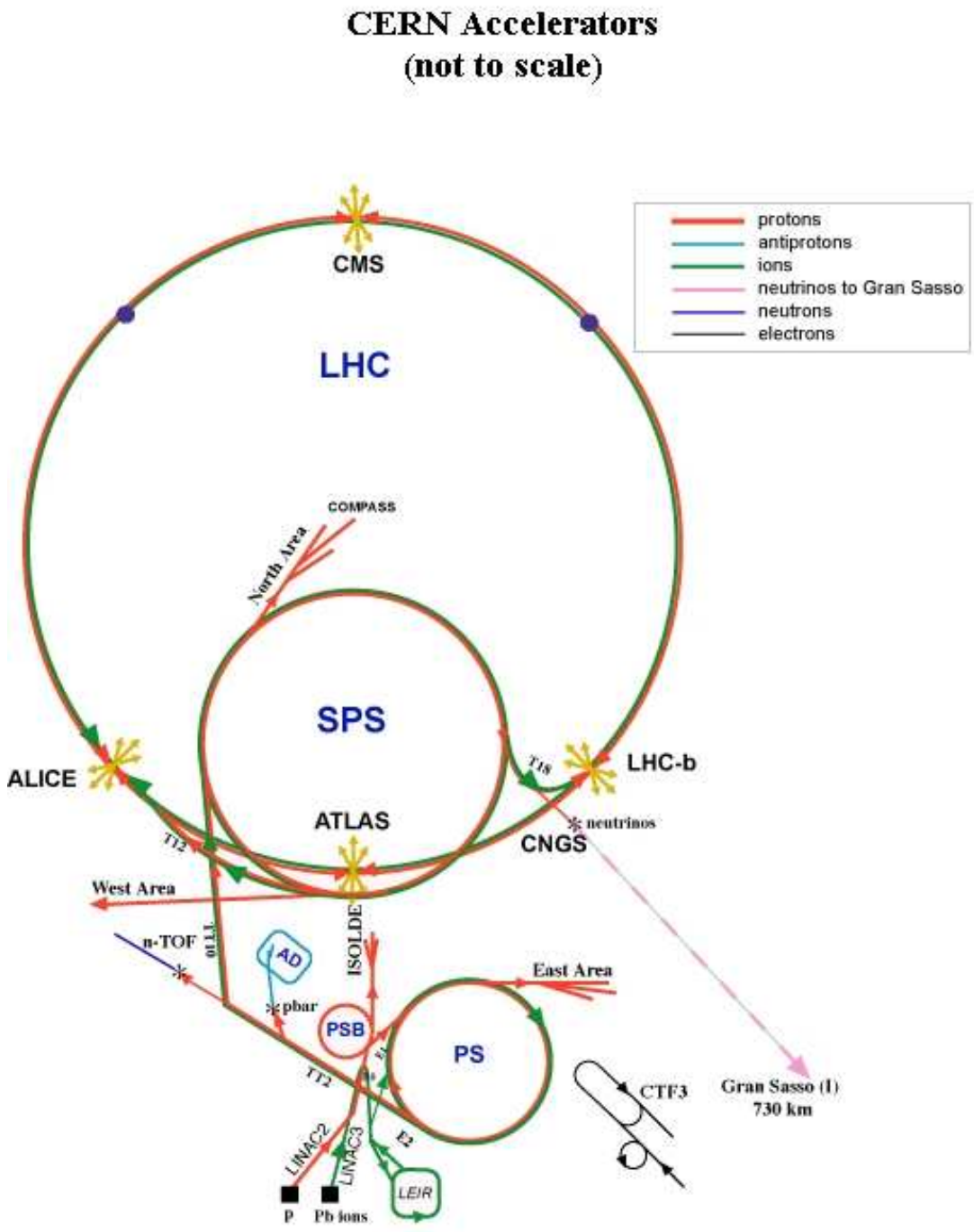

FIGURE 3.1: CERN accelerator complex. **LHC:** Large Hadron Collider; **SPS:** Super Proton Synchrontron; **PS:** Proton Synchrotron; **PSB:** Proton Synchrotron Booster; **LEIR:** Low Energy Ion Ring; **AD:** Antiproton Decelerator; **LINAC:** LINear ACcelerator; **ISOLDE:** Isotope Separator On-Line DEvice; **CNGS:** CERN Neutrinos to Gran Sasso; **nTOF:** neutron Time-of-Flight.

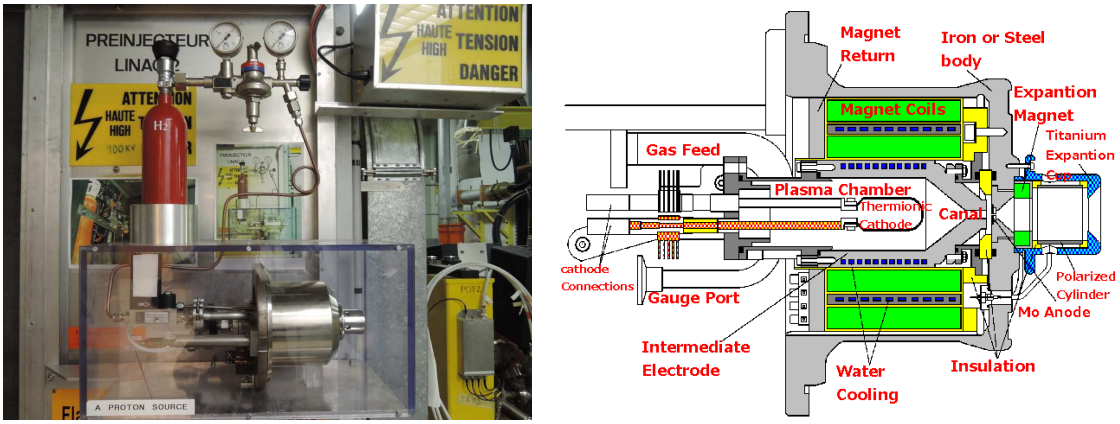

FIGURE 3.2: Proton source of the accelerator complex at CERN. **LEFT:** Duoplasmatron with a hydrogen tank - a duplicate for display. The actual duoplasmatron which is linked to the injection chain is hidden behind the metal mesh of the Faraday cage on the left. **RIGHT:** Internal structure of the CERN duoplasmatron. The picture is from [18].

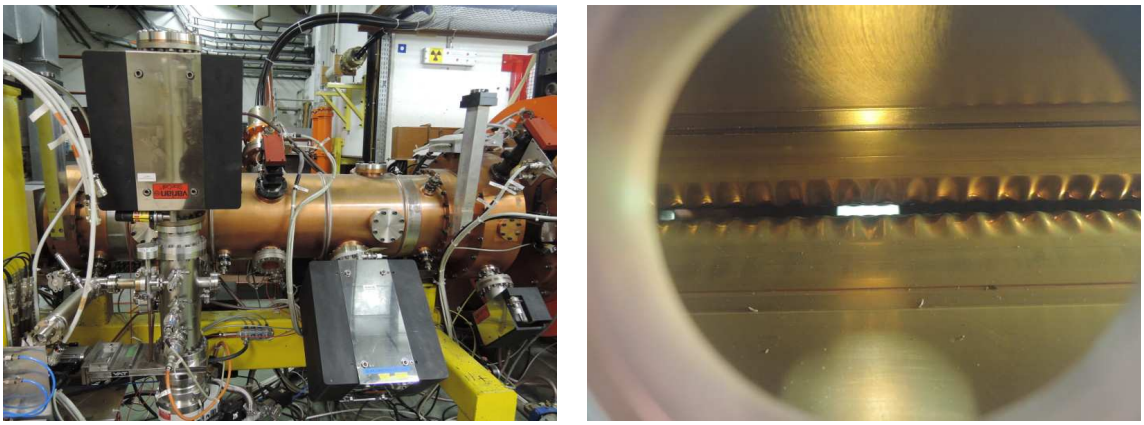

FIGURE 3.3: Radio-frequency quadrupole. **LEFT:** RFQ in the accelerator complex at CERN. **RIGHT:** Undulating vane electrodes inside of the RFQ. The picture is taken through the service opening of the RFQ displayed in the Linac2 complex.

age of opposite polarity applied (see Fig. **3.3**). The resulting electric field in the transverse plane focuses the beam in one direction and defocuses in the other. As the polarity of the electrodes changes, the beam is focused in the other diraction. The RFQ hence provides alternating-gradient focusing. As particles proceed through the cavity, the undulations on the electrodes gradually get longer which gives rise to the transverse electric mode which accelerates the protons. The 1.8 m long RFQ accelerates the beam to 750 keV ($\beta = 0.04$) and provides a beam current of 200 mA as an output. The longitudinal matching of the

RFQ to the Linac2 is done by means of two bunching cavities.

3.1.3 Linac2

Linac2 has served the CERN accelerator complex since 1978 when it had replaced Linac1[21]. The present Linac2 accelerates the protons to 50 MeV. This is a drift tube linear accelerator of Alvarez type (Fig. **3.4**). It is comprised of three tanks operating at a common RF of 202 MHz. The first tank accelerates protons to 10.3 MeV (particles acquire the speed of $\beta = 0.04$) and provides a beam current of 185 mA. The second tank brings the energy up to 30.5 MeV ($\beta = 0.145$) while the beam current on the output drops to 180 mA. Finally the third tank increases the energy to 50 MeV ($\beta = 0.314$). The same 180 mA are available on the output of the Linac2 and are delivered in shots of 10^{14} protons every 1.2 sec. The beam focusing is achieved by means of electromagnetic quadrupoles placed inside of the drift tubes. With the operation time of Linac2 of about 6000 hours per year the CERN experimental facilities hence consume about 3 μg of protons per year.

FIGURE 3.4: Linac2. **LEFT:** Array of Linac2 tanks. **RIGHT:** Drift tubes inside of the Linac2 tank. The picture is taken through the service opening of the vacuum vessel displayed in the Linac2 complex.

The Linac2 has been in service as the main supplier of protons at CERN for more than 30 years. With the progress in linac technology over those decades it now became extremely outdated; the old-fashioned components of Linac2 and recently developed problems make the maintenance more and more problematic. Besides that, the luminosity up-

grades for the LHC would require higher intensity at the PSB injection which essentially means higher energy on the output of the linac. The limited space at the end of Linac2, however, limits the possible energy increase. All of the above motivated the replacement of Linac2 with Linac4[21] which would benefit from all recent advances in linac technology. The construction has started in 2008 and the commissioning is currently scheduled for 2015.

3.1.4 Proton Synchrotron Booster

The next stage in the proton (ion) acceleration is the Proton Synchrotron Booster which is the first circular accelerator (synchrotron) in the LHC injection chain[21, 22]. It is composed out of four superimposed rings with a radius of 25 m; the nominal beams in the adjacent rings of PSB are 36 cm apart, Ring 3 (third from the bottom) is leveled with the PS. The PSB is formed by 32 dipole (bending of the beam) and 48 quadrupole (focusing of the beam) magnets, which are arranged in a periodic pattern with a repeating sequence: straight section, dipole, triplet of quadrupoles, dipole (Fig. **3.5**). Each of the magnets is essentially a column of four magnets which share a common yoke and are powered by a common power supply. Fine adjustments in individual rings are achieved by means of additional trim power supplies and coils. Straight sections contain other equipment for small corrections, diagnostics etc. as well as an RF system for acceleration. Currently the RF system consists of the cavities for harmonic numbers 1 (2 MHz) and 2 (4 MHz) and a higher, variable frequency system (6-16 MHz) for controlled emittance blow-up.

To fill all four rings of the PSB with a pulse of Linac2, the pulse is sliced with the Proton Distributor: a system of five pulsed magnets with ferrite cores (Fig. **3.6**). Once the rise time of the Linac2 pulse is over, four of the cores each deflect equal slices of the pulse toward the different apertures of a septum magnet which pulls them even further apart to separate them according to the levels of the PSB rings. The most upstream core at the same time deflects the tail corresponding to the fall-time of the pulse into an absorber block – a tail dump. The fraction of the pulse corresponding to the rise-time also hits the absorber – a head dump. At any time, in case of a missing trigger or Proton Distributor system failure,

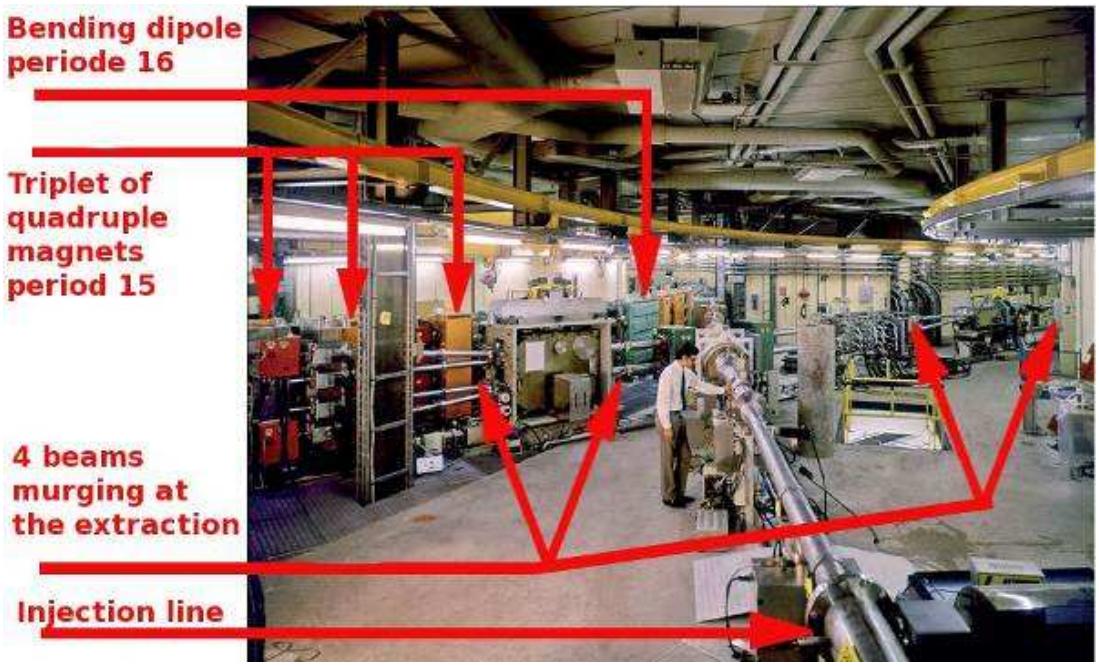

FIGURE 3.5: PS Booster, peroids 15 and 16, injection and extraction beam lines. Murging of the beams from four rings into a common beam pipe is clearly seen in the extraction beam line. The main photo is taken from [23]

the entire linac pulse is dumped into the head dump. However, if only one of the cores of the Proton Distributor fails, the corresponding pulse slice will be deflected by the next core downstream to the corresponding ring of PSB. The slices are then further deflected to achieve the separation of PSB rings and injected into the PSB by means of multi-turn injection.

After the PSB acceleration cycle is over, the bunches in different rings are synchronized, extracted by a system of slow extraction bumpers and merged into a common beam line (Fig. **3.5**).

The operation of PSB is essentially a repetition of one of the pre-programmed super-cycles, which are made up out of 1.2 sec-long basic cycles. During each of the basic cycles the beam for one of the PSB users (such as LHC, ISOLDE, SPS fixed target physics, etc.) is injected, accelerated and extracted. Nevertheless, the beams in the basic cycles are completely independent and can differ by intensity, transverse and longitudinal emittance, number of PSB rings in use, harmonic at the extraction.

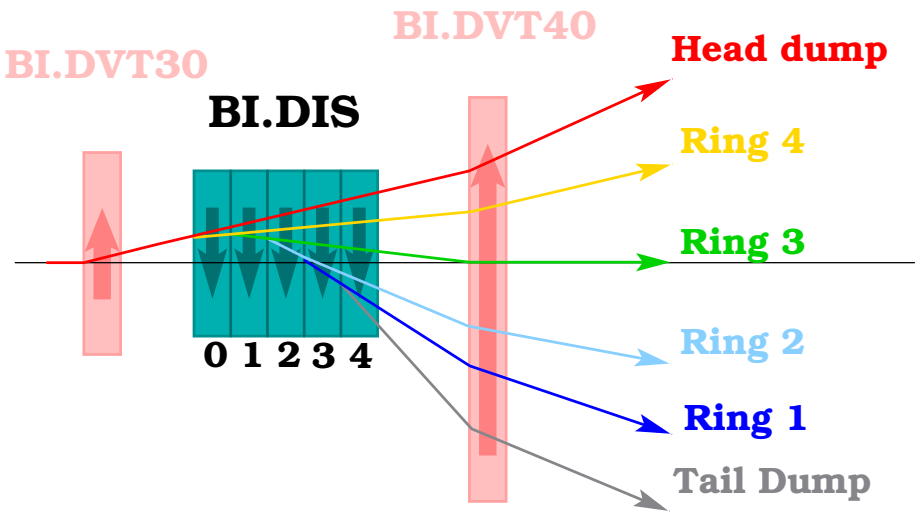

FIGURE 3.6: Proton Distributor in the injection to PSB. Red and grey trajectories correspond to the rise and fall time of the pulse from linac and are dumped, while the medium, homogeneous part of the pulse is split in four for future injection into PSB rings.

The beams for the LHC are generated by means of double-batch filling: in the first basic cycle all four rings of the PSB are used, operationg at harmonic 1 (one bunch per ring), they are then extracted toward the Proton Synchrotron (PS) in order 3-4-1-2. While the first batch of protons circulates in the PS, unaccelerated, the second basic cycle of the PSB makes use only of the top two rings, 3 and 4, each accelerating one bunch on harmonic 1 and extracting them toward PS 1.2 sec after the first batch.

3.1.5 Proton Synchrotron

Once the particles are accelerated to 1.4 GeV, they are injected into the CERN Proton Synchrotron (PS) – a 100 m radius synchrotron.

PS is the oldest of the major particle accelerators built at CERN and the first proton synchrotron to take advantage of the strong focusing concept. Since its comissioning in 1959 it remains in service for more than 50 years[24]. Despite many upgrades over those years, the main magnetic system – state of art at the time of construction – remain unchanged. It is comprised of 100 magnet units which are, unlike magnets of PSB, combined-function

elements: the beam focusing is achieved by precisely designed transverse gradient in the bending field. Each magnet unit consists of focusing (**F**) and defocusing (**D**) half-units. C-shape steel magnetic blocks with two different profiles of the poles produce alternation of the gradient. Five such blocks, each 41.7 cm long and weighting 2890 kg, form a half-unit. Ten blocks form a magnetic unit with two common aluminum excitation coils around top and bottom poles. The straight section (**O**) between the main magnetic units are field-free and carry corrective magnetic lenses for fine adjustments of the field, accelerating RF cavities and other equipment (Fig. **3.7**). The main magnetic units of the PS arranged to produce the recurrent **FOFDOD** configuration.

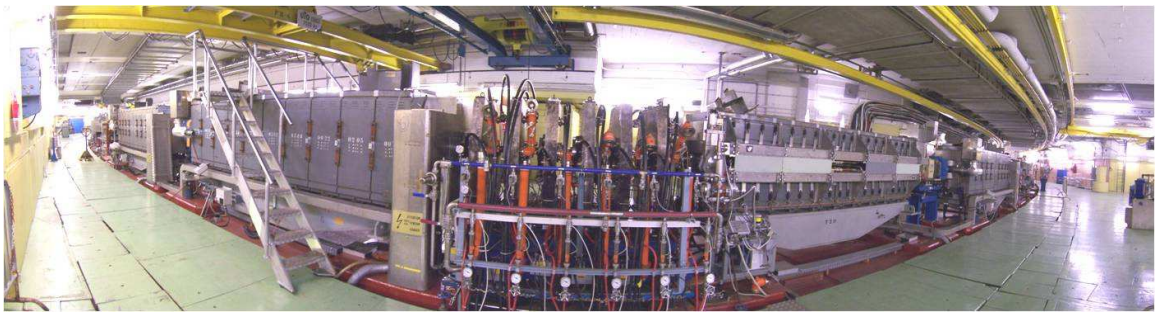

FIGURE 3.7: View of the PS tunnel with the accelerating RF cavity system (in the middle) and main magnetic units (on both sides of the RF). The magnetic unit to the left from the cavity is installed with its return yoke inside of the synchrotron ring, while the unit on the right from the RF system is installed with the yoke outside of the accelerator ring.

The RF system of the PS consists of tuneable ferrite loaded cavities and several types of fixed frequency accelerating cavities. And yet another strong side of the PS machine, which contributed to the success of many physics programs at CERN during five and a half decades, is the amazing diversity of transformations performed over the bunch train by means of the RF systems. The treatment of the bunch train for the LHC in the PS is indeed sophisticated. Six PSB bunches are used to fill the PS, so this can be done by ejecting two batches: $4 + 2$ bunches with 1.2 sec pause (duration of the basic cycle in the PSB) between the consecutive batches ($3 + 3$ bunch injection PSB beams were also developed and studied). The PS operates on harmonic 7, so once two PSB batches are injected, there is one vacant bunch spot (the gap in the bunch train thus allows for the ejection kicker magnets rise time and hence bunches are not lost during injection into the SPS).

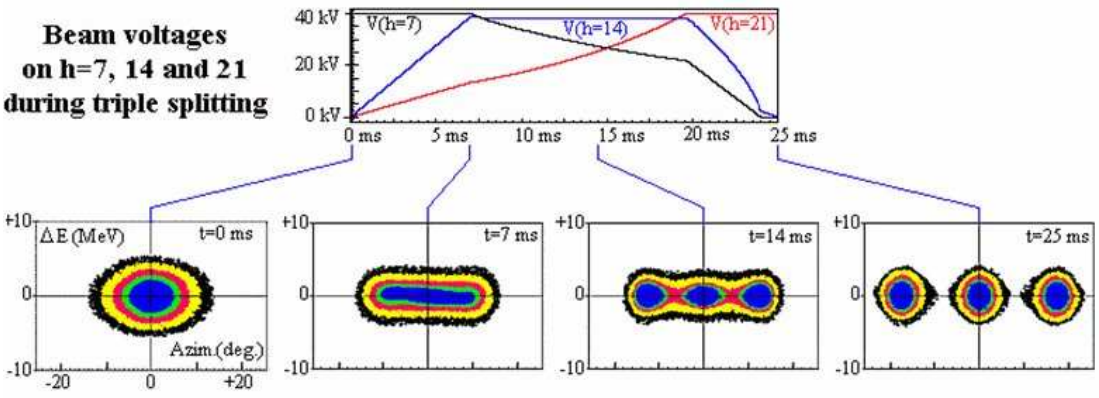

FIGURE 3.8: Principle of bunch splitting in the PS shown for triple splitting. First the bunch is stretched by the RF of the double harmonic, then the constrictions are formed by the triple harmonic RF. As the action on the lower harmonics fades away, the bunch is split in three with the same distribution of particles as in the initial one. Picture taken from [21].

First, the injected beam of 1.4 GeV is captured by the subset of tuneable cavities, operating at harmonic 7. Then each of the original six bunches, 160 ns long, is split into three by successive engaging of the sets of cavities pretuned to harmonics 14 and 21 (Fig. **3.8**). After triple splitting is achieved, the resulting 18 bunches are captured by the set of cavities at harmonic 21, while the rest of the tunable cavities re-tune from harmonics 7 and 14 to 21. Then, with the RF system operating at harmonic 21, the beam is accelerated to 25 GeV. At this energy the fixed frequency RF (harmonics 42 and 84) take over and each bunch is split in two twice[1], yielding 72 bunches and 12 (consecutive) vacant bunch spots (PS operation on harmonic 84). Finally, the length of bunches is adjusted by means of rotation with the RF system at harmonics 84 and 168. This results in a bunch train with 72 bunches of 4 ns and 320 ns gap in the sequence of bunches, which allows the PS ejection kicker magnets to rise.

3.1.6 Super Proton Synchrotron

After the acceleration cycle in the PS is over the transfer line which is about 850 m long directs protons into the Super Proton Synchrotron (SPS). The SPS has been in operation since

[1]This is the way of generating the nominal bunch train with 25 ns spacing. For the 50 ns spaced bunch train the second splitting in two in the PS is not performed.

1976 and contributed a lot to particle physics research: it provided high energy beams to various fixed target experiments. Since the year of 1982 it has been used as a $p\overline{p}$ colliding-beam storage ring, which has led to the discovery of W and Z bosons. Later, between 1989 and 2000, it had served as an injector for the Large Electron-Positron Collider (LEP). Nowadays it remains in service as the last stage of the injection chain for the LHC, provides the beams for the NA61/SHINE, NA62, COMPASS experiments and CNGS project.

The synchrotron tunnel of the SPS, 4 m in diameter, is located about 40 m underground. The SPS machine is formed by six circular segments (947 m radius) and six straight sections 250 m each. The circumference of the SPS is divided into 216 half-periods. The typical half-period is formed by six main magnet elements: focusing quadrupole, four bending magnets, each 6.26 m long, and a defocusing quadrupole, or the same structure in the reversed order[1]. The strong focusing system hence follows the **FODO** structure. Although at the time of construction, the superconducting magnets were already available, the decision had been taken in favor of much better understood room-temperature electromagnets, providing 1.4 T magnetic field.

The sextants of the synchrotron are formed by 18 subsequent periods such that four periods corresponding to the straight section are in the middle of the sextants. Straight sections contain RF accelerating systems, merging points with the injection beamline and two extraction beamlines, beam instrumentation equipment. Short straight sections inside the periods accomodate magnetic lenses for fine corrections of the beam.

When the proton beam reaches the SPS, the velocitiy of protons is already close to the speed of light. Therefore during acceleration their velocity (and hence the frequency) does not change too much (only by a fraction of a percent). This allows to make use of fixed frequency traveling wave cavities[25] with narrow bandwidth (Fig. **3.9**).

[1] At first sight it may seem that four magnets of the same function set next to each other is not the most optimal solution. But it is due to a historical reason: the evolution of the SPS complex was decided to follow the so called ”missing magnet” concept: if the size of the machine is not an issue, one can design the synchrotron with long straight sections next to the bending units. When the decision of the energy upgrade is taken, the straight sections accomodate extra bending magnets to increase magnetic flux density. So the initial design of the SPS included two bending magnets for the 250 GeV machine and the space for two more in future upgrades. Later on, however, the decision was taken to proceed directly to the ”upgraded” design with all four bending magnets installed. In contrast, the evolution of the PS was guided by the ”missing power” concept: the magnets were overdesigned to be capable to operate with higher power, and it was the power supply system which was extensively upgraded.

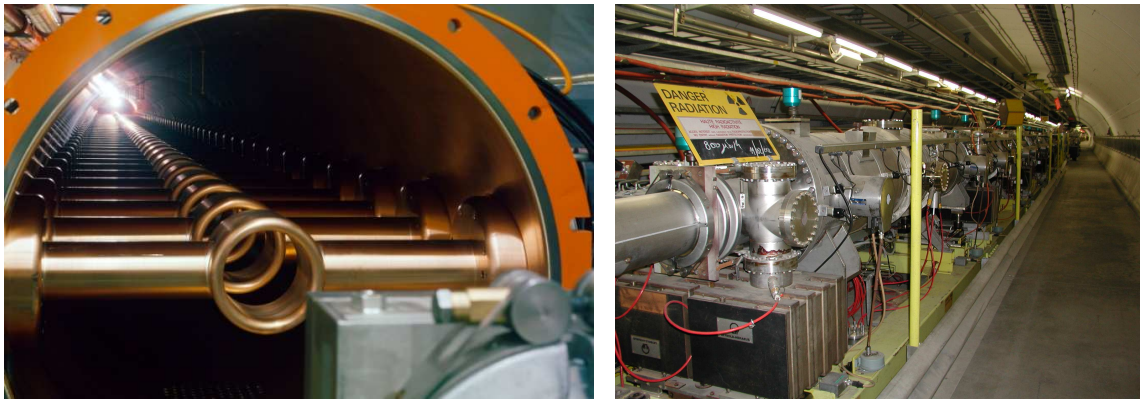

FIGURE 3.9: Traveling wave accelerating RF cavity in the SPS. **LEFT:** The internal view of the RF from the archive of CERN RF/SR section; **RIGHT:** RF cavities in the SPS tunnel.

The circumference of the SPS is about eleven times that of the PS; hence, the SPS could accomodate eleven batches from the PS. Though, the more efficient bunch train generation scheme requires to fill the SPS with a train of three or four batches from the PS with only a small gap of 8 vacant bunch spots (to allow for the SPS injection kicker rise time of 220 ns).

After the acceleration cycle in the SPS is over, the beam is directed into the LHC through one of the two transfer tunnels.

3.1.7 The Large Hadron Collider

The LHC went live on 10 September 2008. Ever since it remains the record holder both as the most powerful particle accelerator and the largest hadron collider ever built. It is housed in the 27 km long tunnel inherited from the LEP accelerator. Construction of that tunnel at that time was the biggest european civil engineering project – it took about three years to make the tunnel alone. The tunnel spans across the Franco-Swiss border and lays 50 to 175 m underground.

Eight arcs of the synchrotron, which carry magnetic elements, are interlayed with eight insertion regions (IR) – straight sections are about 528 m long. Those are used for experimental and monitoring equipment. The major experiments are located at four of the IRs: ATLAS (IR-1), ALICE (IR-2), CMS (IR-5), LHCb (IR-8). Two of them are also used for the injection of the proton beams from the SPS (IR-2 and IR-8). IR-4 houses the acceler-

ating cavities. Two beam collimation systems are located in the IR-3 and IR-7. Finally in the IR-6 the beams are extracted from the LHC for dumping.

As the LHC operation requires not only high energies of hadrons, but also high beam intensities, the antiproton beam was not an option. Hence the design for two counter-rotating proton beams demanded for bending magnetic fields of opposite polarity and thus separate beam pipes[1]. The LHC tunnel is only 3.8 m in cross-section; therefore, installation of two separate cryogenic rings would be problematic. The design of the main magnetic units – bending dipoles and focusing quadrupoles – has adopted the twin-aperture structure: two sets of coils surrounding the beampipes share a common iron yoke and mechanical structure. The entire assembly is then installed inside of the cryostat (Fig. **3.10**).

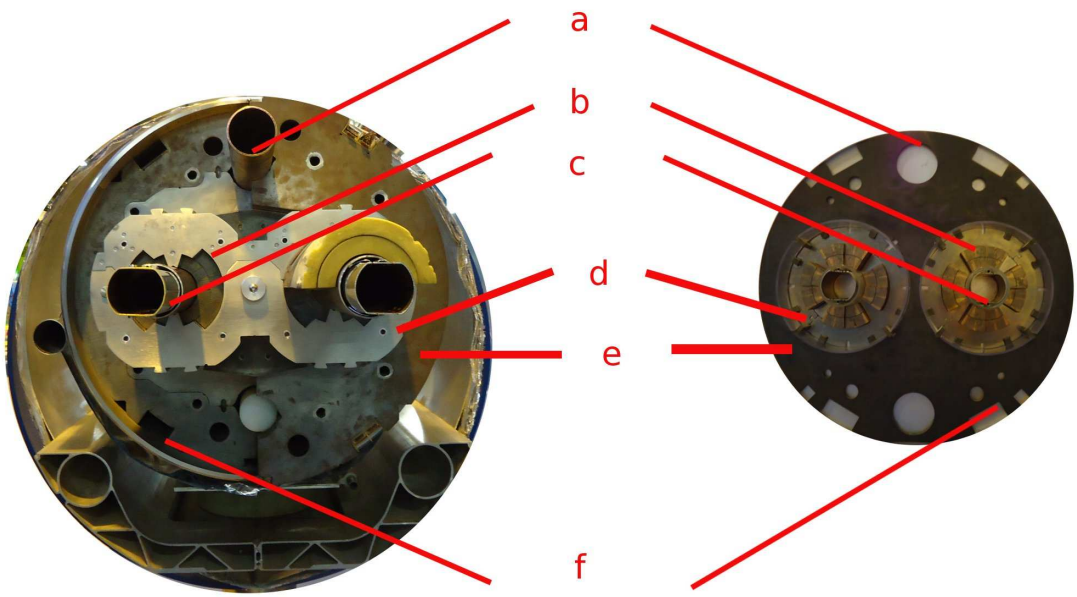

FIGURE 3.10: Cross-section of the main magnets of the LHC. Pictures are taken at the SM18 – cryogenic testing facility. **LEFT:** Cryostat of a dipole installed in the vacuum vessel. **RIGHT:** Cryostat of a quadrupole. **(a)** superfluid Helium guide; **(b)** superconducting coils; **(c)** beam chambers; **(d)** austenitic steel collar; **(e)** return yoke; **(f)** cable trays. Assorted holes seen in the yoke serve for equalizing of the magnetic flux and avioding of the yoke saturation.

The magnets are cooled down to 1.9 K and can provide a field up to 8.33 T. The bending magnets are 15 m long at room temperature, but as they are cooled down, they shrink

[1]The only common sections are located in the insertion regions housing the experiments.

by 4.5 cm. To accomodate this significant change in length, only one end of the magnet is mounted, while the other one is allowed to move freely. The magnet shrinking is then compensated by the stretching of a stainless steel bellows (Fig. **3.11**). To avoid any perturbations of the RF field at the junction of the beam vacuum chambers, the RF-bridge formed by 30 sliding fingers is installed in the interconnection.

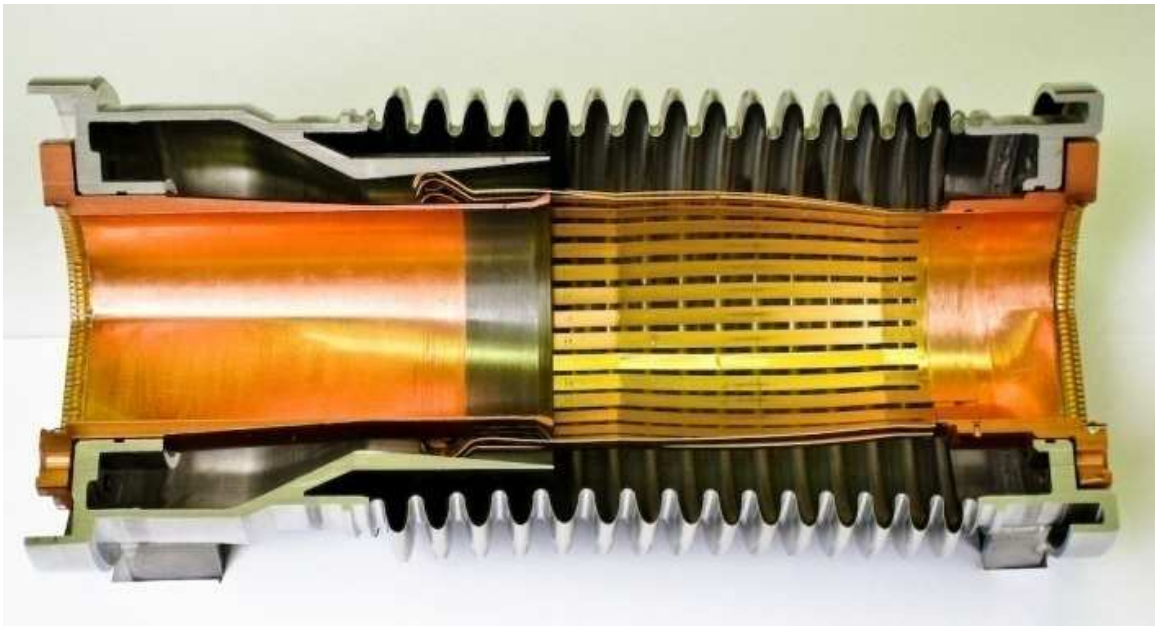

FIGURE 3.11: Steel bellows with RF-shielding fingers connect the beam vacuum chambers between the superconducting magnets. The picture is taken from [26].

Each of the eight arcs of the LHC is formed by 23 arc-cells; the cells are 106.9 m long and contain two half-cells with 3.10 m quadrupole followed by three 15 m dipoles. As the twin-aperture quadrupole magnets focus one beam and defocus the other, the beamline optics period **FODO** in one ring corresponds to **DOFO** in the other ring. The multi-pole magnets used for small corrections serve individual beampipes and are installed at the ends of the main dipoles and quadrupoles.

By the time the beams are finally injected into the LHC, they are already highly relativistic: during the entire acceleration cycle in the LHC the revolution frequency changes insignificantly, only about 2.5 ppm, and so does the accelerating RF frequency. With such a narrow bandwidth of the RF system, standing wave RF cavities are used with a resonant frequency bandwidth of 100 kHz (the RF frequency of the cavities is 400 MHz).

The choice has been made in favor of superconducting technology: niobium-coated copper cavities[27], each with a single cell, are housed in a common cryostat in groups of four (Fig. **3.12**). Superconductivity is reached by cooling to 4.5 K by means of liquid helium. Each ring is equipped with eight RF cavities providing 2 MV of accelerating voltage (16 MV per beam).

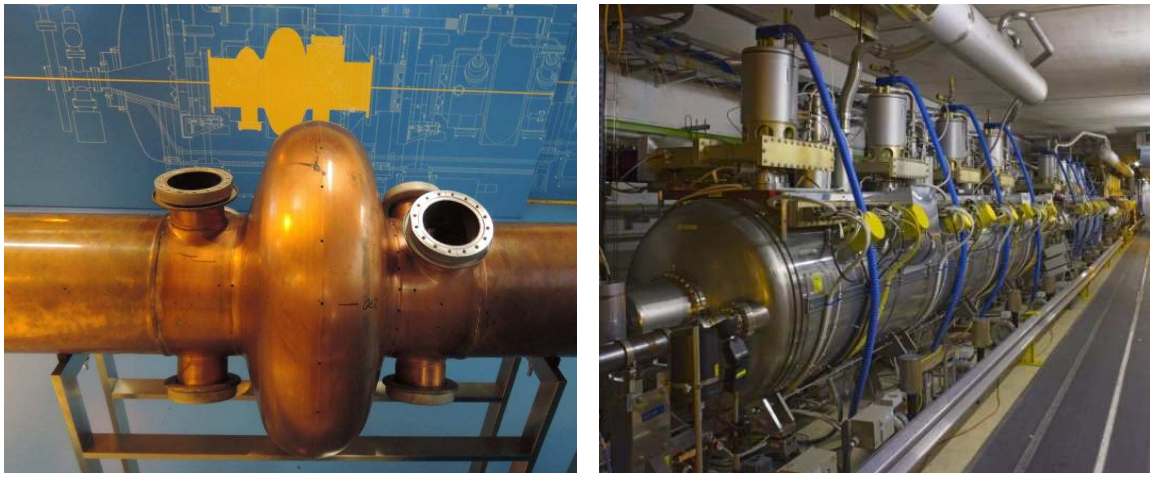

FIGURE 3.12: Accelerating cavities of the LHC. **LEFT:** Bare RF cavity on the display of the CERN cryogenic testing facility. **RIGHT:** The actual RF system in the tunnel of the LHC – two cryostats contain eight standing wave supercondicting RF cavities.

The RF system is not only used to accelerate the protons, but also to create and maintain the structure of the beam: as the accelerating frequency of the RF cavities at the LHC is 400 MHz, it operates at the harmonic $h = \frac{L\nu}{c} \approx 35640$, and creates the same number of RF buckets for capturing the proton bunches. In practice, only 2808 of those RF buckets are occupied by the proton bunches, the rest of the vacant buckets is uniformly[1] distributed around the ring. This ensures that not only the bunches are small in the longitudinal direction (RF bucket is only 2.5 ns wide), but also spaced at least 25 ns apart, which makes them suitable for the LHC detectors.

The LHC receives trains of three or four batches from the SPS (Fig. **3.13**). Hence in the LHC ring every three-batch and four-batch structure is followed by 38 and 39 vacant bunch spots correspondingly – both gaps are due to the LHC injection kicker rise time of 0.94 μs.

[1]Except for a few longer gaps which allow for the rise time in various magnetic systems of the LHC complex.

The entire bunch train in each ring of LHC is followed by an abort gap – 119 vacant bunch spots to allow for the LHC dump kicker rise time of 3 μs.

It takes about 15 min to complete the injection process, then the main dipoles are ramped up synchronously with the RF system, which takes another 20 min. After some final preparations the beam is ready for the physics run, which can last 10-20 hours.

3.2 The experiments

There are four large (ATLAS, CMS, LHCb and ALICE) and three small (TOTEM, LHCf, MoEDAL) experiments at the LHC. There detectors were designed, constructed and commissioned by international collaborations of many institutes, bringing together scientists from all over the world. Each experiment has particular goals and is optimized to fulfill its physics program.

The two biggest experiments, ATLAS and CMS, use general-purpose detectors to both investigate in detail a variety of known physics phenomena and probe the terra incognita. The availability of two independent detectors based on different designs and technologies provides an opportunity for cross-confirmation of any new discoveries. ALICE and LHCb are focused on specific phenomena. These four experiments occupy huge caverns on the LHC ring.

The small detectors, TOTEM, LHCf and MoEDAL, are focused on forward particles. Hence, their detectors are located on the LHC ring on both sides of the bigger experiments.

3.2.1 CMS

CMS (**C**ompact **M**uon **S**olenoid) is a general purpose detector at the LHC. The detailed description follows in the next chapter.

3.2.2 ATLAS

ATLAS (**A** **T**oroidal **L**HC **A**paratu**S**) is one of the two general purpose particle physics experiments at the LHC. It is lighter and less dense than its competitor, CMS (Fig. **3.14**).

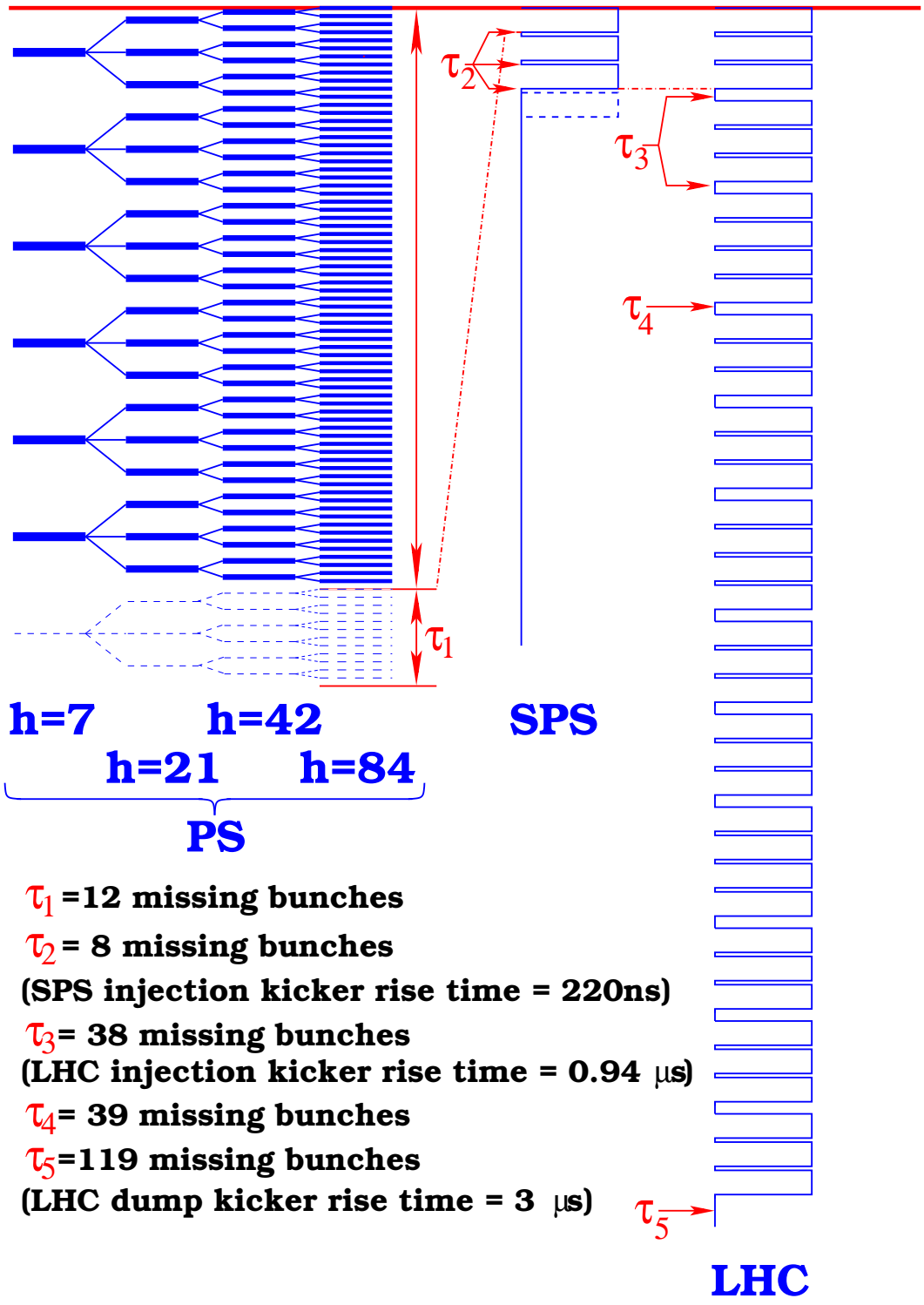

FIGURE 3.13: LHC bunch train and its formation in the PS and SPS.

With its length of 44 m and diameter of 22 m it is the biggest general purpose detector ever built.

As a general purpose detector, ATLAS is suitable for a wide range of particle physics tasks: it is capable of improving the existing measurements in the realm of the Standard Model, as well as for probing ”new physics” grounds such as unification theories, Supersymmetric theories, extra dimensions, etc. Although it was the last missing SM particle, the Higgs boson detection requirements served as a benchmark for all subdetector systems performance during construction of the experiment. Along with the CMS experiment, ATLAS has anounced the discovery of a particle fully compatible with the Higgs boson in 2012.

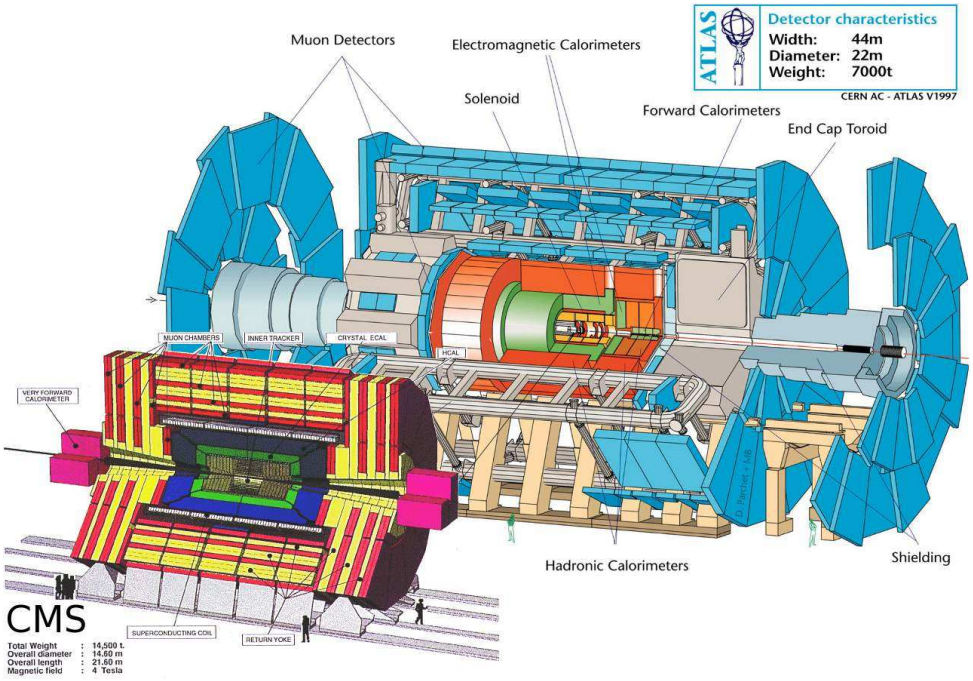

FIGURE 3.14: General purpose detectors at the LHC: CMS (on the left) and ATLAS (on the right). Note the difference in size and weight.

3.2.3 LHCb

LHCb (**L**arge **H**adron **C**ollider **b**eauty) experiment is focused on heavy flavor (charm and beauty) physics. At high energies both b and $\overline{b}$ quarks are mostly produced in the same

sharp forward or backward cone. The LHCb detector implements a single-arm design for the geometry of the spectrometer (Fig. **3.15**). As, in this case, the occupancy of hits can be an issue at the high luminosities delivered by the LHC, the beam focus can be tuned to lower the luminosity at the LHCb independently from other experiments.

The physics goals of the experiment cover studies of rare b-hadron decays and precise measurements of the CP violation in various decays. The latter can shed light on the discrepancy between matter-antimatter assymmetry of the Universe and Standard Model predictions for this assymmetry.

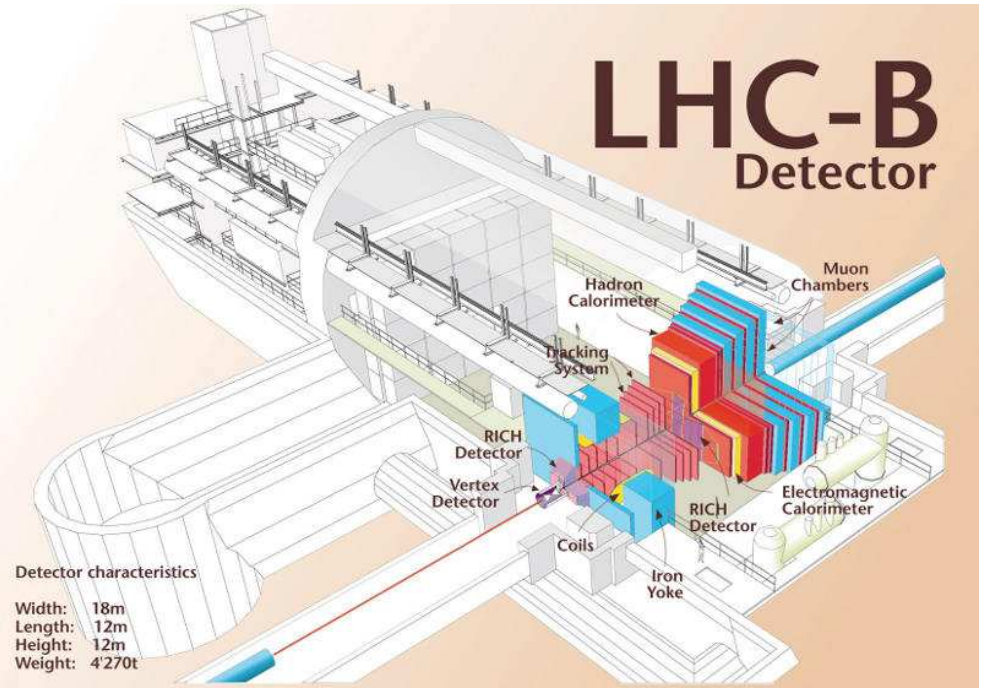

FIGURE 3.15: LHCb detector.

3.2.4 ALICE

ALICE (**A** **L**arge **I**on **C**ollider **E**xperiment) is a general purpose experiment, which focuses on strong interaction studies (Fig. **3.16**).

It is optimized to study $Pb - Pb$ collisions at a center-of-mass energy of 2.76 TeV per nucleon. In the collision the resulting energy density and temperature can be sufficient to produce a quark-gluon plasma. The detector is also taking data with $p - p$ collisions for

reference. The physics program also includes data taking with nuclei lighter than Pb to vary the energy density.

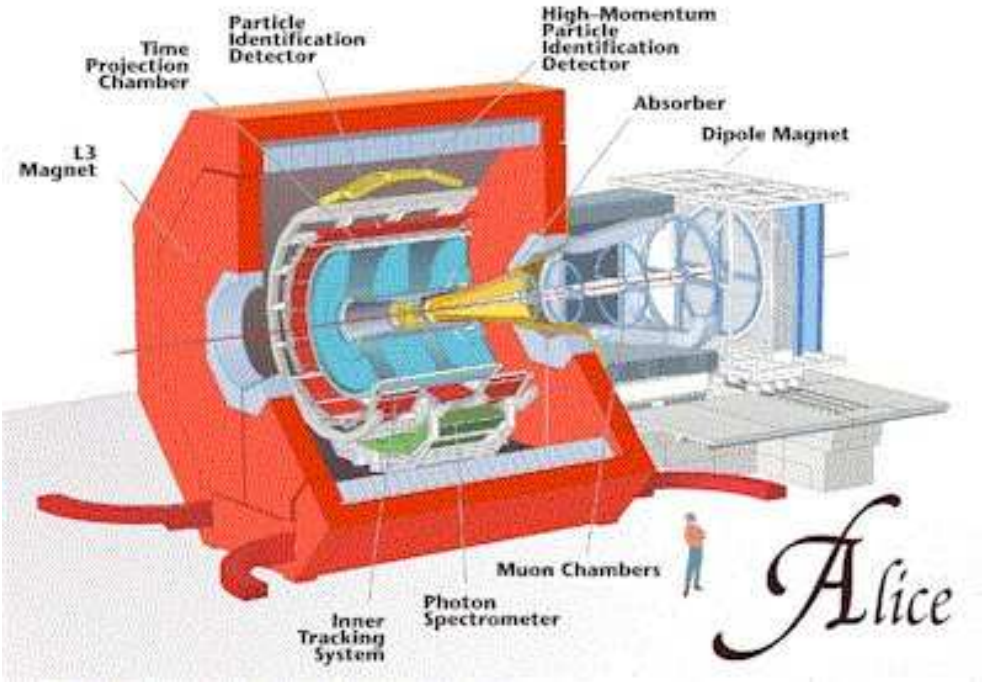

FIGURE 3.16: ALICE detector.

3.2.5 TOTEM

TOTEM (**TOT**al cross section, **E**lastic scattering and diffractive dissociation **M**easurement) experiment is dedicated to the measurements of the total $p - p$ cross-section by means of a luminosity independent method. Its other goal is to achieve deeper understanding of the proton structure by studying elastic scattering with large momentum transfers, and via a comprehensive menu of diffractive processes.

Unlike previously mentioned experiments – big, but localized in a particular cavern, – the stations of TOTEM are spread over 400 m along the LHC tunnel around the interaction point, where the CMS detector is installed.

3.2.6 LHCf

LHCf (**L**arge **H**adron **C**ollider **f**orward) experiment is dedicated to measuring a very forward production cross section and energy spectra of neutral particles.

Those measurements are essential for understanding the origins the ultra-high energy cosmic rays and the development of atmospheric showers. The interpretation of data from atmospheric-shower experiments strongly depends on the interaction model. A bunch of competing models exist, however none could be verified in the pre-LHC era, as the energy scale of highest energy cosmic rays spreads beyond $10^{20}\,eV$, which is several orders of magnitude higher than the laboratory equivalent of the S$p\overline{p}$S or Tevatron. LHCf will be capable to test the existing models up to the equivalent of $10^{17}\,eV$ in the laboratory frame, provided by the LHC.

The detector is modular and installed 140 m on both sides of the ATLAS detector.

3.2.7 MoEDAL

In 2010 the decision was taken for construction of its seventh experiment – MoEDAL (**Mo**nopole and **E**xotics **D**etector **A**t the **L**HC). It is focused on the search for the magnetic monopole – a hypothetical particle which carries magnetic charge. The experiment is also looking for highly ionizing Stable Massive Particles (SMPs), which arise in some new physics models, such as SUSY with R-parity or extra dimensions.

Chapter 4

The CMS experiment

4.1 Introduction

The Compact Muon Solenoid experiment is a general purpose 4π detector which was designed to accomodate a wide range of searches dictated by the LHC physics programe. They span from the studies of QCD, electroweak and flavor physics to searches for the Higgs boson, extra dimensions, and dark matter candidates. The detector requirements imposed by the physics programe can be summarized as follows:

- Good muon identification and momentum resolution in a wide range, good di-muon mass resolution, reliable determination of the sign of muons up to a momentum of 1 TeV/c. This defines the large bending power of the magnet.

- Good reconstruction efficiency and momentum resolution for charged particles in the inner tracker as well as both efficient triggering and tagging of taus and b-jets. This leads to the use of pixel detectors close to the interaction region.

- Excellent electromagnetic energy resolution, good diphoton and dielectron mass resolution, wide geometric coverage, π^0 rejection, efficient electron and photon isolation. This is addressed with a fully active scintillating crystal-based electromagnetic calorimeter.

- Good missing transverse energy and dijet mass resolution, which leads to a hadron calorimeter with large geometric coverage and fine segmentation.

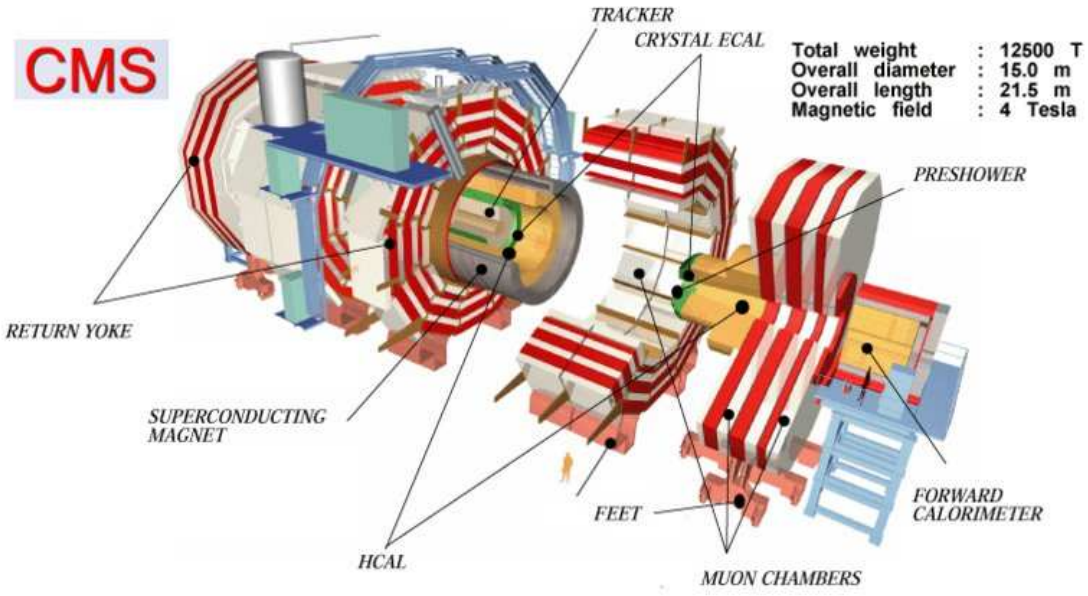

FIGURE 4.1: Layout of the CMS detector

All of the above requirements are satisfied in the design of CMS. The detector is divided into subdetector systems which perform dedicated but complementary tasks. The layout of the detector is shown in Fig. **4.1**.

4.2 Superconducting Magnet

To achieve high precision in measuring the momentum of high-energy particles large bending power is required. For a solenoid of moderate size it requires the use of superconducting technology. The four layers of winding made from a stabilized reinforced NbTi conductor

form 220 tons of cold mass of the CMS superconducting solenoid, which creates a magnetic field of 3.8 T along the beam dirrection. With its inner diameter of 6 m and length of 12.5 m it hosts tracking and calorimetry systems inside. The flux is returned through the yoke made of three layers of iron with a total thickness of 1.5 m (300, 630 and 630 mm in the barrel region) interleaved with four muon stations. In the barrel region the yoke is formed by one stationary - central - ring and four movable rings, the endcaps of the yoke are formed by three discs (250, 600 and 600 mm). The total mass of the iron in the return yoke is 10 000 tons which makes up 80% of the overall CMS mass.

4.3 Inner tracker

The layout of the inner tracker of CMS is shown on the Fig. **4.2**. It has a tracking volume given by a cylinder of length 5.4 m and radius 1.1 m and provides tracking coverage up to $|\eta| < 2.5$. While the tracker is based on semiconductor technology throughout, various parts of it differ from each other substantially.

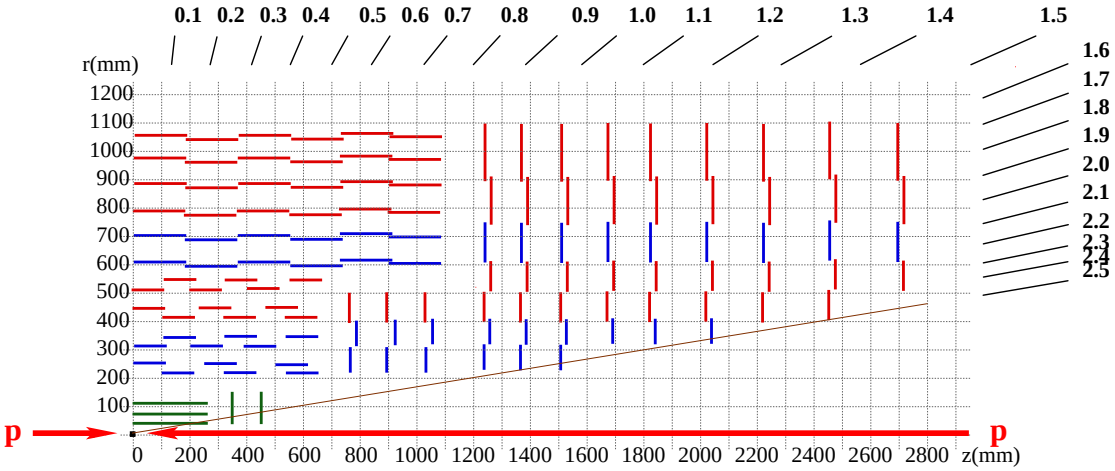

FIGURE 4.2: The inner tracker layout (1/4 of the z view). The Pixel Tracker is shown in green. Two colors are used for the Silicon Strip Tracker: single-sided modules are shown in red, and the double-sided are in blue.

The nominal interaction point is surrounded by three 53 cm long cylindrical layers (at

radii of 4.4, 7.3 and 10.2 cm) of hybrid pixel detectors in the barrel region and the endcaps. Each endcap is formed by two fan-blade disks of pixel detectors, which extend from 6 to 15 cm from the nominal beam and are positioned 34.5 cm and 46.5 cm away from the nominal interaction point. The blades of the endcap disks are rotated by 20 degrees with respect to the plane of the disks. Altogether they form the Pixel Tracker (in Fig. **4.2** it is shown in green) and provide three-hit coverage in pseudorapidity up to $|\eta| < 2.2$ and two-hit coverage up to $|\eta| < 2.5$. With a pitch of 100 μm$\times$150 μm, the Pixel Tracker provides a resolution of 10 μm in $r - \phi$ and 20 μm in z, which is required for secondary vertex reconstruction. The overall area of the Pixel Detector is 1 m^2 and is hosting 66 million independent channels.

The Silicon Strip Tracker[28] instruments the tracking volume from 20 to 120 cm in r and up to 280 cm in $|z|$ and provides a pseudo-rapidity coverage up to $|\eta| < 2.5$. The inner 4 layers of the barrel utilizes thin silicon sensors with a pitch size from 80 to 120 μm. The outer 6 layers are made of thicker sensors with a strip pitch varying from 120 to 180 μm. The endcaps are formed by 3 small disks and 9 big disks, and are designed with the strips pointing to the beam axis, so that the strip pitch is constant in angle, but varies linearly. All over the Tracker the strip pitch varies between 80 and 205 μm from innermost to the outmost layer. Some layers of the Silicon Strip Tracker are made of double-sided, "stereo" modules: two independent single-sided detection units are mounted back-to-back at an angle of 100 mrad to provide measurements in both $r-\phi$ and $r-z$. On Fig. **4.2** those modules are shown in blue while the single-sided modules are depicted in red. The active area of the Silicon Strip Tracker adds up to almost 200 m^2 and is read out by 9.6 million channels and together with the Pixel Detector provides precise and efficient tracking information for the determination of charges, momenta and impact parameters of charged particles.

4.4 Electromagnetic Calorimeter

After passing though the tracker, particles enter the electromagnetic calorimeter (ECAL). This is a homogenious calorimeter, i.e. the entire volume is formed by the sensitive material, scintillating lead tungstate ($PbWO_4$) crystals, and contributes to the signal. The

photodetection is done by means of silicon avalanche photodiodes (APDs) in the barrel and vacuum phototriodes (VPTs) in the endcaps.

The barrel, cylindrical, part of the ECAL is formed by a grid of 360 crystals in ϕ and 170 crystals in η, resulting in a total of 61200 crystals with the overall volume of 8.14 m^3 and weight of 67.4 t. The front face of the crystals in the barrel is located at 129 cm from the nominal interaction point. The tapered-shaped crystals of the barrel have a length of 230 mm (25.8 X_0) and a cross-section of 0.0174×0.0174 in $\eta - \phi$, which corresponds to $22 \times 22\,mm^2$ at the front face of the crystal and $26 \times 26\,mm^2$ at the rear face. The barrel is assembled such that the axis of each crystal makes a small angle, 3°. In this case particles cannot escape detection by going through the thin cracks (0.35-0.5 mm) between the crystals. The barrel of ECAL provides coverage in pseudorapidity up to $|\eta| < 1.479$.

The endcaps of ECAL are located at a distance of 314 cm from the nominal interaction point. Each of the endcaps consists of two D-shaped halves. As each Dee consists of 3662 crystals, the entire endcap part of ECAL contains 14648 crystals with an overall volume of 2.90 m^3 and weight of 24.0 t. The endcap crystals are all identical and have a cross section of $28.6 \times 28.6\,mm^2$ at the front face and a length of 220 mm, which corresponds to 24.7 X_0. They are arranged in an $x - y$ grid (as opposed to $\eta - \phi$ grid). The endcap of the ECAL provides coverage in pseudorapidity in the range of $1.479 < |\eta| < 3.0$.

In front of the endcaps of ECAL there is a preshower device: a sampling calorimeter with the total thickness of 20 cm, formed by two layers of lead (aproximately $2\,X_0$ and $1\,X_0$ thick) followed by planes of silicon strip sensors with an orthogonal orientation of strips with respect to each other. The principle goal of the Preshower is to identify neutral pions and distinguish their decay products from photons coming from the primary vertex.

The choice of lead tungstate crystals allowed CMS to have a compact and fast calorimeter with fine granularity and good radiation resistivity and an excellent energy resolution of $2.8\%/\sqrt{E} \oplus 0.12/E \oplus 0.3\%$.

4.5 Hadron Calorimeter

The hadron calorimeter (HCAL) follows the ECAL on the path of particles' passage through the CMS detector. HCAL is a sampling calorimeter: it consists of layers of brass absorber, where the hadronic shower is produced, interleaved with an active material (plastic scintillator), where the light is collected for subsequent detection. The layout of the HCAL is depicted in Fig. **4.3**. The active material is segmented such that the cells ("tiles") in consecutive layers form a tower in $\eta - \phi$. The signal from such many-storied tower is then read out in bulk or from several ranges of layers depending on the tower position in the HCAL. Each tile has an embedded wavelength-shifting (WLS) fiber which collects the light from the scintillator and is spliced to a clear fiber that transports the light to the readout. After re-grouping of fibers by the optical decoding unit (ODU) to form the bundle of fibers responsible for the tiles which will be readout together (the whole tower or a set of subsequent tiles in the tower) the photodetection is done by means of a hybrid photodiode (HPD). As many other subsystems of CMS, HCAL has a barrel-endcap structure, and the crack between the barrel and endcap is used for service cables of subdetectors located inside of HCAL. Therefore the crack is pointing away from the interaction point (it makes an angle of 53° with the beam) to avoid undetected particles due to non-instrumented $\eta - \phi$ segments. Instead the last tower of the barrel is overlapping with the first tower in the endcap.

In the barrel (HB) region the towers form a cylindrical grid consisting of 32 towers in pseudorapidity range $|\eta| < 1.4$ and 72 towers in ϕ, which results in a segmentation of 0.087×0.087 in $\eta - \phi$. The towers of HB make use of the entire space left between the ECAL and superconducting solenoid and are made of 17 layers of absorber and 17 layers of scintillator. First and last layers of absorber are made of steel (40 and 75 mm, respectively) for extra mechanical durability, others are made of brass (eight plates of 50.5 mm and six plates of 56.5 mm). This provides 5.8 interaction lengths (λ_I) for normally incident particles and increases to 10.6 λ_I as the pseudorapidity reaches $|\eta| = 1.3$.

Because the absorption depth of HB was limited by the space left between the ECAL and superconducting coil, especially for almost normally incident particles, the combined

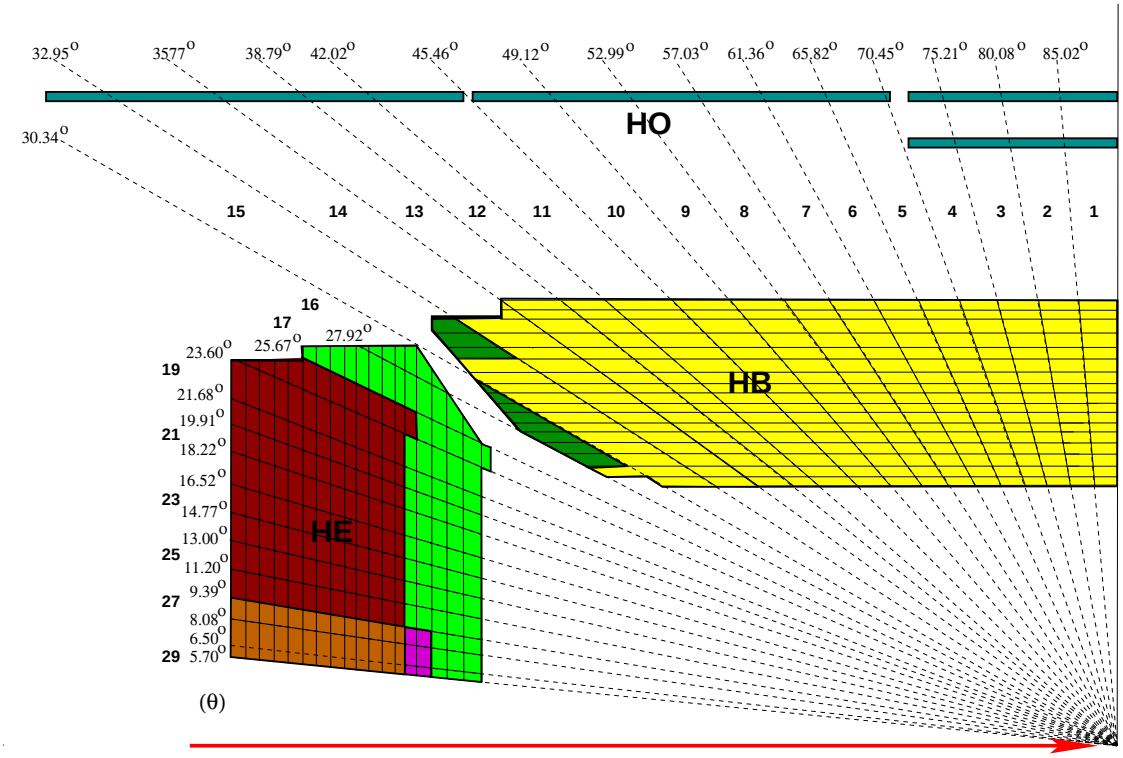

FIGURE 4.3: The HCAL layout (1/4 of the $r-z$ view). In each tower layers of scintillator dipicted in the same color contribute into a common depth readout.

absorber depth of the ECAL and HB is insufficient for some highly energetic hadron showers. Therefore the "tail catcher" calorimeter, the Hadron Outer Calorimeter (HO), is placed outside of the solenoid and hence the superconducting coil is treated as an additional absorber providing $1.4/\sin\theta$ interaction lengths. The HO is designed to match the construction of the 2.536 m wide rings which form the return yoke of the magnet and serves as a first, sensitive layer of each ring. The segmentation in $\eta-\phi$ follows the segmentation of HB. In the range covered by the central ring the interaction depth of the HB is especially thin. Therefore the central ring of HO (ring 0) is equipped with an extra plate of iron 19.5 cm thick which is sandwiched between two layers of scintillator at radial distances of 3.82 and 4.07 m from the nominal beam. The other rings of HO are made of a single scintillation layer positioned at 4.07 m from the beam. The total absorber depth is thus increased to a mimimum of 11.8 interaction lengths.

The endcaps of the hadron calorimeter (HE) supplement the hermetic design of HCAL on both ends of the cylinder. The same tile-fiber technology as for the HB is employed for HE. The 79 mm thick brass absorber plates are interleaved with plastic stintillator and provide along with EE about 10 interaction lengths for stopping hadron showers at $|\eta|$ up to 3.0. Each of the endcaps has 14 towers in η. Five rings of outermost towers, corresponding to smallest values of η, have 5° segmentation in ϕ, the others are segmented in 10° tiles. Segmentation in η is the same as for the HB in the five outmost rings of towers. Then, as η increases, the step in η changes between 0.090 and 0.35. Most of the HE is also segmented in depth. This was partially motivated by the opportunity to compensate for the radiation damage when the scintillator will begin to darken in the forward region where the detector is exposed to extreme radiation conditions. The towers closest to the beam feature 3 depth readouts, while the others, down to $|\eta| = 1.5$, have 2 depth readouts (see Fig. **4.3**).

Coverage in pseudorapidity range $3.0 < |\eta| < 5.0$ is provided by the Hadron Forward (HF) calorimeter. The front face of the HF is located 11.2 m from the interaction point along the beam direction. The HF itself is a cylindrical structure 165 cm long (about 10 interaction lengths) with an outer radius of 130 cm and the inner radius of 12.5 cm. The calorimeter consists of a steel absorber structure populated with 0.6 mm thick quartz fibers which form a lattice 5 mm$\times$5 mm. There are two types of fibers in the HF. The longer ones run all the way through the absorber, the shorter ones start 22 cm from the front face of the HF. The two kinds of fibers are arranged checkerwise and read out separately. Since electromagnetic showers are nearly contained in the first 22 cm of the HF, such design allows to discriminate between electromagnetic and hadronic showers. The fibers are grouped to form a grid in $\eta - \phi$ with a segmentation of 0.175$\times$0.175 (except for the lowest-η and highest-η tower where the step in η is equal to 0.1 and 0.3, respectively, and the step in ϕ equals 0.35 for the tower with highest η). Each bundle of fibers is mated to an air-core light guide which brings the Cherenkov light from the fibers to the PMT-based readout behind the steel-polyethylene shielding. The entire design of the HF was driven by the necessity to operate in severe conditions of a high radiation environment.

4.6 Muon System

The CMS muons system is hosted in the return yoke of the magnet and hence the layout preserves the five-ring segmentation of the yoke (Fig. **4.4**). In the barrel four muon stations are located at the radial distances of 4.0, 4.9, 5.9 and 7.0 m. In the endcap four disks with muon stations are positioned between 5.5 and 10.5 m from the interaction point.

The vast area which required instrumentation put the low-cost technology alongside with the need for fast triggering and good resolution as well as requirements driven by operation in distinct radiation environments and magnetic fields. This is why three kinds of gaseous detectors were employed.

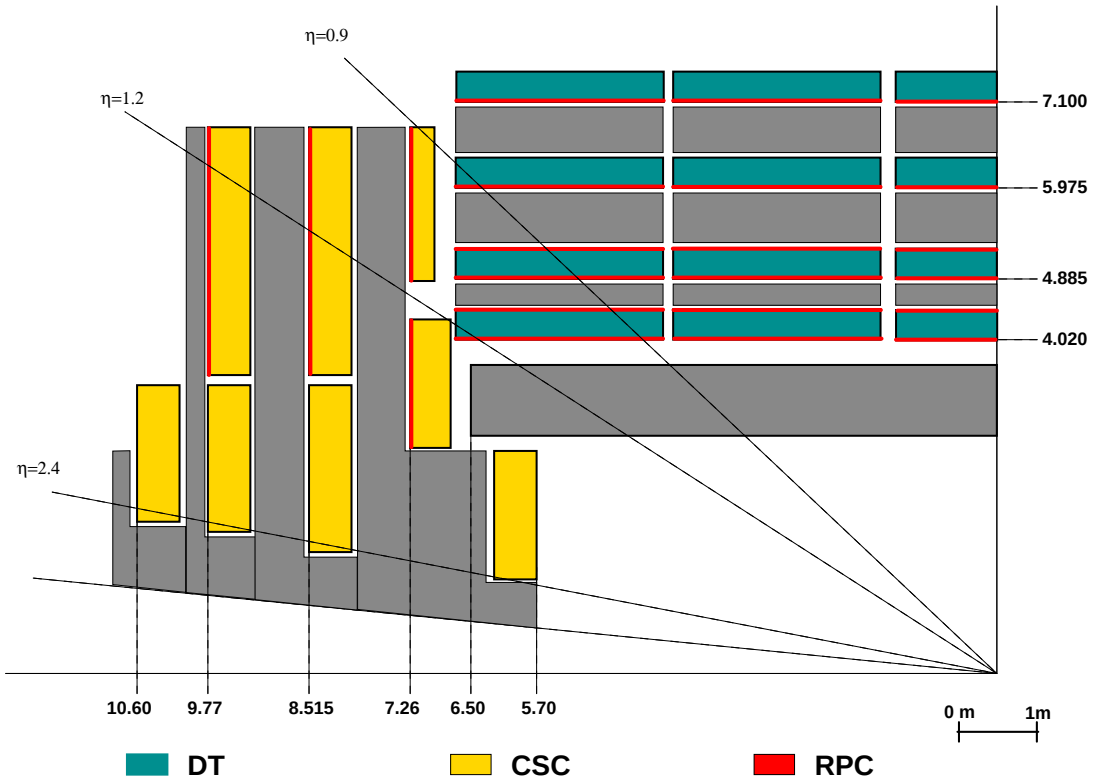

FIGURE 4.4: Muon System layout (1/4 of the $r-z$ view).

Drift tube (DT) chambers are used in the barrel region, where the residual magnetic field in the gaps of the return yoke is low and the neutron induced background is small (in Fig. **4.4** they are shown in cyan). An individual cell of DT is a 2-3 m long aluminum tube

with a rectangular cross-section of 13 mm×42 mm filled with an Ar+CO_2 mixture. The anode wire in the center collects the ionization charges left behind by the charged particle penetrating through the chamber. The layers of such tubes are staggered by half-width of the cell, four layers form a "superlayer" (SL), in which all tubes have the same direction. SLs are used to form a DT chamber: SLs on the opposite sides of the chamber have the tubes along the beam and hence provide measurements in $r-\phi$ plane. Those SLs are sandwiched with an aluminum honeycomb spacer (for better ϕ resolution) and one SL with the direction of tubes orthogonal to the beam. This third SL provides the measurement of z and is not present in the outermost, 4th, layer of DT chambers. Each of five rings of the magnet yoke is equipped with four layers of DT chambers: 12 chambers per layer in three inner layers with each chamber covering 30° in ϕ. In the fourth layer the top and bottom segments in ϕ are instrumented with two chambers each, hence 14 DT chambers per ring in the outermost layer. Each DT provides a position measurement with 100 μm precision and the direction in ϕ with 1 mrad resolution.

Cathode strip chambers (CSC) are used in the endcaps, where operation in high magnetic field is essential (in Fig. **4.4** they are shown in gold). Trapezoidal chambers are arranged on 4 disks into concentric rings, 3 rings on the innermost disk and 2 rings on the others. The innermost ring on the disks 2 through 4 is segmented in ϕ into 18 chambers, other rings carry 36 chambers. Each chamber is formed by 7 trapezoidal 16 mm thick cathode plates with about 80 strip cathodes milled on each side. The pitch of the strips varies from 8.4 mm to 16 mm. The 9.5 mm gaps between the plates are filled with an Ar+CO_2+CF_4 gas mixture and carry the planes of 3 mm spaced anode wires which are orthogonal to the strips. Hence cathode strips provide ϕ measurements while anode wires measure radial position. Each chamber provides a spatial resolution of 200 μm and an angular resolution in ϕ of about 10 mrad.

Resistive plate chambers (RPC) are parallel-plate detectors (in Fig. **4.4** they are shown in red). They are fast, but the spartial resolution they provide is somewhat coarse. Hence those detectors are mainly used in the trigger to provide information independently from DT and CSC. An RPC module consists of two plates with a common plane of readout strips in between operated in avalanche mode. In the barrel RPCs instrument the front faces of all

muon stations and the rear sides of the first two stations. In the endcaps RPCs are located behind the CSCs and provide coverage up to $|\eta| = 1.6$.

4.7 Trigger

With the LHC bunches crossing every 25 ns or 50 ns and more than 20 interactions per bunch crossing the CMS detector witnesses about 10^9 interactions/sec; and yet the detailed data can only be recorded for only about 300 crossings/sec. Hence the trigger system has to discriminate the events to pick out approximately one event of interest in a million which will be stored for future analysis. The trigger system of CMS discards the unwanted events in two steps: Level-1 (L1) trigger and the High-Level Trigger (HLT).

The L1 trigger is implemented in customized electronics (FPGAs, ASICs and programmable memory lookup tables). It is housed partially in the front-end electronics of the detectors and partially in the service cavern 90 m away from the experimental cavern. The total time allocated for taking the decision as well as the transit is 3.2 μsec. During the decision-taking period the high-resolution data are stored in a buffer. L1 uses coarsely segmented data from the calorimeters and muon system in the form of "trigger primitives" to identify trigger objects (electron, photon, jet and muon candidates above certain E_T or p_T) and global quantities (total and missing transverse energy, jet multiplicities, scalar sum of the transverse energies of jets above a preset threshold).

Once the decision to keep the data is received from the L1, the data in the buffer is streamed to a computer farm of about 1000 processors which run the HLT software. The HLT has access to all the read-out data and can apply sophisticated algorithms to reconstruct the objects of interest. The implementation of the HLT as a processor farm is highly beneficial, since this approach allows CMS to take advantage of computing technology advances and the evolution of reconstruction algorithms.

Chapter 5

All hadronic SUSY search

Even with the high luminosities provided by the state of art in accelerator technologies, the LHC, and sophisticated design of its major experiments and their trigger sytems, search for the new physics remains a challenging task, as the signatures of new physics are normally hidden in poorly populated regions of phase space. The performance of such searches directly depends on the performance of the detectors and amount of recorded data. Limitations in the resolution of the subsystems of the experiment lead to more strict selection criteria for the data to ensure that those limitations do not distorte the search regions. As a result, the poorly populated search regions become even more deserted. As an example, SUSY searches in hadronic final states with missing transverse energy suffer from the mismeasurements of the latter, which in turn originates from the mismeasurements of the jets. To reach conclusive results, physicists make use of the big guns of statistical methods and unusual treatment of the MC, which leads to non-transparent and hence possibly error-prone flow of the analysis. This chapter presents in a nutshell the search for the scalar superpartner of a top quark, as conducted by the SUSY Reference Analysis-2 Group at

CMS in 2012-2014, which remains unblinded.

5.1 Stop Pair Production – Motivation of the Search and Signature

To date, there are no experimental observations of supersymmetric particles. However, some important limitations have been established by the recent searches at CMS[29] and ATLAS[30] experiments at the LHC. Search results place a lower limit on gluino masses at 1.1 TeV for some decay topologies in the decoupled squark limit; for the squarks of the first and second generations the lower limit is set at $\sim$800 GeV in the decoupled gluino limit. This validated that supersymmetry has to be a broken symmetry, and the cancellation of radiative correction to the Higgs boson mass cannot be exact. Since the Yukawa coupling of the top quark is large in the SM, it is the scalar superpartners, $\tilde{t}_R$, $\tilde{t}_L$, that play the dominant role in naturalizing the quantum effects of the mass of a Higgs boson. Therefore, if supersymmetry is to resolve the hierarchy problem, the mass of a scalar top quark has to be of the same order as the mass of the top quark. So far the searches for the scalar top have only probed a small portion of the possible phase space[31]. However, if the mass of the scalar top is similar to that of a top quark, stop pair production can be hard to distinquish from that of the top quark pairs with modern detectors; hence, stop quarks could have evaded detection in previous searches.

In the SUSY models with conservation of R-parity after a cascade of decays the final decay products of a pair of scalar quarks should contain two LSPs, which will exhibit themselves as missing transverse momentum. As the aim is basically to identify stops among the mis-identified tops, a second ingredient of the final state is a signature for a pair of top quarks. The top quark only decays into a W boson and down-type quark with a dominating contribution coming from the b quark, as $V_{tb} > 0.999$. If the LSPs are the only source of the missing transverse momentum, i.e. if there are no neutrinos among the decay products of W and b-jets, the total missing momentum of the event can be associated with the LSPs and be the signature of supersymmetric particle production (Fig. **5.1**, top). The

resulting signature is therefore a pair of b-jets, four additional jets and missing transverse energy ($b\bar{b}jjjj + \not{E}_T$).

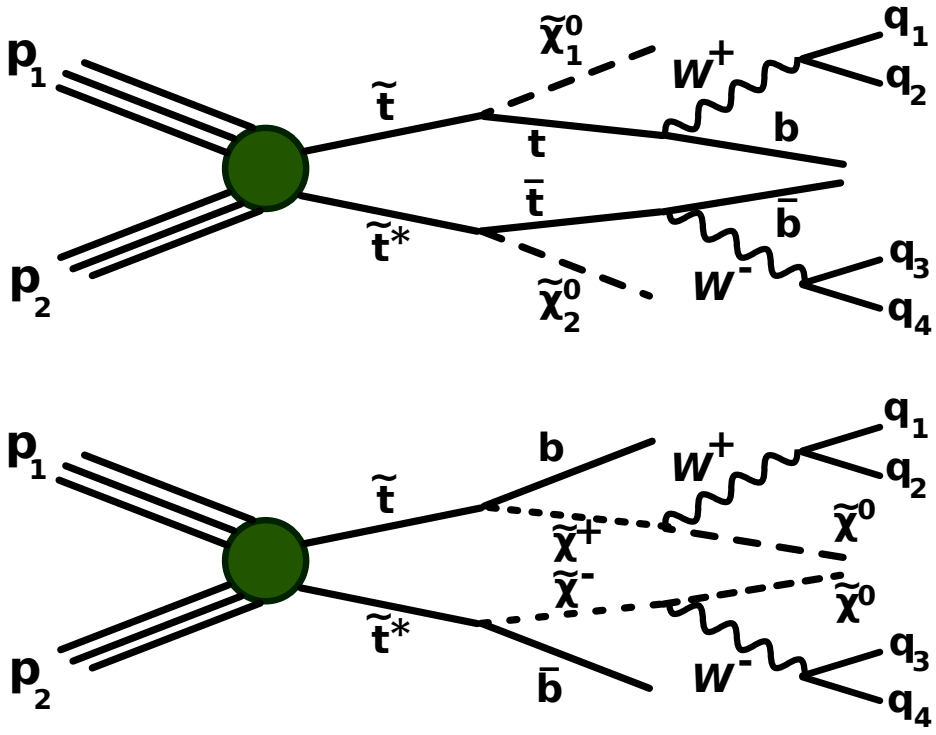

FIGURE 5.1: Diagrams with scalar top pair production, which contribute to the signature $b\bar{b}jjjj + \not{E}_T$. **TOP:** Diagram with stops decaying through on-shell top. **BOTTOM:** Diagram with stops decaying through intermediate chargino.

However, such a signature does not give exclusive sensitivity to the stop decay through an on-shell top quark (from now on this option is referred to as T2tt). This signature is likewise suitable for the scalar top decay through an intermediate chargino (referred to as T2bw). Hence, the presented search is sensitive for both options.

5.2 Datasets and Triggers

The datasets used for this study for the search region, as well as corresponding triggers and luminosities are shown in Appendix A.

As it was explained above, the CMS DAQ does not attempt to record all the events occurring in the detector. Instead it records only events with an interesting signature. How-

ever, the definition of ”interesting” does change with time. For example, to check that the detector works properly, some of the events which are of no interest for a physical analysis, are collected. Some other events do not seem to contain anything new, but could be handy for cross-checks of the actual physical searches. If events falling into those categories take place too often compared to more promising events, a good compromise is to record not all of them, but just some lot. Besides, CMS offers an opportunity to vary the fraction of events with a particular signature which ends up recorded according to the current needs. A trigger, responsible for identifying a particular signature, which is fractionally sampled, is referred to as a prescaled trigger. Both triggers which were used for collecting the above mentioned dataset remained unprescaled during the entire period of data taking.

Let us mention here one more pecularity of the CMS triggers. As the underlying algorithms of those triggers is supposed to be very fast to be able to take the decision whether the event is worth keeping, various quantities which the trigger relies on are calculated approximately, based on simplified, but faster, algorithms. If the decision is to keep the event, those same quantities are re-calculated again, now based on sophisticated and slow algorithms which provide the best, most accurate, result. No wonder the new values of the same quantities are a bit different. If one now considers the distribution of the quantity, the trigger was using for cut-off, it does not look like a step-function anymore. The distribution is smeared around the threshold value: not only some events which didn't have to pass the trigger, did pass, but also some events, which qualified to pass, got rejected. The sketch of this effect is depicted in Fig. **5.2**. It is then said that the trigger is inefficient close to this threshold. To avoid biasing the data sample, collected with such trigger, one has to impose a stronger cut on the quantity the trigger is using to take the decision, such that all the events selected fall within a range of sufficient efficiency of the trigger.

All other datasets are listed in Appendix B, finally all MC samples utilized are represented in Appendix C.

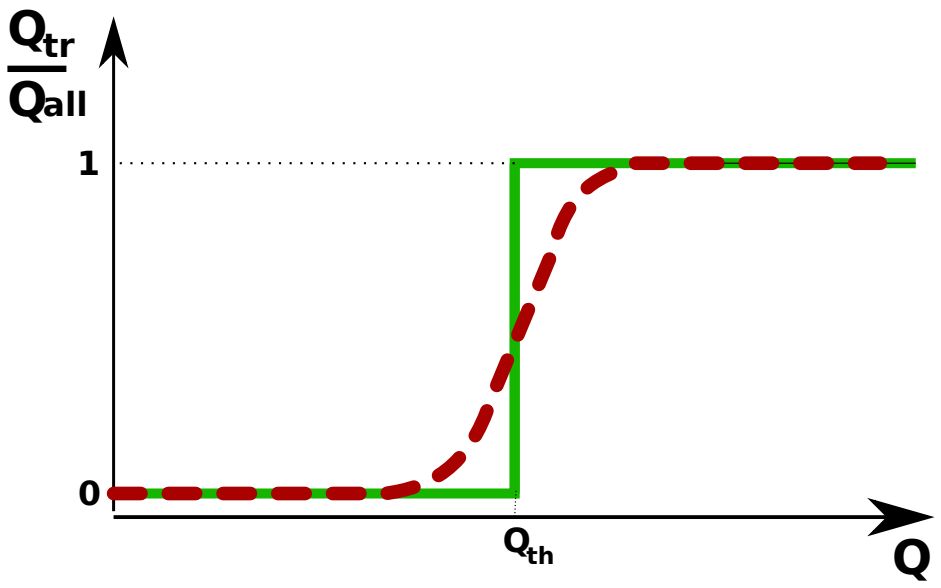

FIGURE 5.2: Sketch of a generic trigger efficiency, which is basically the fraction of triggered events, Q_{tr}, to all possible events, Q_{all}, as a function of the reconstructed value of quantity Q by the trigger (in green) and by the offline algorithm (in red). The hypothetical quantity Q is used for the decision making by the trigger. Once the event is stored, the offline algorithm reconstructs the value of Q more precisely, and the efficiency smears around the trigger threshold.

5.3 Identification and Reconstruction

5.3.1 Jet Reconstruction. ”Picky” jets

Two kinds of jet algorithms were used: the search for the T2bw signal uses standard anti-k_T jets, while the search for T2tt utilizes custom ”picky” jets. Anti-k_T jets are corrected for the effects of pileup according to standard procedures[32].

Since the beginning of operation, the anti-k_T algorithm with $R = 0.5$ has become a standart tool for most of the analysis in CMS. However, in some cases its performance is insufficient. In particular, if one considers a fully hadronic decay of a top quark and decides to elaborate a study with a pair of top quarks involved, both decaying hadronically, the fraction of the detector populated with the debris of such event will be quite high. The chances that all three jets from top decay will be properly resolved and will not overlap in such case are not inspiring. Top quarks naturally tend to produce jets which sufficiently vary in momentum, and this is even more so, when the two of them are produced in the same

event and with asymmetric momenta. As a result not only the neighboring jets originating from different partons can be merged together in case of high occupancy of the detector, but also a softer, wider jet can end up being split, and both situations can take place in the same event. Therefore jet clustering with fixed size parameter is not suitable: if reconstructed jets are small enough to avoid overlapping between them, then they are unable to properly reconstruct the jets originating from soft partons and tend to split them.

Therefore it is highly desirable to adopt a "picky" jet-clustering scheme, which would allow to accomodate the radius from jet to jet in the same event. The algorithm summarized here is covered in[16]. It starts with pre-clustering the "fat" jets according to Cambridge/Aachen with a size parameter 1.0 and uses the subjettiness metric[17] for jet splitting.

In general subjettiness measures are defined as

$$\tau_n^{(\beta)} \equiv \frac{\sum_i p_{T,i} min\left\{(\Delta R_{1,i})^\beta, (\Delta R_{2,i})^\beta, \ldots, (\Delta R_{N,i})^\beta\right\}}{\sum_i p_{T,i}(R_0)^\beta},$$

where the sum runs over all the constituents of a proto-jet. However, as far as the "picky jets" are concerned, $\beta = 1$, and $R_0 = 1$. The second, splitting, part of the algorithm then proceeds as follows:

- Maximize the subjettiness metric τ_2;
- Compute the discriminator and based on its value decide if the performed splitting should be preserved. In case of a positive decision, replace the original proto-jets with two proto-jets resulting from its splitting; otherwise discard the changes and move the protojet to a list of final jets;
- Repeat the procedure with remaining proto-jets;
- Once a proto-jet cannot be further split, it has to be moved from the list of proto-jets into the list of final jets.

A natural choice of the discriminator is offered by the definition of N-subjettiness measures themselves: by construction τ_n tends to zero as the constituents of the proto-jet cluster

along one of the n predetermined axes. Hence a small value of $\frac{\tau_2}{\tau_1}$ would indicate that the constituents are in accord with a two-parton hypothesis rather than a single parton.

Jets are further pileup-corrected on an event-by-event basis by subtracting the appropriate energy in much the same manner as it is done for anti-k_T jets.

5.3.2 B-tagging

For T2bw signal regions jets originating from b-quark decay are identifiend by the Combined Secondary Vertex (CSV) algorithm[62], which uses secondary vertices identified within the jets and track impact parameters. Additional categories can be defined and combined into a likelihood discriminator for the cases where a "pseudo vertex"[1] is found, or there is no vertex at all, to provide stronger discrimination from the much larger background of gluon, charm and light quark jets.

In case of T2tt signal regions, for which "picky" jets are used instead of anti-k_T, the only difference in applying the algorithm in this case is that while for anti-k_T jets all tracks inside of the $R = 0.5$ cone around jet axis are included into the calculation of the discriminator, for "picky" jets only the tracks associated with PF particles are included.

5.3.3 Top reconstruction

Top candidates are reconstructed out of three "picky" jets with a dedicated CORRAL algorithm[16]. As there are many jets in the events of interest, consideration of all combinatorial combinations of three jets as top candidates is time-consuming. Therefore the algorithm proceeds in stages, keeping the best candidates at each stage. Each of the seed jets, which is of high p_T, is paired with two other, lower p_T, jets, which meet the angular and invariant mass requirements. The pair of top quarks is then selected such that the tops are formed by disjoint sets of jets, and the pair satisfies the requirements on the di-top invariant mass, angular properties of the top candidates and b-tagging of jets.

[1] If the real vertex is not found, sometimes it is possible to combine two tracks and calculate vertex-assocated quantities even without the actual vertex fit.

5.4 Main Backgrounds and Baseline Selection

The described signature eliminates many kinds of potential backgrounds. However, the expected cross section of scalar top production is very small compared to SM processes. Therefore apt attention has to be payed to background suppression methods. The SM processes which contribute into the background in this case include:

- Top quark and W boson production with the subsequent leptonic decay of W, where the lepton is either lost or not identified.
- Z boson production with subsequent invisible decay.
- QCD multijet production.
- Top pair production in conjunction with Z boson, which decays invisibly.

While some of the backgrounds have indeed the same signature as the signal of interest, the intervention of others comes from the detector imperfections, which lead to misidentification of some objects and the escape of others. A set of loose selection criteria is used for initial suppression of the SM backgrounds.

Slightly different sets of preselection criterias are used for T2tt and T2bw:

T2bw preselection constraints:

- Events with an isolated leptons are rejected. This suppresses SM backgrounds which may produce prompt leptons.
- $\not{E}_T > 175\,\text{GeV}$. This requirement comes mainly from the search trigger. The remaining sample is more than 95% efficient for signal, once this cut is imposed.
- At least five jets with $p_T > 30\,\text{GeV/c}$ in the barrel region of the detector, with at least two of them with $p_T > 70\,\text{GeV/c}$. As it was stated above, the distinct signature of a hadronically decaying pair of top quarks is the presence of six jet events. However, it is not uncommon that some of those jets can be soft. A good illustration of this feature is the decay of a boosted W, in which one emitted quark approximately follows the direction of the boost and hence is observed with high p_T, while another

travels against the boost direction and therefore is registered as a soft one. Hence two different transverse momentum thresholds are employed. Besides, SM backgrounds naturally tend to produce lower jet multiplicities. Therefore this constraint brings us one step closer to the desired multijet signature of the event and besides strongly suppresses QCD background.

- One b-tagged jet with $p_T > 30\,\text{GeV/c}$ in the barrel region. Again approaches us to the desired signature.

- Missing transverse energy should not be collinear with any of the three most energetic jets. In particular:

$$Min(|\Delta\phi(\not{E}_T, jet1)|, |\Delta\phi(\not{E}_T, jet2)|) > 0.5,$$

$$|\Delta\phi(\not{E}_T, jet3)| > 0.3.$$

  This constraint removes events with severe jet mis-measurement. Such mis-measurements are more likely to happen with a single, highly energetic jet in the event. Therefore the artificial $\not{E}_T$, which arises this way is collinear with the mis-measured jet.

T2tt preselection constraints are very similar in both motivation and implication and only differ when it comes to the assumption of an on-shell top quark presence:

- Events with isolated leptons are rejected.

- $\not{E}_T > 175\,\text{GeV}$.

- At least two highly energetic jets with $p_T > 70\,\text{GeV/c}$ and in the barrel region of the detector.

- One b-tagged custom jet with $p_T > 30\,\text{GeV/c}$ in the barrel region.

- At least one customly reconstructed candidate for a top quark.

- Non-collinearity of the missing transverse energy with any of the three most energetic jets:

$$Min(|\Delta\phi(\not{E}_T, jet1)|, |\Delta\phi(\not{E}_T, jet2)|) > 0.5,$$

$$|\Delta\phi(\not{E}_T, jet3)| > 0.3$$

.

5.5 Final Selection: Boosted Decision Tree

Once the events are pre-selected according to the above-described requirements, they have to undergo the Boosted Decision Tree (BDT) trial.

Boosted Decision Trees are among the most powerful methods of statistical learning, at the same time they are rather intuitive and easier to visualize and interpret than others.

5.5.1 Basics of Statistical Learning and Decision Trees

Here only the concepts that are relevant to the discussed analysis are briefly summarized. A detailed coverage of this broad field of modern statistics can be found in [33]. Statistical learning in many cases can be defined as building a statistical model, based on which the prediction of an output value can be done based on a set of inputs. Suppose there is a set of input variables (predictors), $\overrightarrow{X}$, and an output, or response, Y, then

$$Y = f(\overrightarrow{X}) + \varepsilon,$$

where ε is an independent of $\overrightarrow{X}$ random error term with a mean value of zero, $f()$ is a fixed, but unknown function of $\overrightarrow{X}$. Statistical learning then represents a collection of methods for the estimation of $f()$.

The decision tree methods are based on collections of rules, according to which the input data are split (assigned to branches). Each of the branches can in its turn contain a new bifurcation point (internal node), where the next rule for the data in a particular branch is applied (Fig. **5.3**, left. Note that the trees are drawn upside-down). The process continues until the stop point is achieved (for example, when the number of events in each

of the branches falls below a particular threshold, or a particular depth is reached). One of the pros of the decision trees is the ease of visualization: each of the internal nodes corresponds to a binary division of a corresponding region in a predictor space (Fig. 5.3, right). Once the decison tree separates the entire predictior space into a collection of non-overlapping regions R_j, the prediction for an observation that falls into some region is the mean value of the training outputs, which falls into the same region.

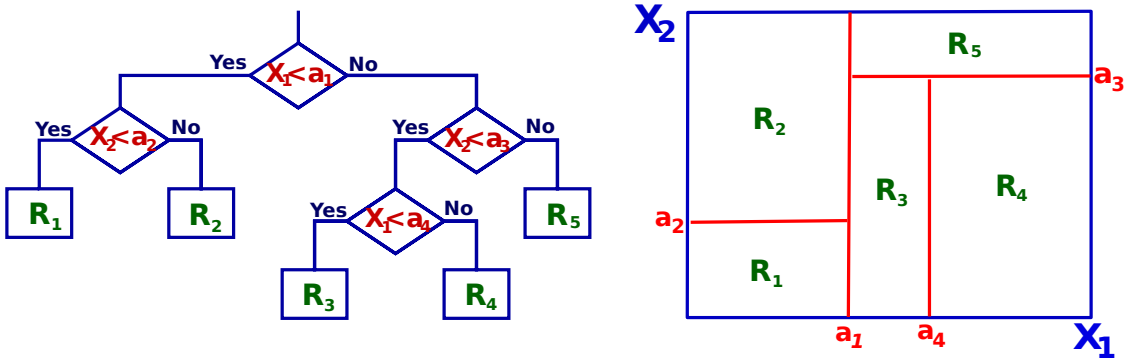

FIGURE 5.3: **LEFT:** Sketch of a simple decision tree. **RIGHT:** Visualization of a corresponding predictor space division.

Let $\widehat{y}_i$ be the prediction for Y based on some x_i, while y_i is the observation for Y. The prediction of this statistical model will be the most accurate if one finds the separation of predictor space R_j such that the residual square sum (RSS)

$$\sum_{j=1}^{J} \sum_{i \in R_j} (y_i - \widehat{y}_{R_j})^2,$$

is minimized. The task is therefore reduced to finding the set of R_j, which satisfies this condition the best. However, in the general case this would require comparing the results for an infinite number of predictior space partitions. One of the best options is referred to as ”top-down greedy splitting”. It starts with the construction of the tree from the top and at each step divides the predictor space in such a way that the RSS is minimal. Hence the algorithm is not attempting to optimize the resulting tree.

This kind of R_j division can be achieved fairly quickly, and will even produce good predictions on the training set. However, it might overfit the data, as the resulting tree can turn out to be too complex: it can result in higher variance than a simpler tree with less

branches.

Therefore the next step for the statistical model building is pruning the excessive tree. But again, searching for the best pruned decision tree can be extremely time-consuming, if one decides to compare all possible sub-trees of a tree produced on the previous stage. Therefore a "weakest link pruning" is often employed. Let T_0 be the original tree, produced with the top-down greedy splitting, T – a sub-tree of T_0, and α – a non-negative tuning parameter, which indexes the sequence of sub-trees:

$$\sum_{m=1}^{|T|} \sum_{i:x_i \in R_m} (y_i - \widehat{y}_{R_m})^2 + \alpha |T|$$

is minimized ($|T|$ is the number of leaves on a sub-tree T). For $\alpha = 0$ the tree sub-tree is identical to the original tree. However, as α increases, the minimization of this expression corresponds to some sub-tree with less leaves.

In this case the value of α can be determined by the k-fold cross-validation method: a set of training data is divided into k sets and for each of the sets the tree-growing and weakest link pruning are performed. Then each of the folds is treated as a validation set, while the other $k - 1$ are used for the fit. The mean square error is then computed for the validation set. As this process is repeated k times (once with each of the folds treated as a validation set), it results in k estimates for the mean square error. The result is then averaged for each value of α and the value of α is picked such that it minimizes the average error. The sub-tree, which corresponds to this value, is then chosen as a result of the pruning.

5.5.2 Boosted Decision Tree

Even after all steps described above the prediction of such decision tree would suffer from an important shortcoming – high variance. In practice it means, that if instead of using the whole training dataset at once, one splits it in halves and then fit a decision tree on each of the subsets separately, the outcomes in general might sufficiently differ.

There is a whole bunch of ways to approach this problem. One of them is a Boosted Decision Tree. In this approach instead of fitting a single huge decision tree to data, a collection of small trees is constructed sequentially, based on the information from the

trees, constructed previously. Instead of working with the response Y, the collection of current residuals (r_i) is employed: initially the prediction function is set to zero. In each cycle the small tree $\widehat{f}_b$ with d internal nodes is fit to the training data set (X, r). The small tree is then added to the main tree, and the residuals are updated:

$$\widehat{f}(x)^{new} = \widehat{f}^{old}(x) + \lambda \widehat{f}_b(x),$$

$$r_i^{new} = r_i^{old} - \lambda \widehat{f}_b(x_i),$$

where λ is a small positive number, a shrinkage parameter, which controls the pace of BDT learning. As the new trees take into account the trees that have already been grown, the number of internal nodes, d, in each tree can be quite small. As a matter of fact, $d = 1$ is not uncommon. Besides small trees simplify the interpretation: for instance, the use of $d = 1$ stubs results in additivity of the model.

In the current search at first $\sim$100 variables were pre-selected for BDT based on the signal against $t\bar{t}$ and $Z \longrightarrow \nu\overline{\nu}$ efficiency curves. After point by point comparison of the maximum significance for different combinations of variables, the final set of BDT inputs was selected. The complete sets of variables, used in the final BDT, are listed in Appendix D. All variables using quark likelihood are based on a CMS quark gluon likelihood calculation[34]. This system seems to be insensitive to any fine tuning: BDTs trained with signal points that have minor differences in mass have similar discrimination over a wide range of signal point. Therefore a sparse set of signal points across the mass plane was selected to find the final search regions. The picking of specific search regions is accomplished by determining the set of search regions that maximize the number of expected excluded signal points. The detailed description of the search region determination can be found in[35]. Finally, five search regions are defined for T2bw and four for T2tt.

5.6 Lepton Vetos

5.6.1 Electrons and Muons

The semileptonic decay of $t\bar{t}$ with an unidefied charged lepton is the main source of background in this search. The main challenge is to reject events with leptons coming from the decay W either directly, or through the intermediate τ decay, but at the same time keep leptons from hadron decays, as well as "fake" leptons. To achieve better separation between these two classes, a multivariate analysis based on Boosted Decision Trees is employed. The training was done separately for electrons and muons, which are pre-selected in the barrel region of the detector and with $p_T > 5\,\text{GeV}$; variables used in the BDT are listed in Appendix E. The working point for both the muon and the electron vetoes are chosen to obtain 98% efficiency for W-lepton tagging.

5.6.2 Tau Leptons

Semileptonic decays of $t\bar{t}$, where an intermediate τ decays into final states with hadrons become the main background to the search after applying e and μ vetos, described above. As the prevailing majority of those decays are one-prong, the presence of a single track was selected as a main component of the τ veto. Tau-candidates were identified as PF candidates in the barrel region of the detector with $p_T > 5\,\text{GeV}$ and

$$m_T = \sqrt{2 * p_T(track + nearest\ \gamma) * \not{E}_T(1 - \cos(\Delta\phi))} < 68\,GeV.$$

The selection of τ is made with the BDT, trained on samples of $t\bar{t}$ MC and a representative T2tt signal point. The list of varibles used in BDT is listed in Appendix E.

5.7 Background estimation

The method for background estimation of the electroweak processes and QCD multijets used in this anlysis is based on MC and shares a common event reweighting method which account for the observed discrepancies betwen data and simulated descriptions of various

SM processes. Correction factors fall into two conceptually different classes:

- detector reconstruction effects for lepton, b-tagging, trigger efficiences, jet resolution, etc.
- modeling of process kinematics such as the p_T spectrum of t-quarks, W and Z bosons, jet multiplicities, b-production cross section, etc.

The physically meaningful effects are identified, and the simulation is corrected for them. Closure tests are then performed in a large range of data and across several channels. This gives confidence that the corrections are also applied properly even in the (search) regions which are poorly populated. For the first class the standardized scale factors from the measurements performed by other groups in the collaboration are used, whenever possible. The effects of the second class come from the generation step of the simulation, such as finite order approximation in the matrix element calculations, phenomenological models and so forth. The goal is to derive the scale factors parameterized by generator-level quantities[1] rather than observables, such that after the reweighting of MC events after the simulation step their distributions agree with real data in some control region. In an ideal case for each background process there can be found a control region, which is pure and only gets contributions from this process. In reality this is nearly impossible: the background processes are tangled, and the connection between the yields of reconstructed, simulated MC events for the ensemble of backgrounds to the scale factors for various contributing processes is reflected in a matrix equation. The scale factors can be functions of some quantites (i.e. binned in them). As those quantites, strictly speaking, are not necessarily observables for the reconstructed events, the matrix in this equation is not square:

$$\begin{pmatrix} N_A \\ N_B \\ N_C \\ N_D \\ N_E \end{pmatrix} = \begin{pmatrix} n_A^{t\bar{t}} & n_A^W & n_C^Z(BIN_1(p_T)) & n_A^Z(BIN_2(p_T)) & n_A^{other} \\ n_B^{t\bar{t}} & n_B^W & n_B^Z(BIN_1(p_T)) & n_B^Z(BIN_2(p_T)) & n_B^{other} \\ n_C^{t\bar{t}} & n_C^W & n_C^Z(BIN_1(p_T)) & n_C^Z(BIN_2(p_T)) & n_C^{other} \\ n_D^{t\bar{t}} & n_D^W & n_D^Z(BIN_1(p_T)) & n_D^Z(BIN_2(p_T)) & n_D^{other} \\ n_E^{t\bar{t}} & n_E^W & n_E^Z(BIN_1(p_T)) & n_E^Z(BIN_2(p_T)) & n_E^{other} \end{pmatrix} \begin{pmatrix} SF^{t\bar{t}} \\ SF^W \\ SF^Z(bin_1(p_T)) \\ SF^Z(bin_2(p_T)) \\ SF^{other} \end{pmatrix}$$

[1] The use of generator-level quantities avoids the distirtion of well-known properties.

However, the straight-forward solution of a scale factor finding problem does not work: there is no reason why the inverse matrix should exist and, even in the case where it does, the method would suffer from large fluctuations. All of these are well-known peculiarities of the subject of unfolding. Therefore a stable unfolding method[38] is used here instead. Each generator-level bin scale factor is set to unity and iteratively corrected using Bayes' equation with the observed and simulated yields as input. A small number ($\tilde{4}$) of such iterations are sufficient to obtain reweighted distributions which show excellent agreement with data in control regions.

5.7.1 Top, W and Z($\rightarrow \nu\overline{\nu}$)+ jets

All search regions of this analysis have very low yields, especially in backgrounds like Z boson production. Therefore an MC-based prediction is used to improve the statistical precision of data-based methods. The method is based on using W or Z decays into visible leptons to correct the simulation description of these processes. The same corrections are then applied for the case of W/Z decaying hadronically/into non-reconstructed leptons/invisible decays of Z. Binning of the scale factors of generator level is used for the simulated processes to increase the number of events in the poorly populated regions of the phase space.

In data the control regions are based on the triggers for single electron and single muon, and the adopted definitions of objects are standard in order to allow the use of correction factors provided by the electron/muon Physics Object Groups:

Electron: $p_T \geq 15\,\text{GeV/c}$, barrel region, in accord with tight identification criteria[39], combined PF isolation$\leq 0.1 \times p_T$(or $\leq 0.07 \times p_T$ for electrons in the ECAL endcap with $p_T \leq 20\,\text{GeV/c}$).

Muon: $p_T \geq 15\,\text{GeV/c}$, barrel region, in accord with tight identification criteria[40], combined PF isolation $\leq 0.12 \times p_T$.

Jet: $p_T \geq 30$ GeV/c, composed by Particle Flow candidates (all but electrons and muons which pass medium electron or tight muon identification) clustered with the anti-$k_\perp$ algorithm with size parameter $R = 0.5$.

b-tags: $p_T \geq 30$ GeV/c, barrel region, with the discriminator of the Combined Secondary Vertex b-tagging algorithm > 0.898 ("tight" working point) or > 0.679 ("medium" working point). Only the jets with no leptons are used.

The selection criteria are then as follows:

- If the event passes the *HLT_IsoMu24eta2p1_v** trigger, it should contain a muon with $p_T \geq 28$ GeV/c and $|\eta| \leq 2.1$ in the offline reconstruction. If the event passes the *HLT_Ele27_WP80_v** trigger, it should contain an electron with $p_T \geq 30$ GeV/c and $|\eta| \leq 2.4$.
- At least two jets with no leptons.
- Distance between all pairs of leptons: $\Delta R(l_i,\ l_j) \geq 0.05$.
- If there are exactly two leptons of the same flavor in the event, $m(ll) \geq 56$ GeV/c^2.

For the MC smulation to adequately predict the rate of leptons from non-prompt sources (punch-through hadrons, anomalous fragmentation of jets into highly isolated particles, mis-reconstruction) the lepton selection criteria is relaxed for this process only as follows:

Electron: Loose identification criteria[39], combined PFisolation $\leq 2 \times p_T$.

Muon: Loose identification criteria[40], combined PFisolation $\leq 2 \times p_T$.

Jet: Same, but all the jets, which are closer to the above leptons than $\Delta R < 0.3$, are removed from the list of jets.

Those relaxed selection criteria increase the QCD yield with muons by about a factor 250-500 and with electrons by a factor 6-40. The yields are then normalized to those with the standard selection to provide a ballpark prediction. In the derivation of the top and

electroweak process reweighting factors only those control regions are used, where the contribution of multi-jet is at the percent level or less.

The scale factor sets (SFS) are defined by

- A control region, in which the weight scale factors are derived;
- A set of generator-level quantities, by which the scale factors are parameterized;
- A set of observables, which define a multidimentional histogram of yields in data and simulation.

To avoid ambiguities, each SFS is only applied to a single process, and derived in as a pure control region as possible. The other processes are treated as backgrounds that are subtracted from the data (using the simulated yields) before input to the unfolding procedure. Some consideration in the order of SFS derivation ensures that sizable backgrounds are corrected prior to deriving SFS in less pure control regions. Typically the largest tensions are corrected first and in the high-statistics regions.

The control regions and scale factor sets are listed in the Appendix **??**. The predictions in the $\not\!\!E_T$ triggered search region are made using the MC events after applying the detector effect corrections, the MC sample cross-section equalization and the generator level kinematics scaling factors.

5.7.2 Multijets

The method for a QCD background prediction employed in this search, uses the strategy from [37] as a baseline: the MC is progressively corrected and tuned to predict the data in thr high jet multiplicity and high $\not\!\!E_T$ set. However, the current method is adapted to face the challenge of the MVA-based search regions. This method is similar to the MC tuning technique employed for the electroweak backgrounds, and yet it has its peculiarities: for a QCD event to enter the search region, it should either undergo a heavy flavor decay, or a severe jet mis-measurement (while electroweak events enter it due to the intrinsic $\not\!\!E_T$ from neutrinos), and QCD extrapolation into the search regions and the determination of uncertainties on the predictions is different from that for the electroweak processes. Besides

all the standard corrections that are applied, the $\not\!\!E_T$ corrections were derived for the QCD samples specifically. For the control region with low $\not\!\!E_T$ the standard pileup correction on the number of generated vertexes was not used, due to technical limitations: the sample used here was collected during different run periods with different triggers. Therefore a specific correction is derived based on the number of reconstructed vertexes. For each subset of offline H_T corresponding to a specific set of triggers the MC is re-weighted so that the reconstructed number of vertexes matches the data in that H_T subsection.

The control region used to correct the QCD kinematics is of low $\not\!\!E_T$ and relatively high H_T. Two sets of H_T triggers were used in 2012: PF and Calo triggers. A set of non-prescaled PF-triggers (starting at a threshold of 650 GeV) was chosen for data collection. The lower threshold, pre-scaled Calo triggers were used for the remaining data sample. The turn-ons for each trigger are measured by looking at the efficiency of passing that trigger with at least 99% efficiency for events that pass some lower threshold trigger.

The method of kinematic unfolding differs form the one in[37] in two aspects. The first difference is that the correcton to the magnitude of the unclustered energy at the generator level was removed. For $\not\!\!E_T$ close to zero the reconstructed magnitude of the unclustered momentum agrees relatively well between the MC and data. The correction for the unclustered energy is hence applied only at moderate $\not\!\!E_T$ ($\tilde{50}$ GeV) to rectify the angular discrepancies for $\not\!\!E_T$ and the rest of the event. The second difference is that the b-jet corections are not applied, as they proved to be unneeded after applying all standard b-jet related kinematic corrections.

As $\not\!\!E_T$ is one of the central variables in the analysis used both on the stage of preselection and MVA analysis, it is important to correct it in MC in order to achieve a reliable prediction of QCD. The corrections applied to missing energy are as follows:

- Correction for the core of the jet resolution, which is more narrow in the MC than in data;
- Correction for the imprecise unclustered energy simulation;
- Correction for the bias in $\not\!\!E_T$ and b-tagged jet correlations;
- Correction for the jet resolution tail discrepancies.

5.7.3 $t\bar{t}Z$

The cross section of a Standard Model process of $t\bar{t}Z$ is low ($\tilde{0}.2\,\text{pb}^{-1}$), but it becomes an important background to the searches of high mass stop $\tilde{t}$: high mass of $\tilde{t}$ implies that its decay products, including LSP, are boosted, and therefore produce a sufficient imbalance in transverse energy, which is exactly the signature of the $t\bar{t}Z$ production with Z decaying invisibly ($Z \to \nu\overline{\nu}$). Hence it is an irreducible background to such search. The low cross section of this process does not allow one to find a control region to perform a standard MC reweighting procedure based on an enriched $t\bar{t}Z$ data sample. Instead the MC events simulated with NLO generator are used to obtain the prediction in the search regions.

Two MC samples are available for $t\bar{t}Z$:

- NLO MC generated by MC@NLO with the parton shower simulation done by means of Herwig.
- LO Madgraph with the parton shower simulated by Pythia.

The expected yields of those two samples vary in different search regions up to 49%, which is almost equal to the relative statistical uncertainty. The difference of these yields is used as one of the sources of the uncertainty. The signature of interest does not require more than six jets, therefore the estimation of a central value is taken from MC@NLO, as it is expected to describe the kinematics of low jet multiplicity better than the LO Madgraph.

To get an uncertainty on the $t\bar{t}Z$ cross section a triple lepton control region is used with events where a Z decays into a pair of same flavor opposite signed leptons, and the pair of tops decays semileptonically. For this control region the main background comes from di-bosons, which contribute about 20%. Its contribution is taken from the MC. To factor in the uncertainty of the di-boson cross section, the control region where it dominates the $t\bar{t}Z$ is produced by inverting the b-tag requirement. Both of those regions are selected from the triggers used by the triple lepton SUSY groups. According to them the following selection gives 100% trigger efficiency:

- At least three identified leptons;
- For the leading lepton $p_T > 20\,\text{GeV/c}$;

- For the sub-leading lepton $p_T > 10\,\text{GeV/c}$.

Further, electrons are required to satisfy the medium working point of the POG ID and isolation, and muons – the tight working point of the POG ID and isolation. Finally the pair of same flavor opposite sign leptons is required to be close to the mass of the Z boson: $80\,\text{GeV/c}^2 \leq m(Z) < 100\,\text{GeV/c}^2$.

5.7.4 Top and W: Hybrid Monte Carlo

The background in the search is expected to be dominated by events with leptonic decays of W, mostly coming from $t\bar{t}$ events. In this case the lepton can be out of the kinematic acceptance, not reconstructed and not rejected by the dedicated lepton vetos.

The control sample of $\mu + jet$ was selected from the datasets used for the search. The further selection criteria are as follows:

- Pass the search trigger. This is needed to access the data sample with low p_T of leptons.
- Have at least one μ in the barrel region and with $p_T > 5\,\text{GeV/c}$, and of high quality ("tight POG selection criteria"[36]).
- Satisfy $p_T(W) > 150\,\text{GeV/c}$.
- Have at least two jets (anti-k_T, $R = 0.5$) in the barrel part with $p_T > 70\,\text{GeV/c}$.

The above selection is loose enough to not bias the predictions after search cuts.

To predict the background originating from charged leptons, which escape rejection by dedicated vetos, the embedding of simulated electrons, muons and tau-leptons (which later decay leptonically or hadronically) into the data is employed. After that all search selection criteria, including lepton vetos, are applied to this hybrid sample. This allows the mimicking of the data environment in terms of jets, pileup, etc., which can otherwise be a large source of uncertainties.

The background from $t + W$ can be further divided into five categories: prompt e, prompt μ, $\tau \longrightarrow e$, $\tau \longrightarrow \mu$, hadronic τ. The procedure for embedding the τ is described

in[37]. In a nutshell, the muon in the data event from the control sample is replaced with a simulated tau-lepton with the same four-momentum, but with ϕ flipped around the direction of the original W: this preserves the momentum of W and the overall event description, and at the same time avoids shooting the τ back into the region of the detector that is biased by the selection of an isolated muon. For prompt e and μ the embedding of W is employed instead: the transverse momentum of W is used as an input for generating e and μ compatible with coming from the initial W decay. With only transverse information available, e and μ are built in at the same η, but with ϕ at the opposite side of W with respect to the initial muon. This is accomplished by means of a look-up-table (LUT): from the simulated $\mu + jets$ in the $t\bar{t}$, the decays of W are stored. For a given $p_T(W)$ (which is a vector sum of the $p_T(\mu)$ and $\overrightarrow{\not{E}}_T$) the LUT contains the transverse momentum of a corresponding lepton and $\Delta\phi(l, \not{E}_T)$ at generator level, which is then used to shoot a generated lepton at the same η as the original muon. The generated lepton is placed into an empty generated event at the vertex of the original event. Extra smearing is then applied to the vertex location, which is extracted from the $t\bar{t}$ simulation (in case this step is not done, the resolutions of d_{xy} and d_z for the lepton is too narrow, because embedding at the reconstruction vertex efficiently removes the resolution of this reconstucted vertex itself). The generated event is then fed to TAUOLA[41] and PYTHIA for the generator-level decay treatment. Then the event undergoes the full chain of CMS simulation and reconstruction. Next, the simulated and reconstructed lepton event replaces the original muon at the level of PF particles and tracks, and all the high-level reconstruction steps, such as pileup subtraction, jet clustering, $\not{E}_T$ calculation, vertex finding, b-tagging, etc. are redone on the embedded event. The events then undergo the same selection process as the ones in the search region to produce the prediction of the $t + W$ background. This embedding method increases the statistical precission: if the same event is used with different random seeds, slightly different background events are generated. As a result different events can survive the signal requirements and increase the pool of the control sample, which are used for the background prediction and hence reduce the statistical uncertainty.

5.8 Results

The expected signal yields and efficiencies are derived by applying the full event selection to the Monte Carlo simulated samples and are shown in Figure **5.4**. The MC-based background estimations are used to derive results for this analysis, for now the expected limits prior to unblinding. The systematic uncertainties for the top/EWK backgrounds are mostly symmetric, and are combined in quadrature for simplicity. The $t\bar{t}$, W and single top predictions are combined into a single entry. For the QCD background MC integration is performed to properly combine the sometimes strongly asymmetric uncertainties. Table 5.1 summarizes the central values and uncertainties assummed per background for all search regions.

Search Region BDT Training Point (Notation)	$t\bar{t}+W+t$	$Z\rightarrow\nu\nu$	$t\bar{t}Z$	QCD	$\sum$
T2bW:					
$M(\tilde{t})$ =550, 575 GeV/c^2 $M(\tilde{\chi}^0)=175,\ 200$ GeV/c^2 χ =0.25 (LX)	5.83 ± 1.86	1.81 ± 0.83	0.59 ± 0.19	2.71 ± 1.08	10.93 ± 2.31
$M(\tilde{t})$ =350, 375 GeV/c^2 $M(\tilde{\chi}^0)=75,100$ GeV/c^2 χ =0.75 (LM)	25.05 ± 5.82	4.32 ± 1.80	2.46 ± 0.78	0.36 ± 0.19	32.20 ± 6.15
$M(\tilde{t})$ =550, 575 GeV/c^2 $M(\tilde{\chi}^0)=125,150$ GeV/c^2 χ =0.50 (MXHM)	2.46 ± 0.84	1.61 ± 0.75	0.83 ± 0.29	0.15 ± 0.13	5.05 ± 1.17
$M(\tilde{t})$ =400, 425 GeV/c^2 $M(\tilde{\chi}^0)=25,\ 50$ GeV/c^2 χ =0.75 (HXHM)	7.60 ± 1.89	1.66 ± 0.55	1.72 ± 0.57	0.025 ± 0.011	11.00 ± 2.05
$M(\tilde{t})$ =550, 575 GeV/c^2 $M(\tilde{\chi}^0)=25,\ 50$ GeV/c^2 $\chi=0.75$ (VHM)	1.14 ± 0.47	1.18 ± 0.55	0.62 ± 0.21	0.024 ± 0.010	2.96 ± 0.75
T2tt:					
$M(\tilde{t})$ =300 GeV/c^2 $M(\tilde{\chi}^0)=25$ GeV/c^2 (LM)	18.84 ± 2.99	0.64 ± 0.22	1.34 ± 0.44	0.92 ± 0.58	21.73 ± 3.08
$M(\tilde{t})$ =425 GeV/c^2 $M(\tilde{\chi}^0)$ =75 GeV/c^2 (MM)	7.33 ± 1.62	2.19 ± 0.68	2.66 ± 0.94	0.17 ± 0.07	12.35 ± 2.00
$M(\tilde{t})$ =550 GeV/c^2 $M(\tilde{\chi}^0)=25$ GeV/c^2 (HM)	2.55 ± 0.88	1.86 ± 0.82	1.62 ± 0.58	0.042 ± 0.021	6.07 ± 1.33
$M(\tilde{t})=675$ GeV/c^2 $M(\tilde{\chi}^0)$ =250 GeV/c^2 (VHM)	0.75 ± 0.44	0.56 ± 0.30	0.99 ± 0.42	0.011 ± 0.005	2.31 ± 0.67

TABLE 5.1: Background yields and systematic uncertainties in all search regions as used for the limits calculations.

The modified-frequentist CL_s method[42] with one-sided profile likelihood ratio test statistics is used to test signal models: for each pair of masses $\{m_{LSP},\ m_{\tilde{t}}\}$ the value of the cross section of the model which results in $CL_s = 0.05$ is computed. The limits are

shown in Figure 5.5. One of the search regions is selected at each mass point based on the best expected upper limit performance. The search regions chosen for each of the mass points are shown in Figure 5.6. Further, at each mass point the value of the cross section is compared to the nominal production cross section (SUSY cross sections are computed using the Prospino package[43]), and the expected excluded area is represented with a solid line, while $\pm 1\sigma$ variations of the exclusion region are shown with dashed lines.

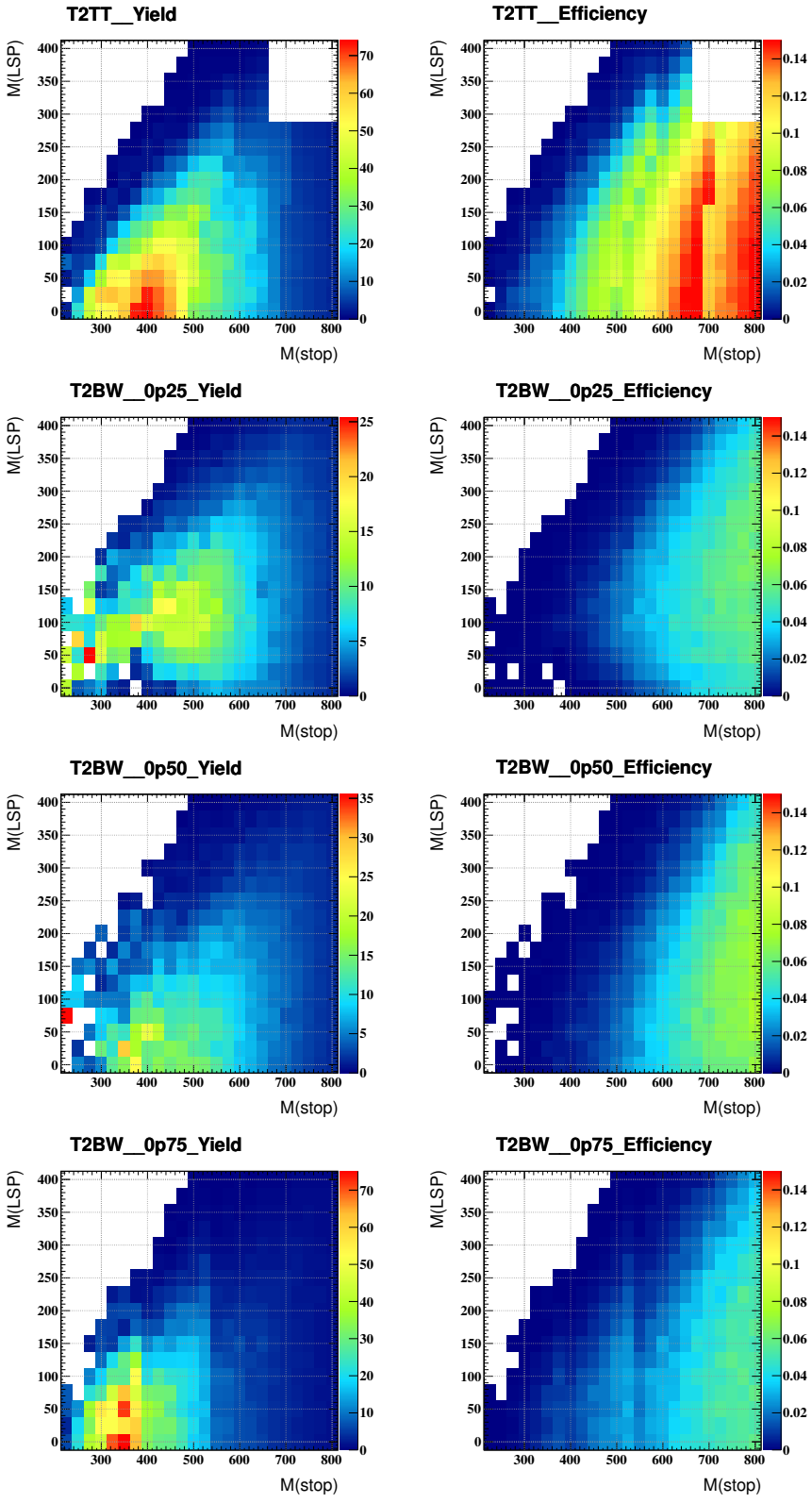

FIGURE 5.4: **LEFT:** Expected yields and **RIGHT:** efficiencies for the $\tilde{t}\tilde{t}^* \rightarrow t\bar{t}\chi_0\overline{\chi_0}$ (**TOP** row) and $\tilde{t}\tilde{t}^* \rightarrow \chi^+\chi^- b\bar{b}$ (three **BOTTOM** rows) signal topologies.

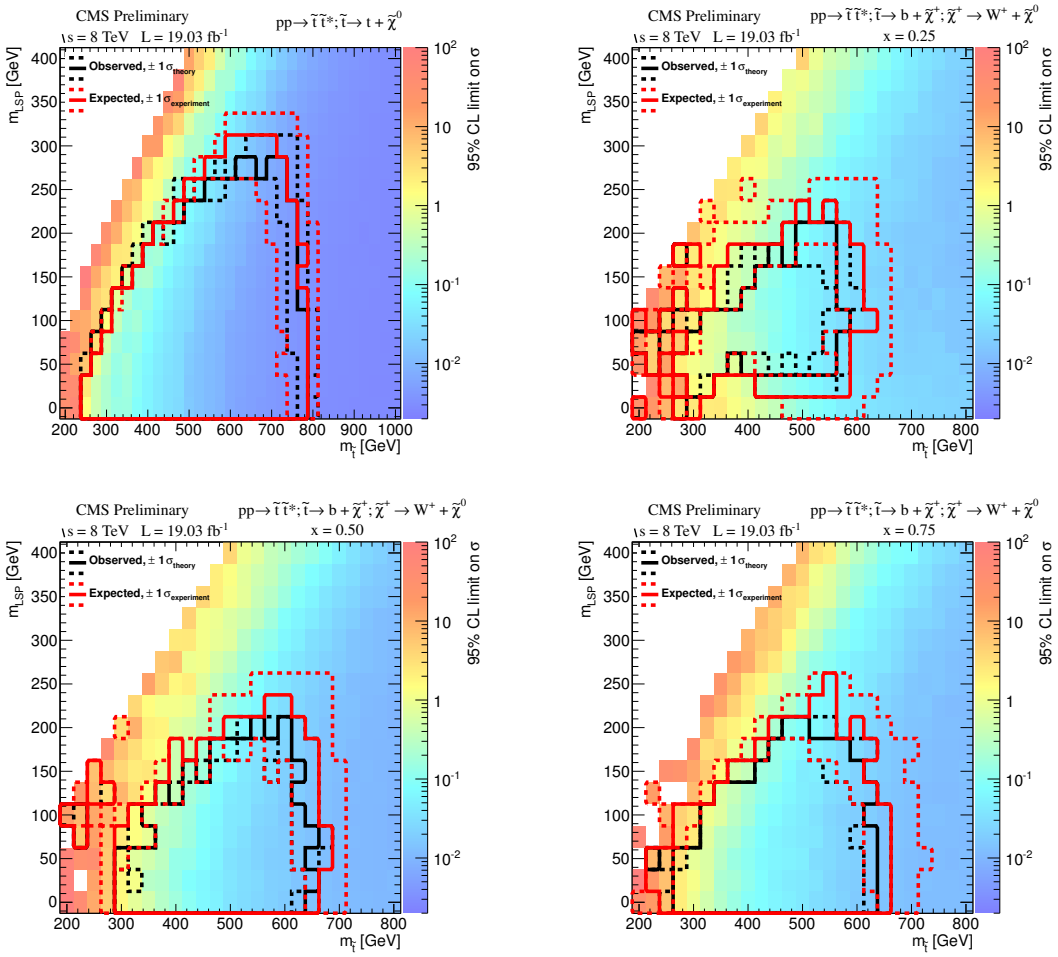

FIGURE 5.5: 95% C.L. upper limits on cross section for simplified models. **TOP LEFT:** $\tilde{t}\tilde{t}^* \rightarrow t\bar{t}\chi_0\overline{\chi}_0$. (**TOP RIGHT and BOTTOM**) $\tilde{t}\tilde{t}^* \rightarrow \chi^+\chi^- b\bar{b}$.

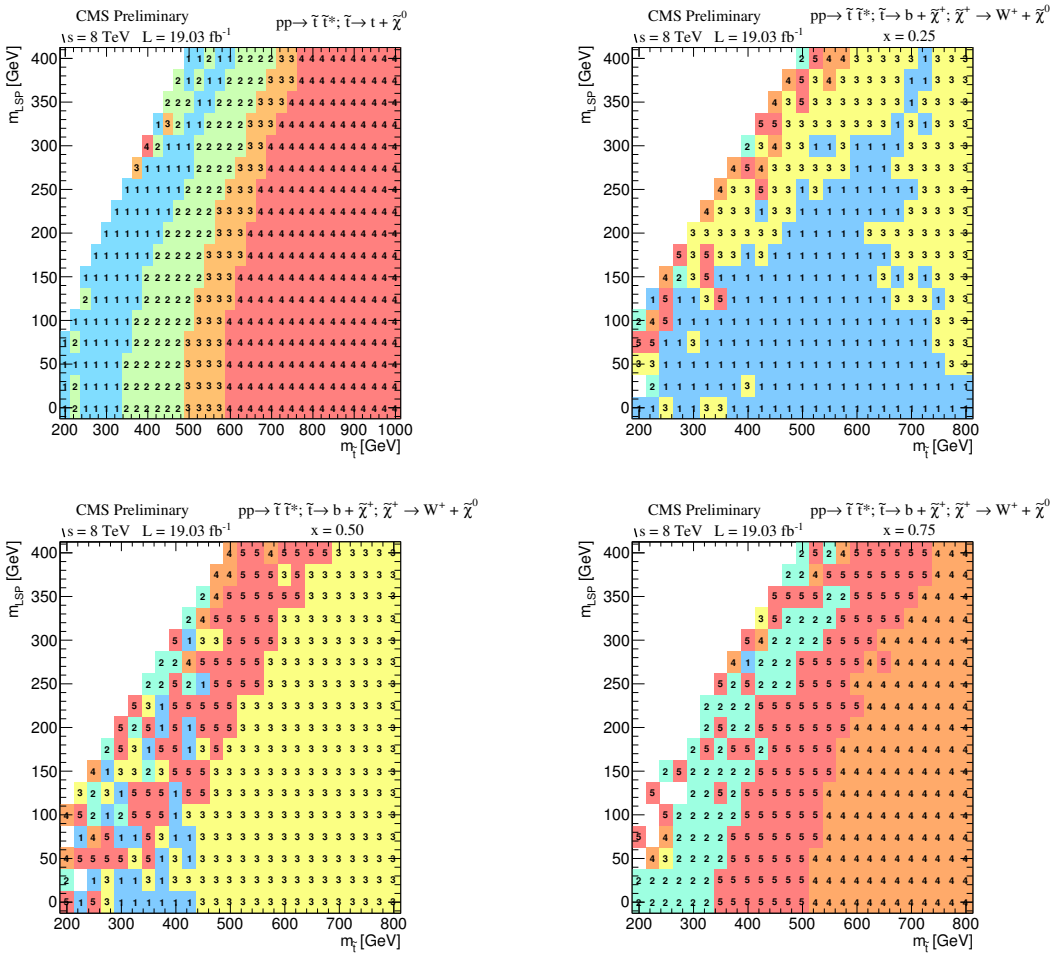

FIGURE 5.6: Search regions providing the best limits in the $m_{\tilde{t}} - m_{\chi^0}$ plane for **TOP LEFT:** $\tilde{t}\tilde{t}^* \rightarrow t\bar{t}\chi_0\overline{\chi}_0$ and (**TOP RIGHT and BOTTOM**) $\tilde{t}\tilde{t}^* \rightarrow \chi^+\chi^- b\bar{b}$. The notation for $\tilde{t}\tilde{t}^* \rightarrow t\bar{t}\chi_0\overline{\chi}_0$ is: $1 = LM$, $2 = MM$, $3 = HM$, $4 = VHM$; for $\tilde{t}\tilde{t}^* \rightarrow \chi^+\chi^- b\bar{b}$: $1 = LX$, $2 = LM$, $3 = MXHM$, $4 = VHM$, $5 = HXHM$.

Chapter 6

Beam Lines at CERN

As new detector technologies become available, and the detectors in use grow old, the experiments go through an upgrade stage by having minor or even substantial components replaced. No change is done to the experimental equipment before the replacement is tested in full and proved to be a reliable and beneficial renovation. An essential part of the evaluation and calibration process before the actual replacement is testing of the prototype in a beam of known properties – particle type, energy, etc.

The beam test can be considered as a high energy (fixed target) experiment of its own with the beam line being part of the setup. Like with any other equipment, it is important to understand the functioning of the beamline in use, be capable to ensure its proper usage and identify all posible malfunctioning; otherwise, the data collected during the beam test might become hard to interpret and even completely useless. It is of primary importance therefore to understand the beam formation process and any changes the beam line equipment can introduce at any stage for taking reliable measurements during the beam tests.

CERN has a unique set of experimental areas that can provide a large variety of par-

ticle beams for such R&D projects and fixed target experiments. There are currently two complexes of beam lines at CERN, which supply beams for the East Area and North Area.

6.1 East Experimental Area

East Area makes use of the beams extracted from the PS. It contains four beam lines: T8, T9, T10 and T11. The latter three are extracted from common primary North (N) target and are therefore highly correlated in momentum and production angle. The experimental area of T11 can supply up to 3.6 GeV beam and currently houses the CLOUD experiment, T10 provides up to 7 GeV beam for the ALICE experiment test beam activities, T9 provides up to 15 GeV beam to various users (ATLAS, CMS, etc.). The T8 line is independent from those listed above, it receives a 24 GeV beam from the PS and houses a new irradiation facility, which combines a proton irradiation facility (IRRAD) with a mixed field facility (CHARM)[45].

This is the modern state of the area, which went through an extensive upgrade during the first Long Shutdown (LS1) of the LHC in 2012-2014. The former state of the facility, less flexible, was nevertheless extremely usefull for the irradiation studies of the materials and equipment used for the upgrade of the CMS experiment in LS1.

6.2 North Experimental Area

The North Area beam lines, which are most frequently used by the CMS experiment, are described in more detail below. The North Experimental Area was constructed at the end of the 1970s to house the fixed target physics experiments for the SPS accelerator, which was built at that time. Therefore the beamlines there are extremely flexible in terms of particle type, energy, energy spread, beam profiles, etc.

As understanding the properties of test beams is essential to the success in R&D and the proper callibration of the new detectors, the formation of those beams is discussed in detail below.

6.2.1 Beam Preparation and Slow Extraction for the North Area

Proton beams intended for the North Area are accelerated on the same injection chain as the ones meant for the LHC, but the maximum energy of the proton beam is lower, 400 GeV, and the bunch train generation scheme is different. At the end of the CPS RF gymnastics, the bunch train is split into 420 bunches. The extraction to SPS is then done by means of Continuous Transfer (CT) extraction. The bumper magnets deflect the nominal closed orbit such that part of the beam is shaved off by a thin electrostatic septum every turn (Fig. **6.1**). The entire beam is extracted in five turns (Fig. **6.2**).

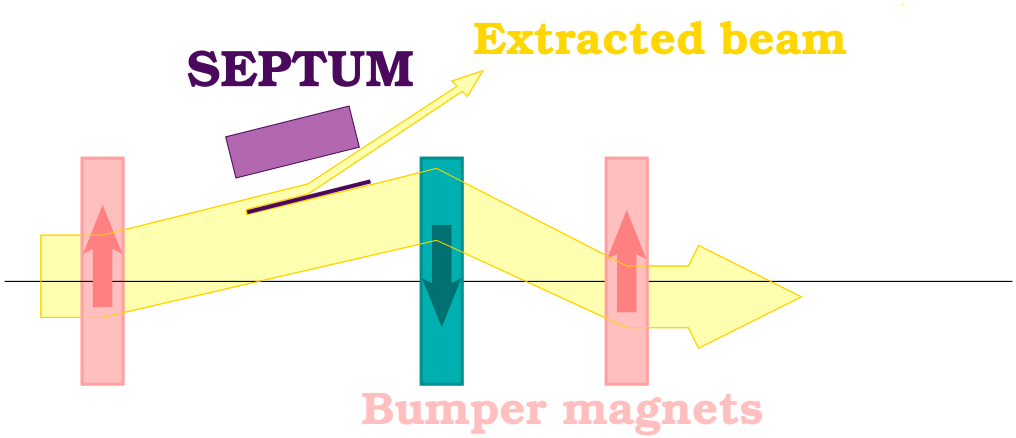

FIGURE 6.1: Slow extraction. For non-resonant Continuous Transfer extraction fast bumper magnets dump the beam to the septum, and the beam is fully extracted in several turns (CPS to SPS transfer for NA high intensity beams). In the case of resonant extraction the bumpers only serve to steer the beam close to the septum, the beam is then slowly driven into the septum by increasing betatron oscillations of the particles in resonance and is extracted in many thousands of turns (SPS slow resonant extraction toward NA).

The SPS is then filled with two five-turn CPS batches at the beginning of the supercycle, which yields 4200 bunches trapped at the harmonic 4620. Once the beam is accelerated, it is debunched before extraction (RF system is turned off), as this way not only a more continious beam can be achieved, but the extraction without interference with the RF system is technically simpler.

The extraction toward the North Area goes through a dedicated extraction line (see Fig. **3.1**) and is based on a different concept. When the SPS beam is due to be injected

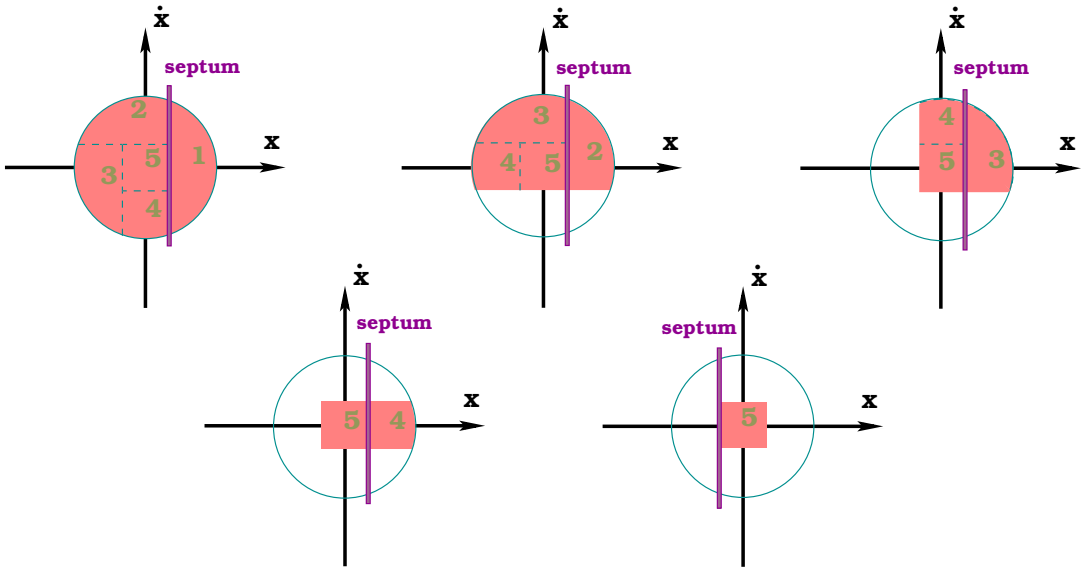

FIGURE 6.2: Continuous Transfer extraction principle. The septum magnet is shaving off a fraction of the beam with every turn. Before the last turn the bumper magnets steer the closed orbit even deeper into the septum. The entire beam is extracted in five turns.

into the LHC, the entire bunch train is extracted from the SPS by means of fast single-turn extraction: the extraction kicker magnets are rapidly ramped up, which deflects the entire beam into the septum, and further into the transfer tunnels. However this approach makes no sense for beams meant for fixed target setups: it would imply that the experimental area is exposed to beams of tremendous intensity within a fraction of the microsecond followed by a long no-beam period. This is usually inconvenient: not only the standard data acquisition systems are incapable to take advantage of such pattern, but this mode of operation is also frequently at variance with the physics goals of the final beam user.

Therefore the concept of slow resonant extraction is made use of [46]. In a linear machine the particles follow closed circular orbits in the phase space (Fig. **6.3**). However, if sextupole magnets are introduced, the phase space is perturbed: closed trajectories of the stable motion are delimited by the separatrices, which form a triangle. The area of the triangle is controlled by the betatron tune, which is set close to the third fractional resonance. By following along the separatrix, the particles with high amplitude of betatron oscillations eventually get to the ”corner” of the triangle – a fixed, unstable, point – and

then contunue to stream out along the outgoing arm of the separatrix.

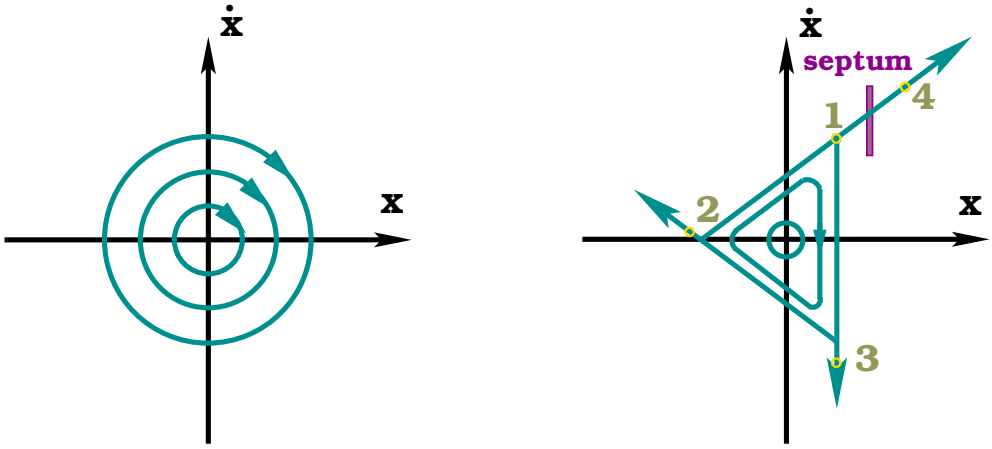

FIGURE 6.3: Slow extraction principle. **LEFT:** Phase space in a linear machine. **RIGHT:** Phase space in a machine with sextupoles. Once the particle reaches the corner of the triangle (**1**), it leaves the stable motion region and with each subsequent revolution in the synchrotron drifts further and further along the separatrix (**2, 3**), until finally it is far enough to be picked up by the extraction septum magnet (**4**).

As those particles deflect enough from the ”triangle”, they are picked up by a thin septum magnet, which gives them a kick toward the transfer line (Fig. **6.1**). In the SPS in general a particle spends about $2-3$ milliseconds in resonance before it reaches the septum. To extract not only particles with big betatron amplitude, but also the ones with small ones, the betatron tune is moved closer to the resonance, which leads to the shrinking of the stable motion triangle. Hence more particles resonate and eventually get extracted. By controlling the pace of approaching the resonance, the speed of the extraction is controlled. Such multiturn extraction can be spread in the SPS over several 100000 turns, the spill delivered to the fixed target experimental areas hence lasts for several seconds.

6.2.2 Beam Transfer and Primary Targets

Even the intensity of slowly extracted SPS beams is very high. Therefore several beam users can split the beam for multiple simultaneous tests: the beam passes through two splitter septum magnets (Fig. **6.4**, left). As thin electrostatic septa are not strong enough

to provide the desired level of beam separation, the thicker steel septa are used leading to significant beam losses in the barrier between the region with magnetic field and field-free cavity. Hence splitters are among the hottest objects in the accelerator complex. Splitting of the intensity between the beams is tuned by positioning of the beam relative to the septa's barriers.

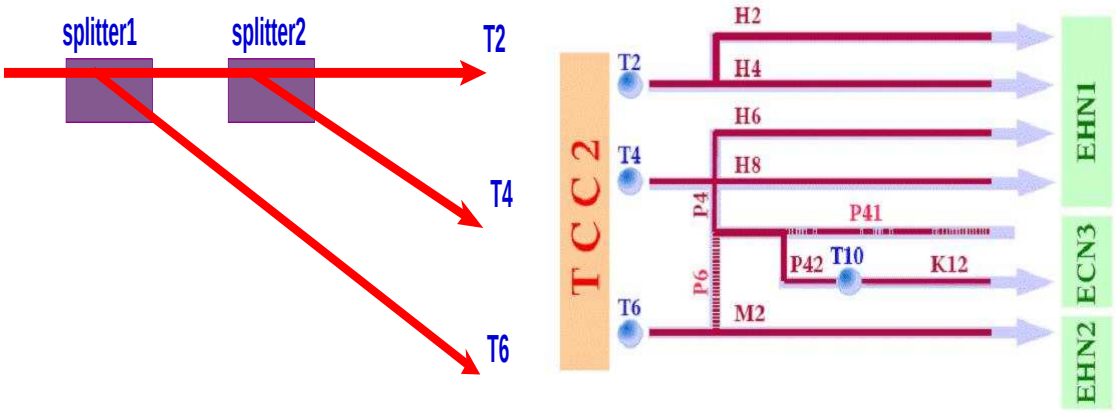

FIGURE 6.4: Beam splitting in the North Area. **LEFT:** Splitting by splitter septum magnets before the primary targets. **RIGHT:** Final separation of the beam lines by the wobbling stations.

Finally the beams hit the primary targets – T2, T4 or T6, each enclosed in the target station: a common support with a set of berrylium and lead targets of different lengths and cross-sections can be moved by the operator to select the target and adjust its position in the beam. Along with several Secondary Emission Monitors (SEMs) a target-carrier assembly is enclosed in the massive iron shielding (Fig. **6.5**).

SEMs upstream from the target box and in the target box assembly, upstream and downstream of the target, are used to monitor various characteristics of the beams. The BSI monitor is a single Ti conversion foil used to measure the intensity of the beam. As this monitor is located upstream from the target, its readings only characterize the beam and do not imply that it hits the target in the case of misalignment. Two monitors upstream and downstream from the target (Al-foil BSI monitors, parts of TBIU and TBID systems) provide the particle flux measurement for the calculation of a measure of the secondary particle production efficiency – target multiplicity.

FIGURE 6.5: **LEFT:** Primary targets T2 and T4. Along with a set of targets, the station contains beam monitors for positioning of the beam on the target, intensity measurements etc. **RIGHT:** Split-foil beam monitors: two sets of top-bottom and left-right imbalance monitors provide the data for target centering.

Another important parameter is the symmetry of the target. It is defined as follows. For each direction (top-bottom, left-right) two sets of the split-foil detectors are installed in front of the target (Fig. **6.5**), one set inside of the target box assembly and one somewhat 30 m upstream from the target. As the beam hits the foil, the flux measure is available for left and right (or top and bottom) foil converters. The values $S = \sqrt{1 - \frac{|R-L|}{R+L}}$ then defines the symmetry of the beam on that monitor. The SEMs upstream from the target box can be moved in and out of the beam. If this monitor is in the beam and the symmetry it measures is good, then the overall symmerty of the target is defined as follows:

$$S_T = 100 * S_1^{Horizontal} S_2^{Horizontal} S_1^{Vertical} S_2^{Vertical},$$

where 1 and 2 refer to the first and second sets of split-foil monitors, and a letter ”a” follows the value of symmetry to indicate that the angle is also taken into account. If for some reason the upstream monitor information is unavailable, the symmetry is calculated with a simplified formula:

$$S_T = 100 * S^{Horizontal} S^{Vertical},$$

and the letter ”a” does not accompany the value. As each of the individual monitor symmetries cannot exceed 1, which is achieved when the beam is equally distributed between the two halves of the monitor, the overall value of S_T cannot exceed 100. Only the symmetry measurement with two sets of monitors is trustworthy, even if the symmetry is high for the location of the second set of SEMs, it does not guarantee good angular steering on the target and, as consequence, good properties of the secondary beam. It is recommended to achieve at least a value of 75 for the S_T with ”a” for satisfactory operation.

6.2.3 SPS page-1

These important parameters are always shown on the SPS page-1 – an SPS summary page (Fig. **6.6**), which is normally shown in the control rooms, experimental baracks and also available online. Note that the SPS page-1 shows that multiplicity and symmetry for target T10 are equal to zero. This is due to the fact that this secondary target is not equipped with a downstream monitoring station, which is essential for such measurements.

Along with the above described parameters of the beams in the North Area, the SPS page- 1 provides information about the performance of the SPS itself and the phases of operation. There are two curves on the SPS page-1. The white curve reflects the magnet cycle, the other one in yellow and turquoise (or sometimes purple) represents the instantaneous beam intensity in the SPS. Two different colors for different parts of this curve are due to two different Beam Current Transformers (BCT) used for the measurement of the beam intensity: for high intensity beams measured with BCT3 the yellow color is used, for the low intensity beams measured by means of BCT4 the turquoise (or purple) color is used. Yellow and turquoise hence represent not only measurements done by different detectors, but also correspond to different scales.

The correspondence between the phases of the acceleration cycle and parts of the graph is as follows: flat bottom on magnet cycle curve, several steps of the intensity curve – beam injection from the CPS; linear rise of the magnet cycle graph, fixed plato on the intensity plot – acceleration (magnets are ramped up); flat top on the magnet cycle graph with linearly decreasing intensity plot – slow extraction toward the North Area; immediate

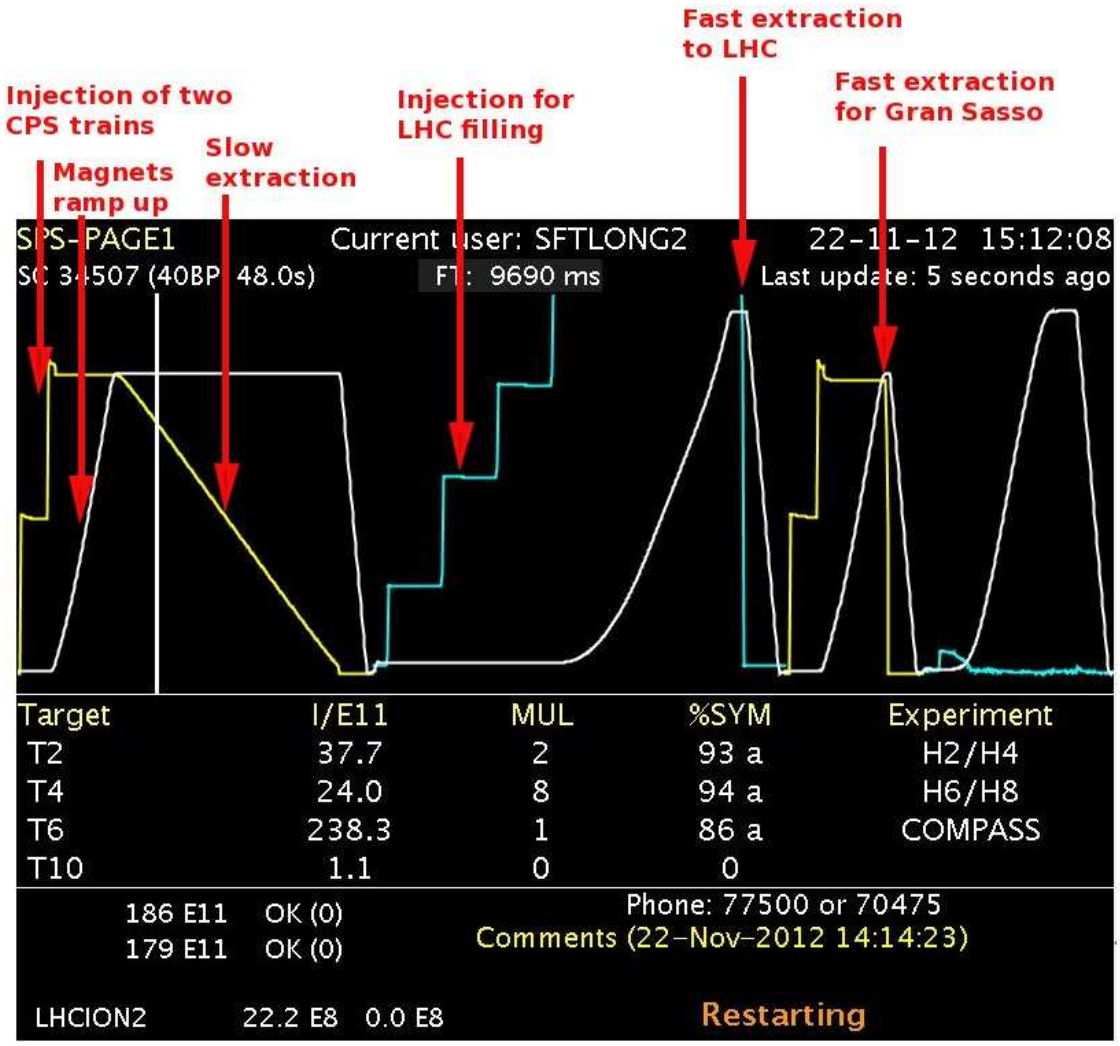

FIGURE 6.6: SPS page-1. Magnetic cycle curve (white) and instantaneous intencity in the machince curve (turquoise) and beamlines and primary targets information.

step down to the base level in the intensity curve – fast extraction of the beam (to LHC or for Gran Sasso); linear fall of the magnet cycle curve with the intensity curve staying low at the base level – ramping down of the magnets in preparation for the new acceleration cycle. The moving vertical line indicates the current phase of the cycle. The top left corner of the SPS page-1 shows the number of the super cycle after the abbreviation SC (this number gets reset to zero after every 65000), the number of basic periods and the total duration of the supercycle (the products of the number of basic periods and the duration of the basic period, 1.2 sec).

6.2.4 Multipurpose Wobbling Station

Several beams can be simultaneously delivered by the same target by means of the "wobbling station" – an arrangement of three dipole magnets, two upstream and one downstream from the target, followed by the special thick dump-collimators, called TAXes. An example for the beam lines H2 and H4, originating from the target T2, is shown in Fig. **6.7**.

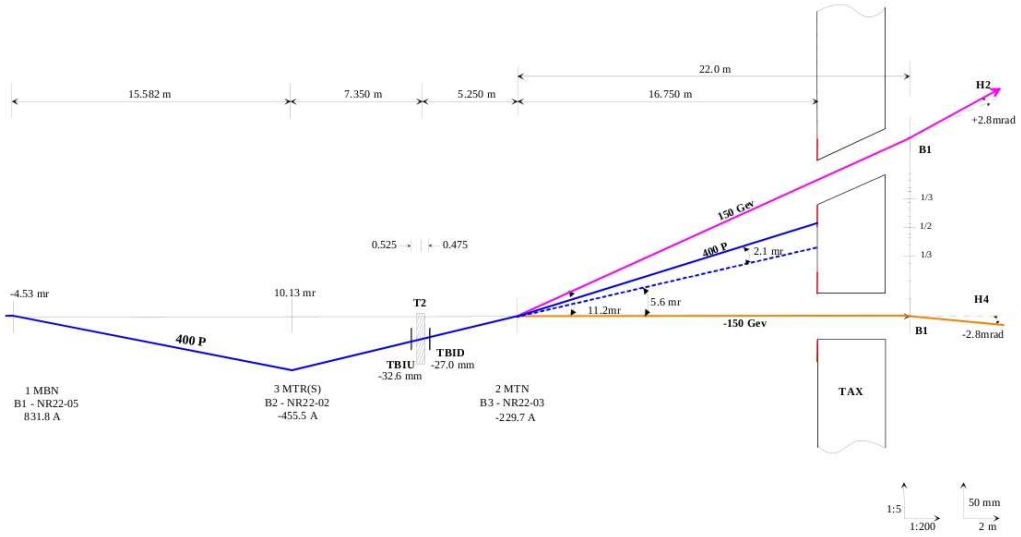

FIGURE 6.7: T2 wobbling station. Dipole magnet B3T deflects particles of a chosen momenta into the holes of the TAX block. The incident angle of the primary beam on the target is controlled by the dipole magnets upstream from the target – B1T and B2T. The picture is from [47]

The magnet downstream from the target, B3T, is set to provide momentum separation and sweep the particles of desired momentum produced at zero production angle into the center of the TAX holes. However, the distance between the TAX holes of beam lines H2 and H4 is fixed, therefore the required separation of the beams often implies non-zero angle of incidence on the target. This is achieved by the steering of the beam with the magnets B1T and B2T upstream from the target. The attenuated primary proton beam hits the TAX block between the holes and gets dumped. However, this is not the only option – in the case of the primary target T4 the attenuated proton beam is picked up by the beam line P0 and transmitted to the target T10. In some cases the primary proton beam can also be deflected by B3T into one of the other beam lines; however due to radiation issues this can only be

safely done for highly attenuated proton beams. Primary target T6 has no wobbling station, the momentum ratio between the P61 and M2 lines is fixed at 2.0 (400 GeV/c primary beam in P61 implies -200 GeV/c momentum in M2.

Hence the currents in the three dipole magnets B1T, B2T, B3T essentially determine the state of the wobbling station and the secondary hadrons beam momenta that the wobbling is optimized for. To provide more flexibility in momentum selection to the final user of the beam, the adjustable holes in the TAX blocks possess significant aperture (Fig. **6.8**) to select a wide secondary hadron momentum bite[1]. The particles which are not deflected into the apertures, hit the TAX blocks and are properly dumped. The wobbling station is therefore a radiation hot area; it is hidden underground to ensure sufficient shielding.

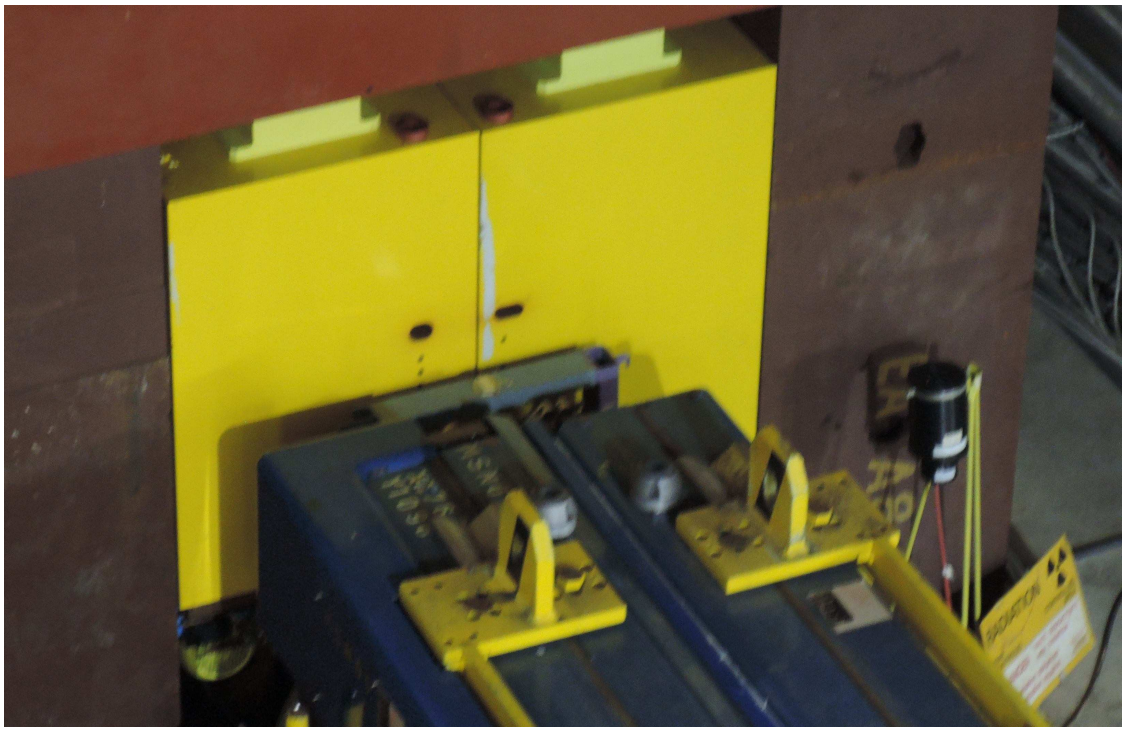

FIGURE 6.8: TAX blocks of the beam lines H2 (right) and H4 (left). The movable TAX blocks provide a selection of collimators and serve as a first stage of the secondary beam momentum selection.

[1]For example, when the wobbling station of T2 is set to multipurpose wobbling, with 150 GeV/c positively charged hadrons for H2 and 150 GeV/c negatively charged hadrons for H4, both beam lines can be supplied with particles with a momentum in the range of 100-360 GeV/c, however only 150 GeV/c particles follow the zero production angle line.

6.2.5 Beam line Equipment

The layout of the H2 beam line is available at [48]. It documents the positions of all the beam line elements starting from the primary target T2. More than 400 m of the beam line downstream from the target are hidden underground or protected by concrete blocks for shielding purposes.

Part of the beam is enclosed in vacuum pipes to minimize the losses due to the interactions with molecules of air. However, in the case of the short term installations and for ease of maintenance of various beam monitoring equipment, the beam frequently leaves the vacuum tubes through thin windows and travels through normal air. Technical up to date listings of the beam line elements can be found at [49], in particular, those listings include records of the vacuum beam pipe sections.

All the outfit of the beam line is remotely controlled from the main experiment control room by means of CESAR (Cern Ea SoftwAre Renovation)[50] graphical user interface (Fig. **6.9**). CESAR is a client-server control system based on Java and constructed around an ORACLE database. Below, as the equipment of the beam line is described, their aliases used by CESAR are given in capital letters.

The momentum selection is done downstream from the TAX blocks by the first dipole magnets of the beam lines (Fig. **6.10**). Dipole magnets of the beam lines, called BENDs, are six meter long warm magnets with peak field of about two Tesla. Further BENDs are used for steering the beam from the underground area to the experimental zone. Therefore their currents normally should not be modified by the users.

In case the beam is not wanted in the experimental zone, powering down the first BEND leads to complete dumping, and the beam does not even enter the experimental hall.

TRIMs are small, 40 cm long warm dipole magnets, which serve for small corrections in the beam steering (Fig. **6.11**). Hence the current in the TRIMs should normally be set to zero and only the last pair (for vertical and horizontal fine steering) of TRIMs before the experiment is to be used. Those magnets are quite weak – typical values of a 100 GeV/c beam displacement by the TRIM7 and TRIM8 with 100 A current is 22 mm.

Quadrupole magnets, called QUADs (Fig. **6.12**), are used to focus or defocus the beam

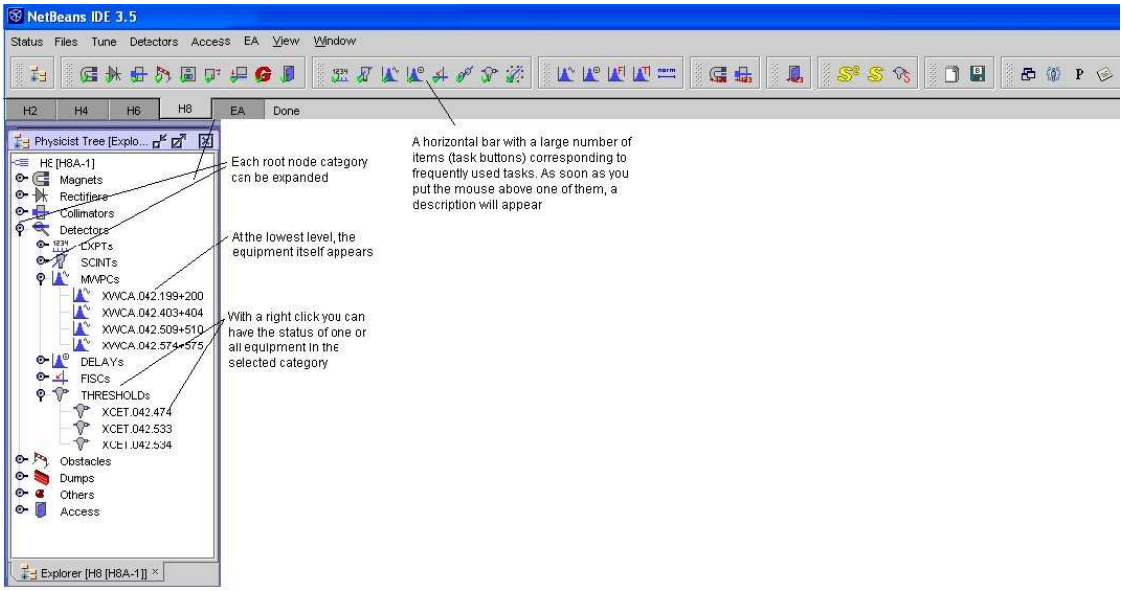

FIGURE 6.9: CESAR graphical interface for controlling the North Area beam lines by the beam user. This interface is automatically invoked on all of the front-end computers in the control rooms of the North Area.

FIGURE 6.10: BEND1 and BEND11 in H2 and BEND1 in H4 beam lines in the underground shielded area. The first dipole magnets in the beam lines provide the momentum selection of the secondary beams.

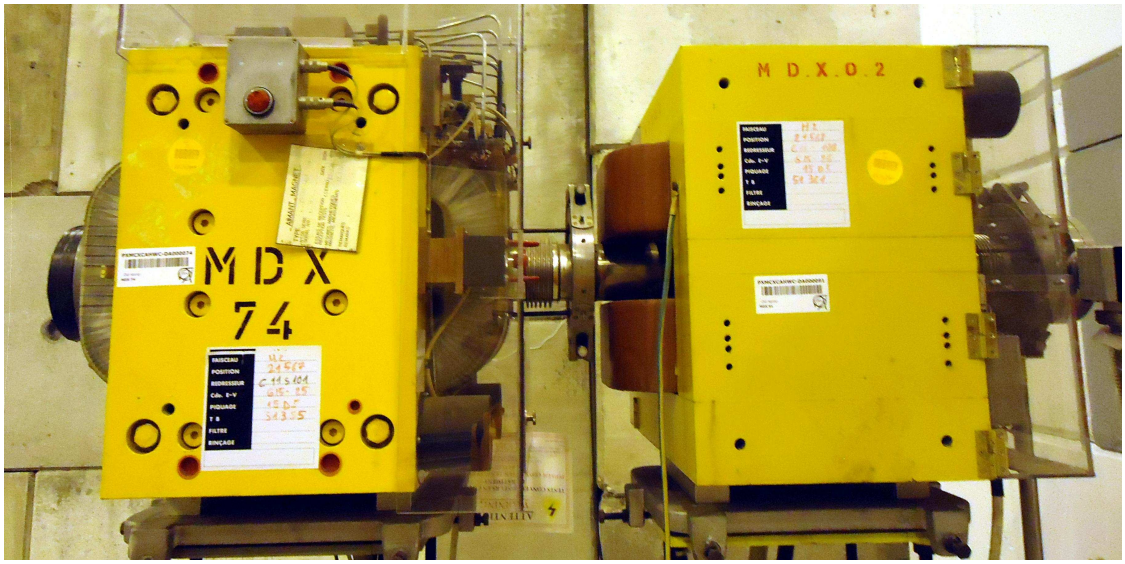

FIGURE 6.11: TRIM7 (left) and TRIM8 (right) in H2 beam line serve for fine beam steering in vertical (TRIM7) and horizontal (TRIM8) directions. Note that they are installed around the short vacuum beam pipe; before and after this vacuum section the beam travels through the air.

and hence to change the beam spot size. Normally the first QUADs of a beam line serve to refocus particles produced in the primary target before the momentum defining slit. Intermediate QUADs help to eliminate any reminant correlations between position and momentum of the beam particles after the final bending magnet. The last QUADs before the experiment are set up to minimize the beam spot.

This however isn't the only possibility. Most of the beam tests of the hadron calorimetry do not require a focused beam, as even a highly defocused hadron beam spot is still smaller than a single independently read-out calorimeter cell (for more details see the section on the CMS Hadron Calorimeter). Some equipment benefit from the beam intensity spread homogenously over a sufficient area during the beam tests. In the course of the test beam in the fall of 2012 the author has created a set of beam configurations with a diagonal beam spot of $1\,cm \times 4\,cm$ of the required intensity for the Silicon Beam Telescope team; such extraordinary beam profiles cannot be realized by means of few pieces of beam line equipment and imply extensive use of the entire beam line.

The collimators in the beam line, called COLLs (Fig. **6.13**), are essentially adjustable

FIGURE 6.12: One of the Quadrupole magnets in the H2 beam line. Most frequently used for focusing of the beam on the main experiment, if needed, they can also be used to create quite sophisticated beam profiles.

motorized slits. Depending on their position along the beam line, their function can be of a distinct nature. If used after the bending magnet, they can be a part of a momentum bite defining spectrometer. In other cases they can define the acceptance of the beam hence affecting the size of the beam spot in the main experimental area. In both cases the collimators affect the intensity of the beam, as the particle flux is proportional to the slit opening.

Besides the beam shaping and steering equipment, the beam lines are also outfit with various beam monitoring tools, which help to establish various characteristics of the beam.

The scintillators, called SCINT, are tiles of scintillating plastic coupled to large PMTs with a fishtail light guide (Fig. **6.14**, top left). They are used to monitor the beam intensity

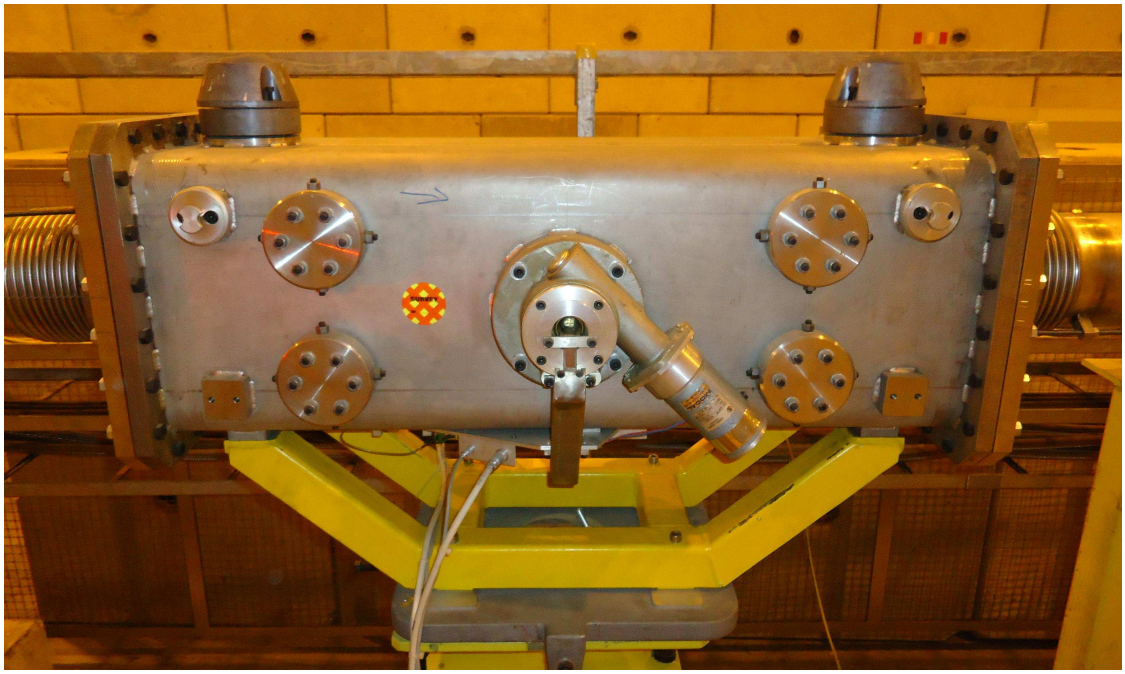

FIGURE 6.13: Collimator COLL14 in H2 beam line. As collimators redefine the acceptance of the beam, they are among the hottest objects in the beam line. This particular collimator is the only one in the beam line which is not hidden under protective concrete shielding.

or to strobe more complicated equipment. The scintillators provide the integrated count per spill. As those counters present a significant amount of the material to the beam, the scintillators are motorized and can be removed from the beam, once their task has been accomplished, to minimize the multiple Coulomb scattering and Bremsstrahlung.

The multiwire proportional chambers, MWPCs (Fig. **6.14**, top left), have an analog readout that integrates charge for every wire over the whole spill. Since the total charge on a wire is proportional to the number of particles on it, the plot of charge vs. wire position gives a beam profile in the direction normal to the direction of the wires. The wire spacing in the MWPCs used in the H2 beam line is 1 mm, but the number of readout channels is limited to 32, therefore the cabling has been made such that either each wire or only every second or third wire can be read out. Depending on the beam characteristics, different arrangements can be used. Hence, if every wire is used, only the central one third of the chamber is read out. The sensitivity of the MWPSs strongly depend on the high voltage applied (the maximum HV for MWPC operation is 4000 V). For low intensity beams higher

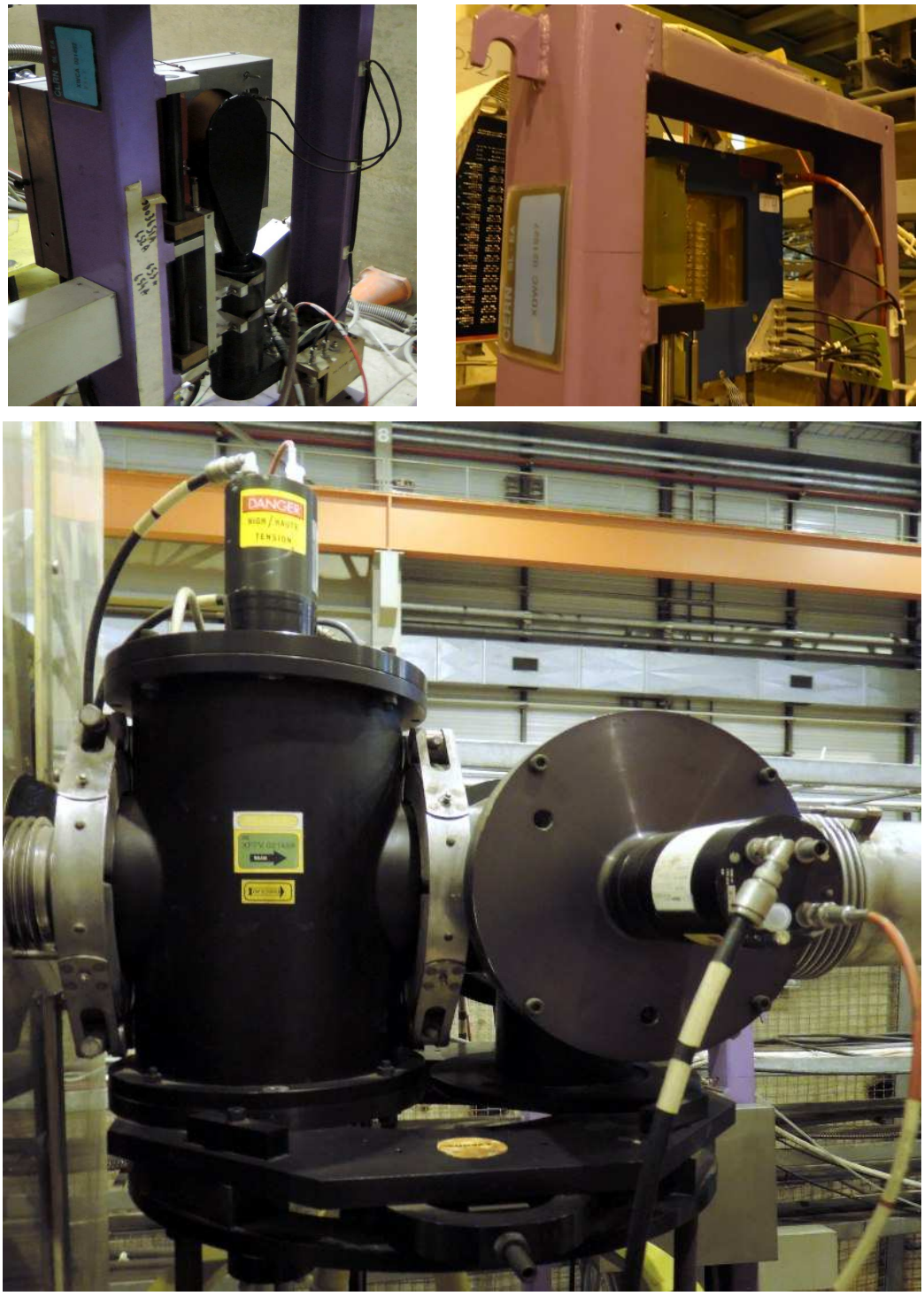

FIGURE 6.14: Beam instrumentation in H2. **TOP LEFT:** Multiwire proportional chamber and a scinntillator counter sharing the same motor. **TOP RIGHT:** Delay wire proportional chamber. **BOTTOM:** Filament scanners.

HV is required to produce a large signal-to-noise ratio. As the highly collimated high intensity beams require much lower HV to avoid saturation, the HV is automatically reduced if the signal ecxeeds 1024 counts.

As the MWPCs often share the motor with the scintillator counter, special attention is required when the later is moved out of the beam.

The delay wire chambers, XDWCs (Fig. **6.14**, top right), provide higher resolution beam profiles and are more sensitive than MWPCs. As in any other multiwire proportional chambers, particles passing through the XDWCs ionize the gas and create free electrons and ions. The high voltage between anode and cathodes then accelerates the electrons towards the 20 micron anode wires, where they start a multiplying avalanche. At the same time an image current is induced in the cathode wires closest to where the anode avalanche takes place. The XDWCs are composed of a sandwich of two cathode planes surrounding a central plane carrying anode wires. The pecularity of the XDWC is that the position data is taken not from the anode wires, but from the cathode, where individual wires are connected to a tapped delay line. The induced signal from the cathode wires builds up two waves in the delay line, one in each direction. These travelling waves are the integral of the contribution from the different cathode wires, summarized according to the delay per tap of the delay line. The anode signal is used as the common start. Then the time delays for the integrated waves to reach the amplifiers at the ends of the delay line are measured. This determines the position of the hit, where ionization took place, with a resolution about ten times better than the spacing of wires in the XDWC. The second cathode-anode-cathode sandwich, providing the measurement in the other plane, is located in the same chamber. These drift chambers with a simple time-to-digital converter over a delay line register the individual tracks with a resolution better than 200 micron. The beamline control software has access only to the beam profiles accumulated over the spill, but the output signals of the delay wire chambers can be used by the DAQ of the experiment, using private time-to-digital converters.

The filament scanners, FISCs (Fig. **6.14**, bottom), consist of motorized scintillator filaments, 200 microns wide and 4 mm thick along the beam direction, and a pair of photomultiplier tubes for detecting the light produced by charged particles in the scintillator. This

kind of detector is integrated into the vacuum system. The filament can be moved through the beam step by step to measure the beam profile. The measurement can be done in a slow mode, when the filament moves one step per spill, or in a fast mode, when the entire profile is measured in one spill. The slow mode of operation provides a precise profile measurement, but requires long time, as only one point is measured during the spill. The fast mode is less precise as it relies on a stable flux of particles during the entire spill. Besides the result of the fast scan is conclusive only in case of intense beams: while getting a decent beam profile in the case of a slow scan requires a beam intensity higher than 1000 particles per spill, and for the fast scan it should be higher than 10000 particles per spill.

6.2.6 Control of the Particle Type in the Beam

Usually each user of a beam line is interested in particular sets of beam energies, beam intensities as well as a beam profile at the main experimental zone. These sets of corresponding magnet currents and collimator apertures are summarized in so called "Beam Files". The files are usually prepared in advance by the senior beam physicist according to the user's request. They are then used by the CESAR application for initial beam set up.

The type of particles in the beam is however the full responsibility of the final user of the beam, as the settings of equipment responsible for it are not stored in the Beam Files.

The secondary particles produced in the target region form beams of mixed composition, which depends on the momentum and production angle. The conposition of the hadronic part of the beam can be calculated with the PARTPROD program[51]. The beam is the mixture of different types of hadrons (p, K, π), muons and a small electron component.

The beam lines are equipped with an absorber, a lead plate $3 - 10$ mm thick, located somewhere half way along the beam line. Once moved into the beam, it removes the electron component, as the electrons loose a substantial part of their energy by Bremsstrahlung and are not transported further along the beam line. At the same time, the absorber almost does not affect the hadronic component of the beam.

To get a pure electron beam, one has to use a converter, a lead plate several millimeters

thick, which is located right after the TAX block upstream from the BEND1. Once the converter is moved into the beam, the photons, contained in the neutral component of the secondary beam, are converted into electron-positron pairs, which can be momentum selected and delivered to the main experiment.

The muons are produced by the decay of pions. Therefore to get a muon beam, one needs to set up a beam line for a pion beam, then prevent the pions which haven't decayed from reaching the experiment. This can be done in two ways. The first option is by moving into the beam a dump block, XTDV, which is located right upstream from the H2A experimental zone, used by CMS, or closing in an off-center position one of the collimators downstream from the last bending magnet. In this case the muons are not momentum selected, and the spread of the muon momenta in the beam is between 57% and 100% of the pion momentum. The second option is to close the collimator upstream from the last bending magnet. In this case muons are momentum selected.

Setting the converters, absorbers and dumps to the appropriate position to achieve the desired composition of the beam remains the responsibility of the beam user and is not stored in the Beam Files.

6.2.7 Beam File Creation from Scratch

Although a certain set of the "Beam Files" exists for the users of the beam and is stored in the CESAR application, sometimes there is a need to create new ones. As the beams in the H2 and H4 experimental areas arise from the same primary target, T2, they are highly correlated both in energy of the secondary beams and production angles and hence the settings of the wobbling station T2 are sometimes changed to accomodate the needs of H2 and H4 users at the same time. The settings of the wobbling station can also be changed in the case where some piece of equipment in the upstream region is out of order, provided the operation still can be managed without it with different settings of the wobbling station. As a sufficient part of the beamline is a radiation hot area, immediate repairs are not always possible.

The settings of the wobbling station can more or less be described by the currents

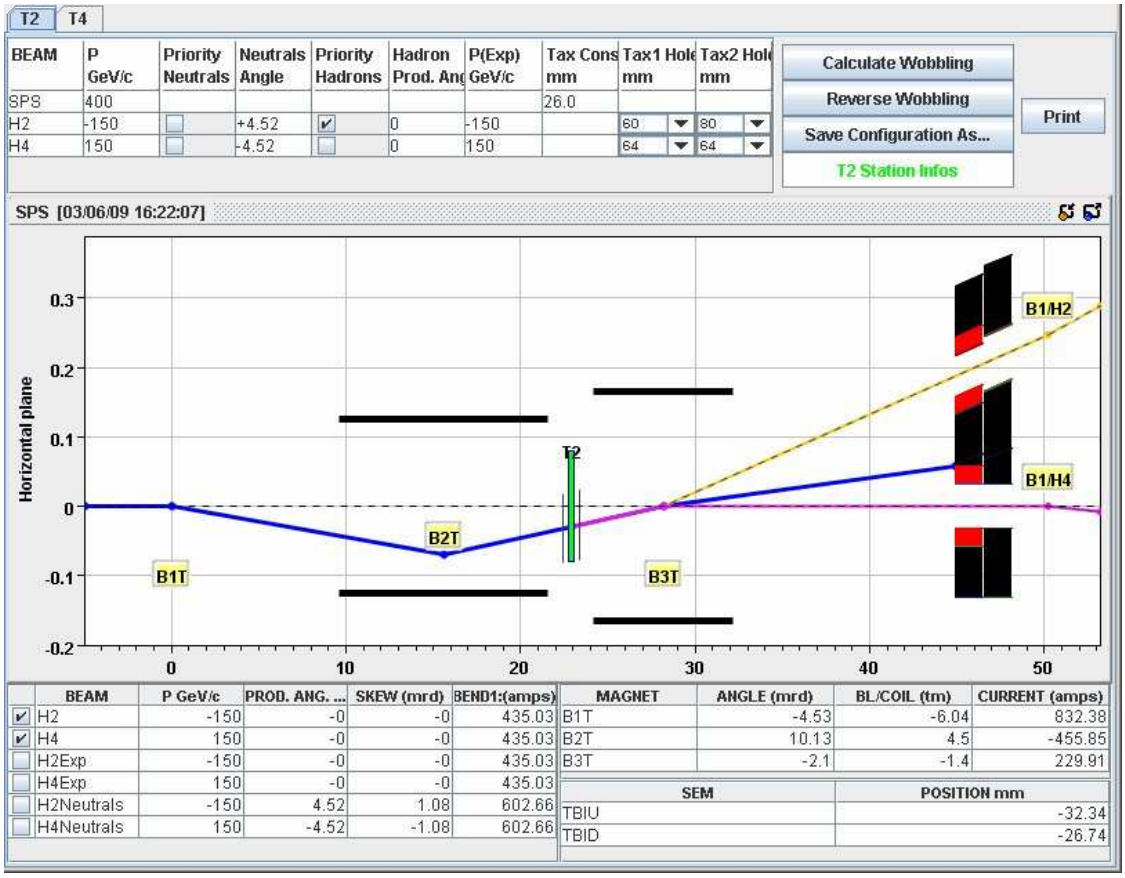

FIGURE 6.15: The appearance of the Wobbling Calculator standalone tool. The chart at the top allows one to set the parameters of the secondary beam and TAX blocks apertures. The right-hand side chart below the drawing summarizes the settings of the wobbling station: currents in the magnets and positions of the Secondary Emission Monitors. The left-hand side chart summarizes the secondary beams' parameters along with the current in the first bending magnet of the beam line required to properly steer the particles with selected momentum.

in three main magnets, B1T, B2T, B3T. The sets of those currents which are commonly used and well studied, are grouped into the wobbling beam files. One can find the list of those settings in the CESAR standalone program [52]. Only the senior beam physicists are in charge of changing the "wobbling" settings, in most cases such changes also require retuning of the SPS beam by the SPS operator. The wobbling settings are agreed on a weekly meetings and posted on the corresponding beam line's whiteboards[53].

The final users of the beam can play around with a "wobbling calculator"[54] standalone to estimate the parameters of the wobbling station, which would suit their needs

(Fig. **6.15**). The values of secondary beam momenta for particles with zero production angle at all beam lines originating from the same target should be specified in the column "P(Exp)", after clicking the "calculate wobbling" button. The program calculates the values of currents in the magnets of the wobbling station and draws the corresponding beams.

The same standalone program can be used to create the beam files in a critical situation, when they haven't been provided by the senior beam physicist, but the beam time cannot be spared in waiting. In this scenario the following steps should be followed:

1. Once the settings of the wobbling station are known from the beamline whiteboard web page, they can be specified in the wobbling calculator in the right-hand side table below the drawing in the column "Current".

2. The momenta of the beams at zero production angle for all beamlines originating from the same target is normally also provided on the whiteboard[1] and should be specified in the "P(Exp)" column in the chart at the top of the wobbling calculator.

3. The appropriate size of the TAX blocks apertures should be set in the same chart.

4. The energy of the secondary beam for the appropriate beamline has to be specified in the column "P" in the top chart.

5. The calculation is initiated by clicking the "Reverse wobbling" button. After that, the drawing should updated to show the propagation of the beams through the wobbling station. The numbers in the left-hand side chart at the bottom of the calculator will also update. The information of primary importance in this case is the value of current in the first bending magnet in the beam line of interest, which can be found in a column "BEND1".

   At the same time the drawing provides a visual check that the selected beam safely reaches its beam line. If on the plot the beam hits one or both TAX blocks or a wall of the B3T magnet of the wobbling station, it means that the beam of the selected

[1] If these momenta are not provided, it is possible to find them by identifing the appropriate "wobbling file" in the wobbling manager, described above.

momentum got dumped and cannot be extracted in the specified way, even if the chart provides the value for the current in the first bending magnet of the beam line.

Figure **6.16** shows the example of a low energy, 20 GeV, beam, which hits the TAX blocks and gets dumped before reaching the beam line H2.

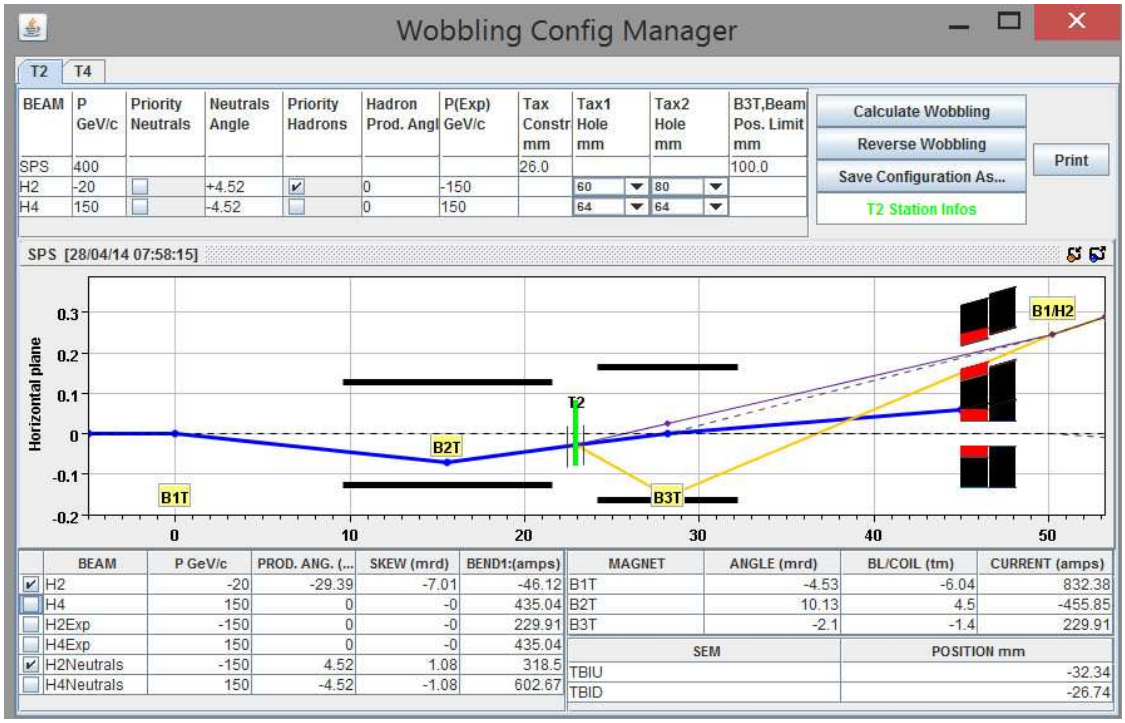

FIGURE 6.16: Wobbling calculator with Democratic multipurpose wobbling. Example of dumping of the beam of interest ($20\,GeV$) in the TAX blocks. This beam cannot be directed into the H2 beam line.

Figure **6.17** shows an example of a low energy beam which hits the wall of the B3T magnet of the wobbling station and gets dumped before reaching the beam line H2.

In both cases above the wobbling station is set to the so called "Democratic multipurpose wobbling", which is optimized to center in the TAX block apertures the following beams: both beam lines, H2 and H4, receive $150\,GeV/c$ hadrons: H2 – negatively charged, H4 – positively charged.

Such low energy beams cannot be picked up by the beam line H2 from the secondary particles produced in the primary target. However, as the neutral hadronic component of the beam, K^0 and Λ^0, decay in the air, the products of their decays, pions

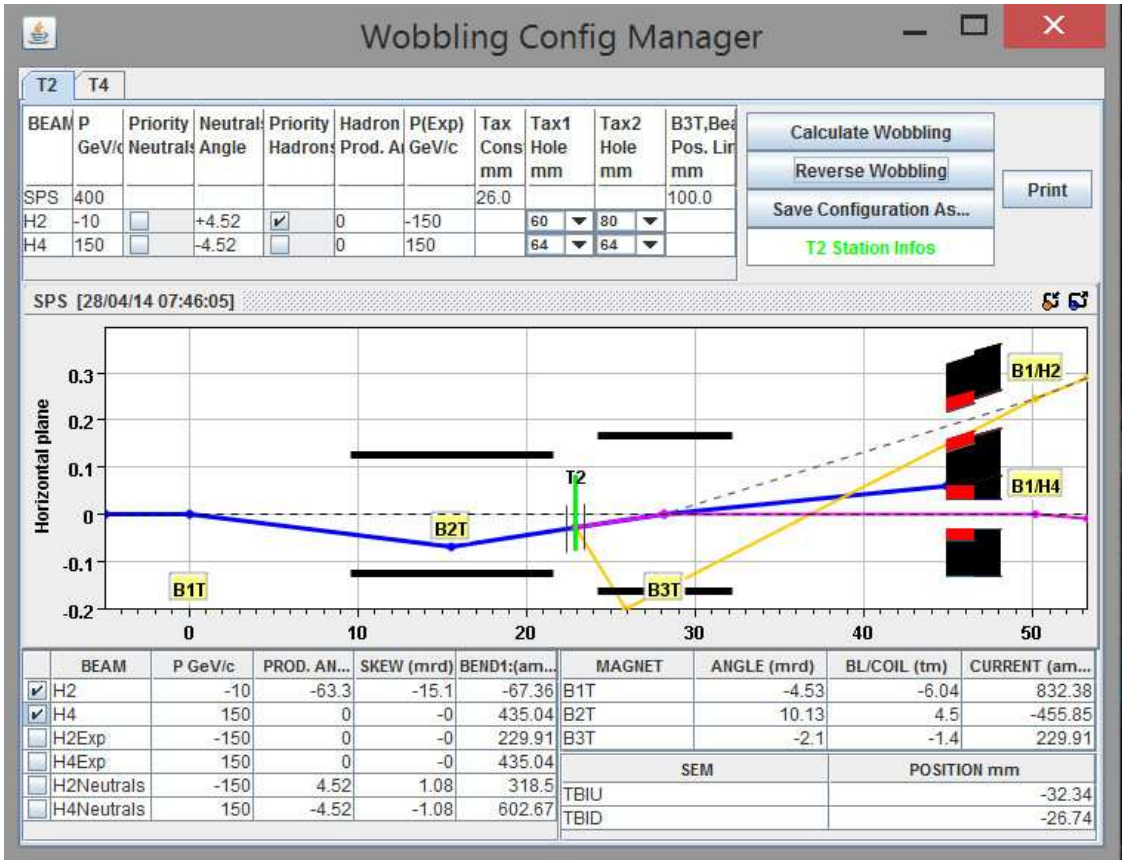

FIGURE 6.17: Wobbling calculator with Democratic multipurpose wobbling. Example of dumping of the beam of interest ($10\,GeV$) in the B3T magnet of the wobbling station. This beam cannot be directed into the H2 beam line.

and protons, can be picked up and momentum selected to obtain low-energy hadron beams.

6. It is possible to make the Beam File completely from scratch, advancing step by step in setting the beamline parameters and monitoring the beam with various beam instrumentation. However, this way is more time consuming than starting from some existing hadronic beam file as a template – it does not matter in this case if it corresponds to the same or a different wobbling. Therefore here the latter method is shown, while the first one obeys the same logic.

   Therefore it is suggested to open some hadronic beam file and create its copy with a different name ("Copy" option in CESAR). According to the naming convention for

the Beam Files, the name of the Beam File starts with the name of the Beam Line or experimental zone (i.e. H2A), followed by a unique number. There is also a field to provide extra information, which can be useful: number of the wobbling file[1], the energy of the beam, type of particles, and any extra information of high importance (tertiary beam[2], specific production angle, etc.)

7. The value of current in the first bending magnet of the beam line, obtained in the previous steps, is used as a starting point to create a Beam File. Once the template with a new name is ready for modifications, it has to replace the value for BEND1. As this setting determines the momentum of the particles in the secondary beam, it should not be changed when further fine-tunning of the beam is performed.

8. Check the profiles of the beam in a pair of wire chambers (for vertical and horizontal measurements) closest to the origin of the beam. A good profile is a Gaussian-like peak centered about the origin of the coordinate axis.

   If the beam is off-centered, it can be steered by the dipole magnets upstream from the chambers – the currents in the relevant magnets have to be ajdusted. Then with the next spill from the SPS beam profiles from the wire chambers will be updated. Adjustments of the current are usually intuitive, even though this take some practice, as they depend on both the type of magnet and momentum of the beam. It is possible however to get a feeling for it without spending beamtime by studying the Bending Power versus Current characteristic curves of the relevant magnet in a CESAR standalone BlAndCurrentConversion[55]. This utility allows one to choose a particular magnet in the beam line of interest and shows the plot of bending power as a function of current, as well as allows one to calculate the bending power for a particular point.

   The beam position has to be adjusted by means of the secondary bending magnets

[1] In the wobbling manager application the most common wobbling files are enumerated. For example, the Democratic Multipurpose wobblings have numbers 1 and 2.

[2] This is important information indeed: tertiary beams naturally have low flux compared to the secondary beams. Therefore, the Beam Files for tertiary beams have collimators widely opened to deliver more particles per spill. Beam Files for secondaries on the other hand, set the collimators to somewhat moderate apertures. Therefore, when the user switches from a tertiary to secondary beam, it is highly recommended to load the collimators (i.e. partially close the slits) before magnets.

(BEND2, BEND3 for the vertical deflection and BEND5, BEND6 for the horizontal). Those magnets are exptremely powerful, so even tiny changes of the current will result in significant deflection of the beam (for instance, a change of 1 Amp in BEND2 results in 15-40 mm deflection of the user's beam – depending on the energy of the secondary beam.

9. The distortion of the Gaussian shape of a profile, especially for the off-centered beams, can be due to partial dumping in the upstream equipment – collimators or even magnets. It is better to correct the position of the beam before taking any steps toward the profile shape correction.

10. The size of the beam spot (width of the profile) can be changed by adjusting currents in the quadrupole magnets upstream from the wire chambers. Those magnets affect the beam spot size by focusing the beam in one plane and defocusing it in the other one. In most cases the desired beam spot size can be obtained by changing the currents in the several downstream-most quadrupole magnets (QUAD16, QUAD17, QUAD18).

11. Since primary dipole magnets, BENDs, are located upstream, further adjustment of the beam spot position by means of downstream trimming magnets may be required. This final adjustment though has to be postponed until the quadruple magnets are finally set in that part of the beamline – as the beam is focused by the quadrupole magnet in one direction, it is naturally defocused in the other one. Therefore the off-centering of the beam profile which seemed insignificant before the beam got defocused, can turn out to be substantial after applying a correction to the quadrupole's current. Vice versa, the result of centerring the beam might not be worth the effort, if the subsequent correction of the quadrupole's current will sufficiently narrow the beam.

12. The flux of particles in the beam can be changed by adjusting the openning of the collimators. In every beam line there is a collimator, located in the dispersive focus, serving as a momentum slit. In the H2 beam line this is a COLL6. For those collima-

tors the beam flux is proportional to the opening, but at a cost of momentum spread, which also grows linearly with the opening. For the other collimators, the flux grows with the opening, but in a non-linear way.

13. If an electron beam is needed, first of all, a hadron Beam File has to be made, then the "Extrapolate" button has to be used, then the option to select is "Hadrons→Electrons". This procedure invokes a special algorithm which properly takes into account the energy losses due to synchrotron radiation.

Beam tuning steps might need to be repeated several times to get a satisfactory result, especially for the tertiary beams, which naturally possess a low flux. It might therefore be hard to even find them by means of the low-sensitivity equipment upstream.

It is also worth to remember the following tips:

- For the beam horizontal and vertical planes can be treated independently. However, the vertical plane is more important for steering the beam into the hall – as the beam originates from the underground hall, it significantly gains in altitude on its way to the final user.

- Analog wire chambers, located upstream, are less sensitive than the delay wire chambers, situated closer to the final user. Therefore there should be a sufficient beam flux to get conclusive measurements by means of analog wire chambers.

- The numbering of the elements of the same type does not always increase along the beam line, as some elements were installed later than the original beamline comissioning.

- Electrons loose a significant fraction of energy even in thin obstacles. Therefore all non-essential equipment has to be removed from the electron beam, once the fine-tuning is over.

An example of a properly setup electron beam is shown in Fig. **6.18**. As demonstrated by the beam profiles from the delay wire chambers, this beam is focused around the nominal beam axis and has nearly Gaussian shape with the core profile of about $4\,\mathrm{cm}\times 4\,\mathrm{cm}$, as requested by the users.

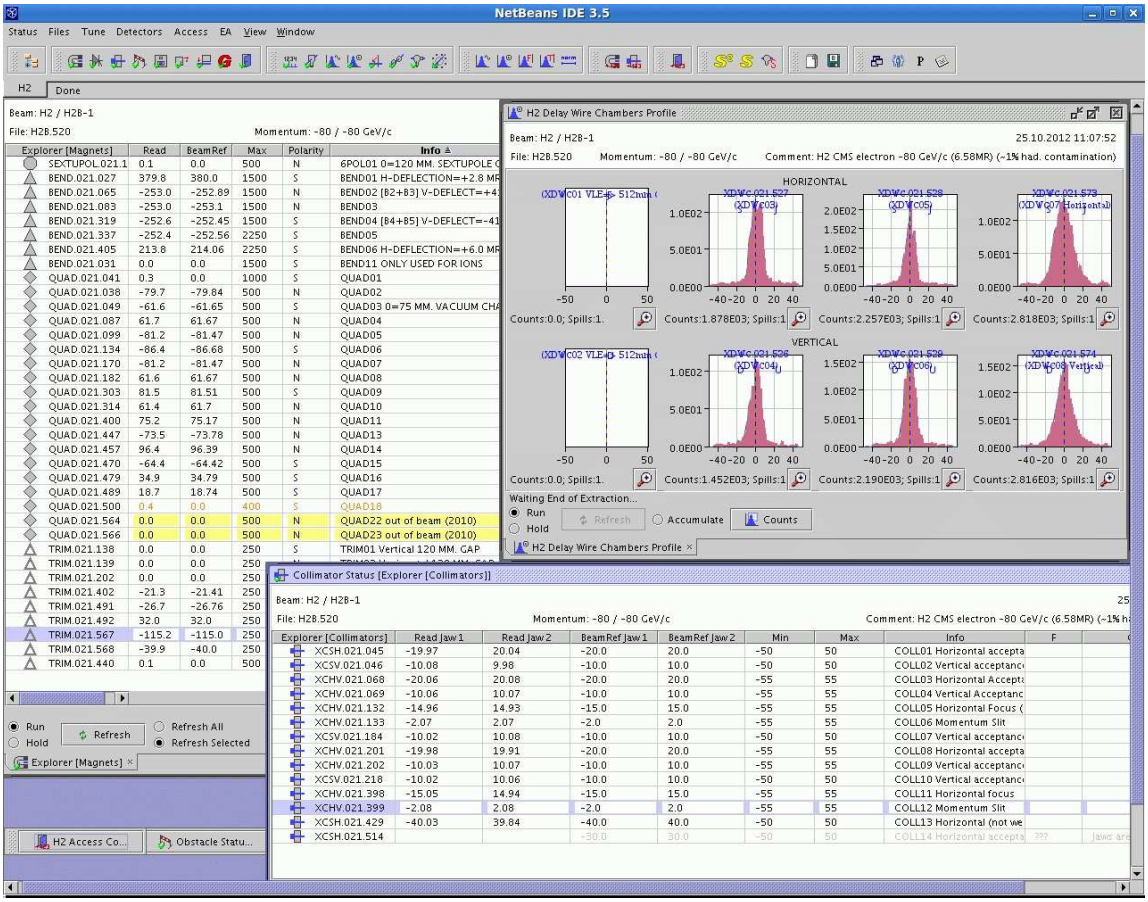

FIGURE 6.18: Example of a properly setup electron beam file for H2 beam line with the beam profiles from wire chambers (screenshot from CESAR).

Chapter 7

Crystal Fibers

Lutetium Aluminium Garnet (LuAG, $Lu_3Al_5O_{12}$) combines a high density of 6.73 g/cm^3 with relatively short radiation and interaction lengths: $X_0 = 1.41\,cm$ and $\lambda_I = 23.3\,cm$. Pure LuAG is an efficient Cherenkov radiator: with its high refractive index ranging from 2.14 for 190 nm to 1.848 for $520\,nm$, the Cherenkov threshold for electrons is as low as 97 keV. By doping the LuAG matrix with rare-earth ions, such as cerium, fast scintillation processes can also be activated. Cerium-doped crystals of LuAG ($Lu_3Al_5O_{12}$:Ce) exhibit bright scintillation in the green part of spectrum with a maximum at 520 nm (Fig. **7.1**).

The micropulling-down technology grows single crystals of LuAG directly into a fiber shape with a diameter of a few millimeters. Furthermore, rather high pulling rates along with the possibility to grow multiple crystals simultaneously provide the opportunity for large-scale production.

Recent advances in growing technology improved the optical properties of the crystals. As a result, the new generation of the LuAG fibers has attenuation lengths ranging from 30 to 50 cm.

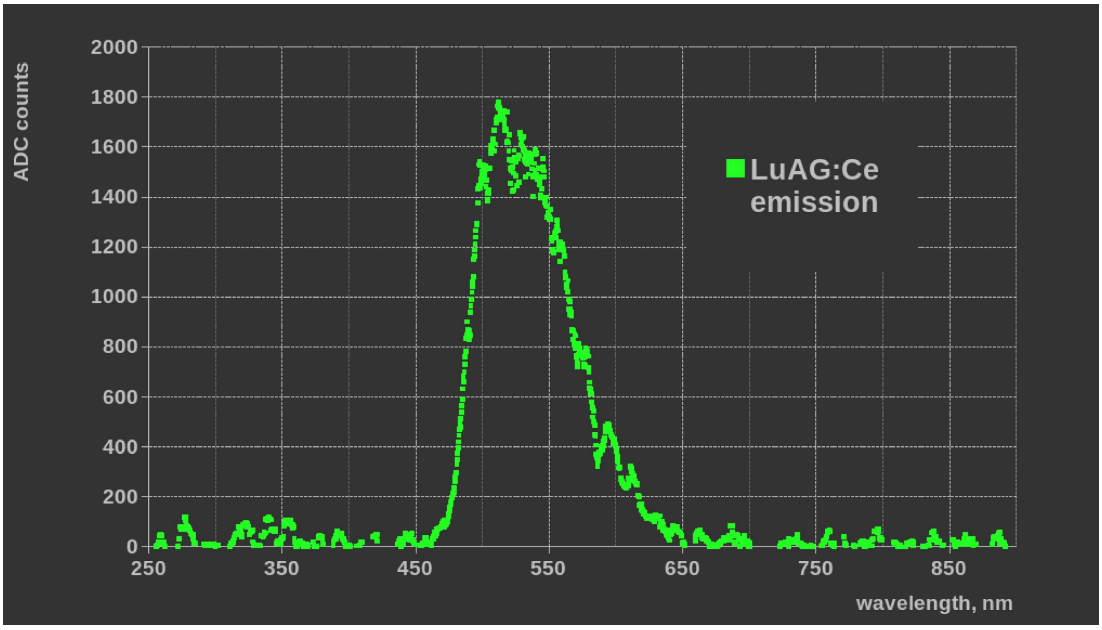

FIGURE 7.1: Emission spectrum of a scintillating Ce-doped $LuAG$ crystal.

All of the above offers a tempting possibility to exploit the fiber-shaped LuAG crystals as active material for high-granularity calorimeters. Moreover, the indications that LuAG crystals possess sufficient radiation hardness to operate in the challenging radiation enviroment of high-luminocity LHC, makes it a prominent candidate for the upgrades of CMS calorimetric systems and give rise to the studies described below.

7.1 Beam Tests in 2012

In 2012 two sets of beam tests were performed with the LuAG crystal fibers. A small module formed by a brass absorber loaded with four crystal fibers was tested in May for a proof of concept. As the results looked promising, the decision was taken to continue the studies of possible LuAG implementations for radiation-hard high-granularity calorimetry. Therefore a second beam test was performed in the fall of 2012 with a module loaded with nine crystal fibers of LuAG. This section offers a broad discussion of the tests and their results[56].

7.2 Geometry of the Module

The volume of a brass absorber was shaped to reproduce the tapered geometry and size (approximately $3{\times}3{\times}22\,cm^3$) of a standard $PbWO_4$ crystal used in the endcap of the electromagnetic calorimeter of the CMS experiment. The module is further referred to as mini-CFcal. In this brass element, 9 LuAG fibers wrapped with Teflon were inserted in holes of 3 mm diameter. The Teflon wrapping does not enhance the light output or the light propagation. It is used for protection of the LuAG fibers while handling the brass module (Fig. 7.2).

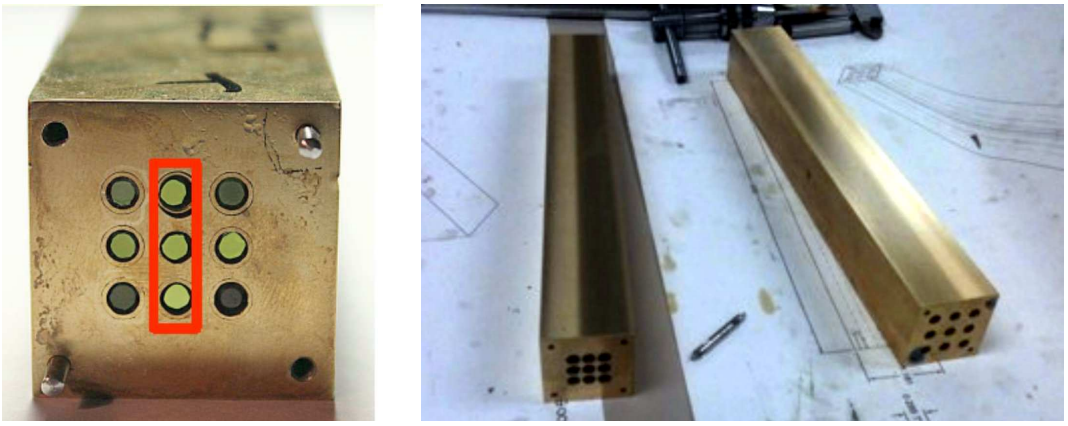

FIGURE 7.2: Tapered brass absorber for the LuAG beam tests. **LEFT:** Front view of the absorber loaded with the LuAG fibers. **RIGHT:** Overall view of the absorber prototypes. The one used for the LuAG beam tests is shown on the left.

The sampling calorimeter prototype has been tested in the H2 test beam line at the Super Proton Synchrotron (SPS) at CERN. The detailed description of this experimental facility is presented in the relevant section.

Multiwire delay chambers were used to provide detailed beam profiles as well as individual particle tracking information. The trigger is provided by the scintillating counters located upstream from the tested prototype.

7.3 Read Out electronics and Data Acquisition system

The mini-CFcal was inserted in the center of a 3×3 matrix of $PbWO_4$ crystals (Fig. **7.3**, top). The signals from those $PbWO_4$ crystals were read out with photomultiplier tubes and was available as part of an online data quality monitor to ensure good beam centering on the mini-CFcal module. According to the technique described in the relevant section, an electron beam, set parallel to the fiber axis, was tuned to have a beam spot of approximately $4\,\text{cm}\times4\,\text{cm}$ to cover the entire mini-CFcal module with a dense core. The beam spread reached $PbWO_4$ crystals with the tails to produce some signal sufficient for effective centering of the prototype. The response of the $PbWO_4$ cells was previously calibrated in independent tests. An example of the $PbWO_4$ outputs for a 100 GeV electron beam is shown in Fig. **7.4** and validate the proper centering of the beam on the mini-CFcal module.

For the light extraction, each extremity of the mini-CFcal was coupled with Silicon grease (Rhodorsil Paste 7) to 9 clear optical fibers (Fig. **7.3**, bottom left) which then transported the analog signal to silicon photomultipliers, SiPM (Fig. **7.3**, bottom right). The cross-section of the optical guides was chosen to be 3 mm in diameter, which exceeds the diameter of the read-out crystal fibers to ensure no signal is transmitted into the cladding and escapes detection.

The SiPMs used are KETEK 20 micron green-sensitive devices with photon detection efficiency (PDE) of 21 % and active area of $2.2\,\text{mm}\times2.2\,\text{mm}$, the gain of which was tuned to be 1 count per photo-electron by AC-coupling with a capacitive divider. The charge signal is measured and encoded into a non-linear digital scale by the Charge Integrator and Encoder ASIC (QIE v8). The QIE uses the LHC clock to divide time into regular bins and measure the accumulated charge in each 25 ns time bin. Internally, the QIE uses capacitors to accumulate the charge and measure the voltage. There are four such capacitors on each QIE, and the QIE uses each capacitor in turn, discharging it for two clocks before using it again. Thus each subsequent time sample comes from a different capacitor. The outputs of three QIE channels are digitally combined onto a high-speed optical link and sent to the HCAL Trigger/Readout (HTR) board. The HTR board buffers the incoming digital data and transfers it to the Data Concentrator Card which in turn transfers data to the central

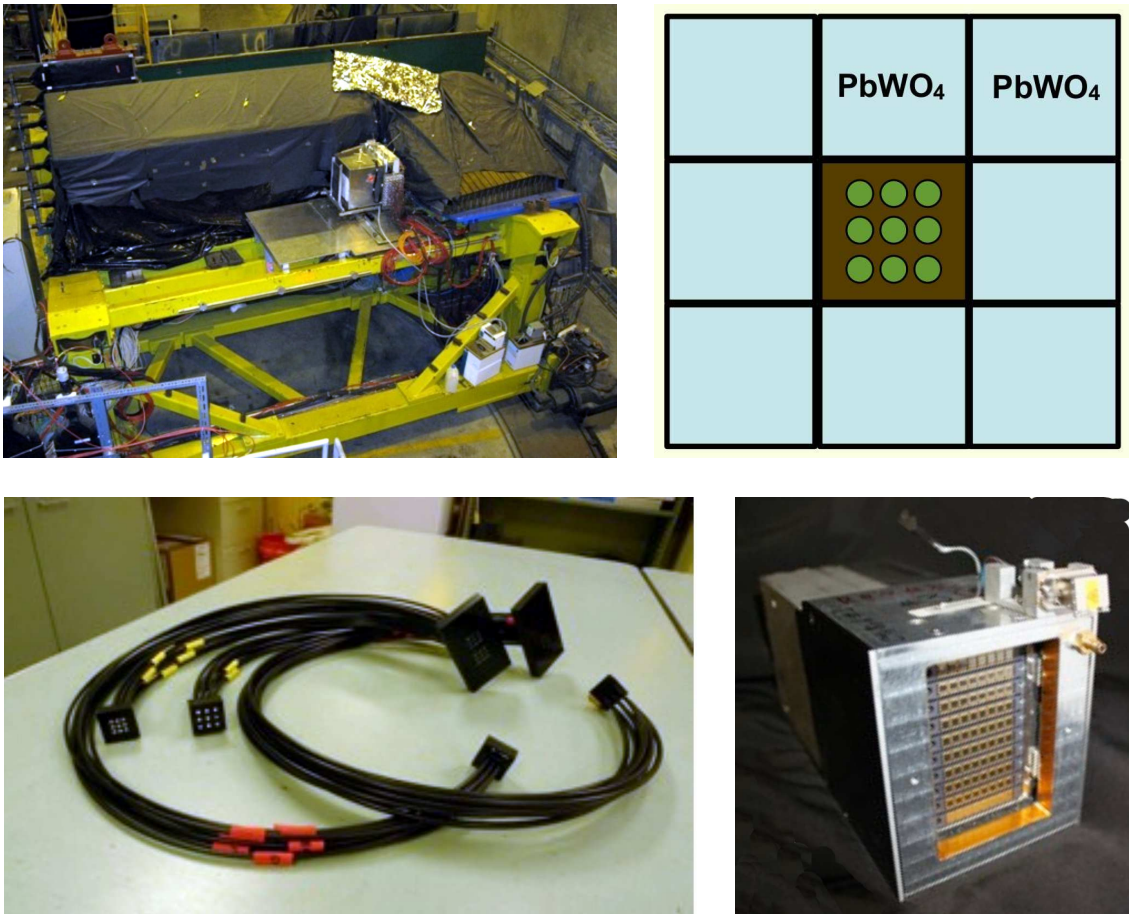

FIGURE 7.3: **TOP LEFT:** Overall view of the installation in the experimental area. When the setup is exposed to the beam, the beam comes from the left. **TOP RIGHT:** Mini-CFcal installed matrix of $PbWO_4$ crystals as seen by the beam. **BOTTOM LEFT:** Bundles of optically clear fibers transport analog signals to the photodetectors. **BOTTOM RIGHT:** Readout module with arrays of silicon photomultipliers.

DAQ[57].

7.4 Wire Chambers

Two delay wire chambers (WCA and WCC) positioned in front of the mini-CFcal were used to monitor the impact point of particles on the absorber (x_i; y_i) by extrapolating the trajectory of a particle:

$$x_i = x_{WCA} + (x_{WCC} - x_{WCA})\frac{z_{WCA}}{z_{WCA} - z_{WCC}},$$

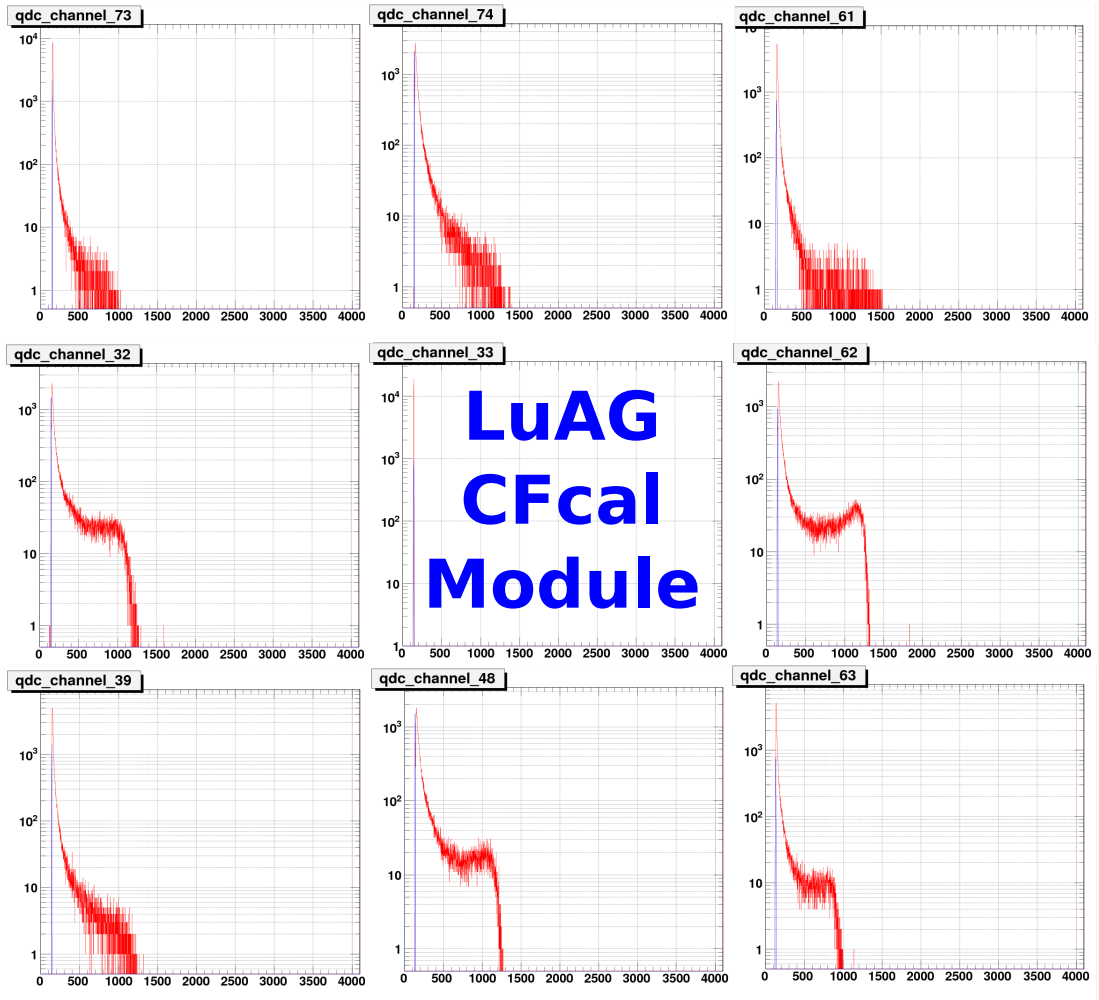

FIGURE 7.4: Signals in the $PbWO_4$ crystals surrounding the mini-CFcal module validate the proper centering of the beam on the module.

where z_{wca} is the distance between WCA and the mini-CFcal module, $z_{wca} - z_{wcc}$ is the distance between the two wire chambers and x_{wca} and x_{wcc} are the horizontal coordinates measured by wire chambers WCA and WCC, respectively. Identical formula with x replaced by y stands for the y coordinate.

The information on the particle position allows the study of the crystal fibers response for each fiber as a function of the impact point. The angular spread of the incoming particles was also estimated and results are shown in Fig 7.5. Both on the x and y axes the average angle of incoming particles is below 0.1 degree with small fluctuations, $\sim$0.02 degree, corresponding to $\sim$1 mm spatial resolution at the target location.

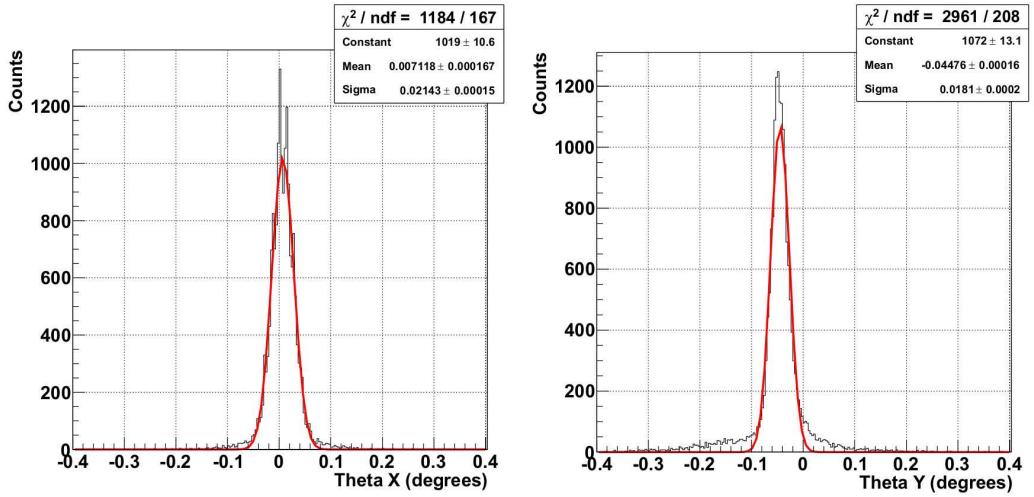

FIGURE 7.5: Distributions of particle angle for 80 GeV electrons. **LEFT:** x (θ_x) **RIGHT:** y (θ_y)

7.5 Response of Ce-Doped and Undoped LuAG Fibers

Two different types of LuAG fibers have been used as active material inside the absorber: Ce-doped fibers to produce scintillation and undoped fibers as Cherenkov radiator. Their response to electrons, with energy between 50 and 150 GeV, has been studied in terms of light output and pulse shape.

Using the wire chambers data a selection of electrons having their impact points within the cylinder of 2 mm radius centered of a given fiber was done and the average pulse shape recorded from the two types of fibers was calculated.

Results corresponding to 80 GeV electrons are shown in the left plot of Fig. **7.6**.

A clear difference is visible between the Cherenkov pulse (measured with undoped fibers) having a fast decay time $< 10\,ns$ and the scintillation pulse (given by Ce-doped fibers). The longer decay time of the undoped fiber was attributed to a Cerium contamination of the Lutetium oxide. In this study the experimental setup only allowed a standard LHC sampling at a period of $25\,ns$, which limits a detailed study of the pulse shape. A more detailed measurement of the pulses performed in [58] is shown on the right plot Fig. **7.6** for comparison.

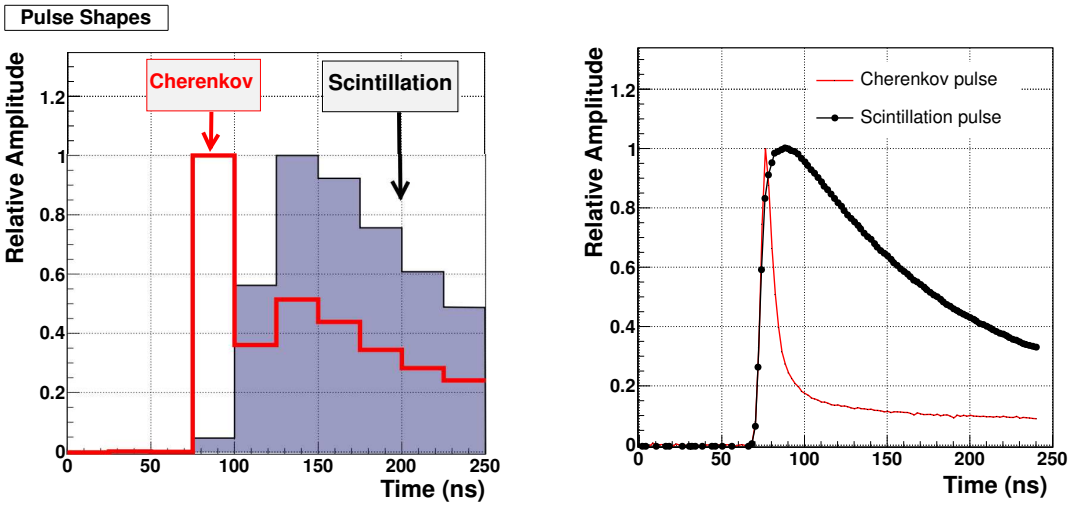

FIGURE 7.6: Comparison between the average pulse shape of a Ce-doped scintillating fiber (in black) and undoped Cherenkov radiator (in red). **LEFT:** Results from this beam test with 25 ns standard LHC sampling for 80 GeV electrons. **RIGHT:** Results from [58] with high sampling rate.

Applying the same beamspot selection, the distributions of signal induced by 80 GeV electrons in the two types of fibers were obtained. The signal of each SiPM has been converted into the number of photolectrons using conversion factors C^i obtained by calibrating each SiPM channel with LED signals. Ce-doped fibers, as expected, show a much higher signal ($\sim$1800 photoelectrons) with respect to the undoped fibers ($\sim$80 photoelectrons), see Fig. 7.7.

These values correspond to photoelectrons measured from the back end of a given fiber only; hence, this number will increase for scintillating fibers, by a factor $\sim$2, if also the front end signal of each fiber is considered. Furthermore, the analog readout is far from being optimal: some fraction of photons is lost in the crystal to optical fiber coupling, then more signal is expected to be absorbed inside the optical fibers used to transport the signal from the crystal fiber end to the SiPMs.

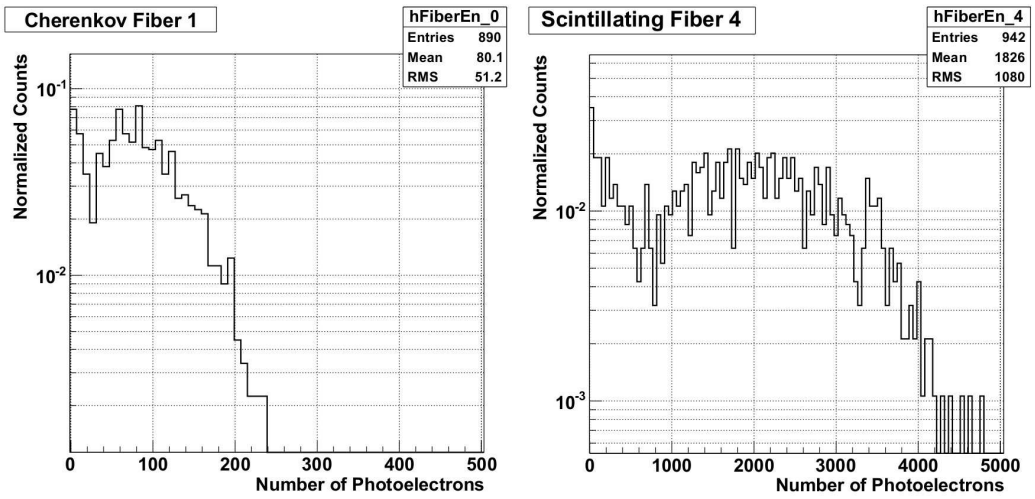

FIGURE 7.7: Distributions of photoelectrons measured from one end of a LuAG crystal using 80 GeV electrons within a cylinder 2 mm in diameter centered around a selected crystal fiber. **LEFT:** For undoped Cherenkov radiator. **RIGHT:** For Ce-doped scintillating fiber.

7.6 Transverse Granularity

To investigate the response of fibers as a function of the electron impact point we made use of the delay wire chambers data to scan along x and y axis the whole mini-CFcal. After a selection of events within $\pm 5\, mm$ on the y axis, the average response of a given fiber for changing the impact point on the x axis was calculated. The same procedure was performed for the y axis. The maximum values IC_x and IC_y of these transverse profiles correspond to the average response of the fiber when the impact point is equivalent to the fiber position, on the x and y axis, respectively. These coefficients are proportional to the light output of each fiber. Therefore, we can then define intercalibration coefficients between fibers as follows:

$$IC^i = \frac{IC^i_x + IC^i_y}{2}.$$

This intercalibration procedure is necessary to normalize the signal from different fibers in order to take into account their different light output which is related to the cerium concentration, fiber quality and the optical coupling between crystal fibers, optical fibers

and SiPMs. The normalized distributions for the central row and central column fibers are shown in Fig. **7.8**. Transverse profiles on the y axis show narrower peaks around the fiber positions reflecting the higher quality of the beam profile on the y axis with respect to the x axis.

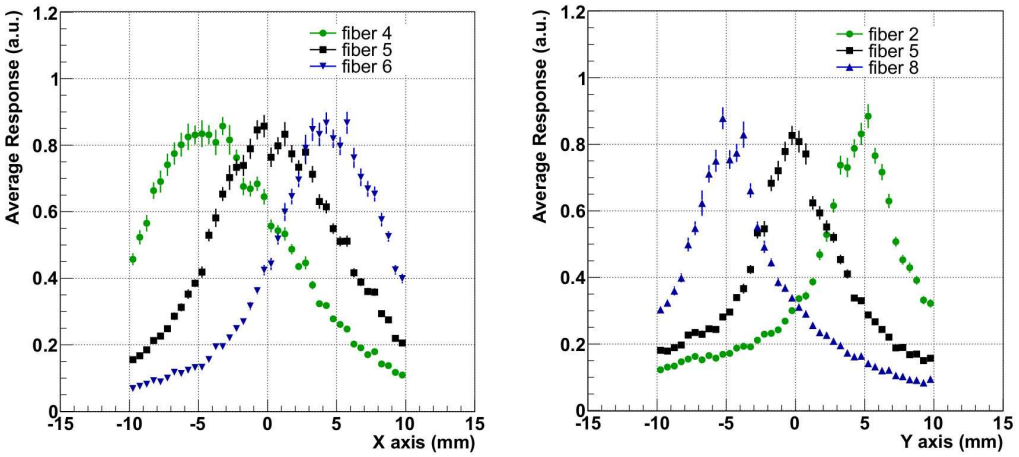

FIGURE 7.8: Average response of the central crystal fibers as a function of impact point along the corresponding axis. **LEFT:** Fibers of the central row. **RIGHT:** Fibers of the central column.

7.7 Energy Reconstruction

Applying intercalibration coefficients, the particle energy can be reconstructed using the contribution from different fibers in order to collect the maximum fraction of energy deposited by the shower in the mini-CFcal. Events within a cylinder of $5\,mm$ radius centered around the central fiber have been selected in order to consider only electrons which start the shower inside the array of fibers. The contribution of each fiber, after intercalibration, has been summed up event by event to reconstruct the signal:

$$E_{reco} = \sum_{i=1}^{9} S^i_{front} C^i IC^i,$$

where S^i_{front} is the signal measured from the front end of each fiber i, C^i are calibration factors to convert the SiPM channel into photoelectrons, obtained using a LED signal as

reference, and IC^i are the intercalibration coefficients.

For the energy reconstruction only signals from the front end of the fibers have been used, since for two fibers the back signal was not available because of the erroneous tuning of the corresponding SiPM voltages. If all back readouts were available, reconstructing the signal using both front and back signals could slightly increase the resolution because of the higher photostatistics. Using electrons at different energies between 50 and 150 GeV, we studied the evolution of the fibers array response. The obtained distributions of the reconstructed amplitude E_{reco} are then fitted with a Gaussian function to estimate the peak position which shows a good correlation with the beam energy as shown in the right plot of Fig. **7.9**. The energy resolution of the reconstructed amplitude varies from 15% to 20% and is dominated by a constant term due to the transverse non-uniformity of the response and experimental systematics discussed later.

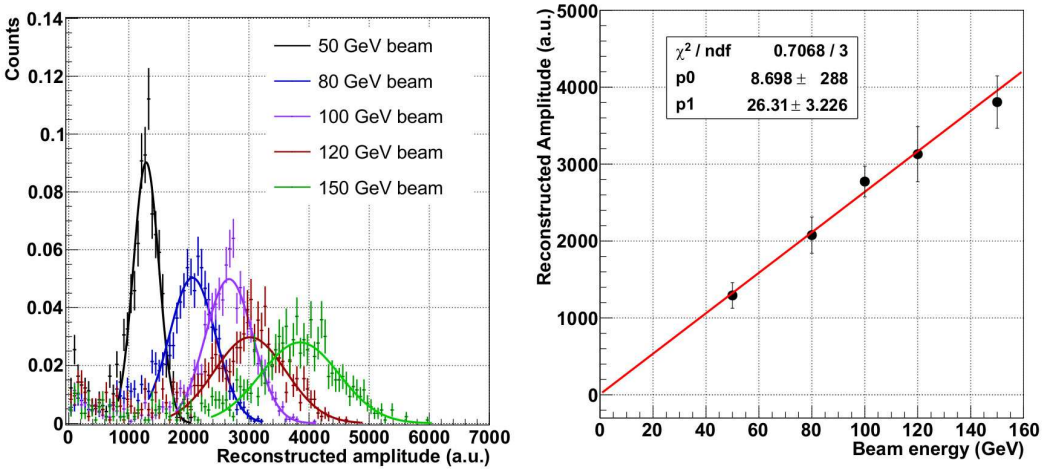

FIGURE 7.9: Reconstructed amplitude. **LEFT:** Distributions of reconstructed amplitude E_{reco} at different beam energies. **RIGHT:** Correlation between the peak value of E_{reco} distributions and the beam energy with a linear fit (in red). Error bars correspond to the statistical error on the estimation of the peak position.

7.8 Longitudinal Shower Profile

As the energy E of incoming electrons increases, the position of the shower maximum t_{max} moves towards the back of the absorber according to:

$$t_{max} \propto \ln(E).$$

This change in the shower profile along the longitudinal axis z is expected to produce a different ratio of the front and back signals measured at the two opposite ends of each fiber. We can define a dimensionless estimator of the shower maximum position as follows:

$$R_{BF} = \ln\left(\frac{S_{back}}{S_{front}}\right),$$

where S_{front} and S_{back} are respectively the signals measured at the front and back end of a fiber. The value of R_{BF} has been estimated for both Cherenkov and scintillating fibers using different beam energies in the range from 50 to 150 GeV. A zone delimited by the cylinder with 5 mm radius centered around the selected fiber has been selected in order to reduce the noise background. In Fig. **7.10** results obtained with the Cherenkov fiber are shown.

We observed a clear correlation between the value of R_{BF} and the beam energy which demonstrates the feasibility of longitudinal shower profile studies using a double readout technique. Similar results are obtained using the scintillating fiber and are shown in Fig. **7.11**.

The different nature of scintillation and Cherenkov light, the former being emitted isotropically whereas the latter has a prefered direction, can explain the difference between the two types of correlations. As expected, the Cherenkov fiber shows a much higher signal in the back readout with respect to the front one. The value of R_{BF} is also expected to show a correlation with the impact point of electrons (along the x and the y axis) since the fraction of the electromagnetic shower which interacts with a fiber will move towards the back end when the shower develops far from the fiber position, as represented in the sketch of Fig. **7.12**.

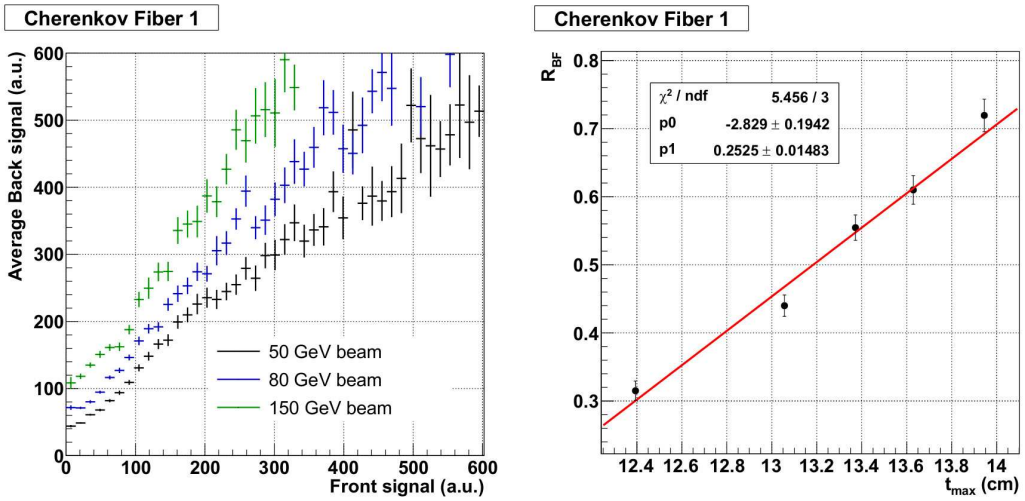

FIGURE 7.10: Front-back correlations for the Cherenkov radiator crystal fiber. **LEFT:** Correlations between front and back signals of a Cherenkov fiber for different energies. **RIGHT:** Correlations between R_{BF} and a theoretical t_{max} position for a given beam energy with a superimposed linear fit result. Error bars correspond to the statistical uncertainties on the data points.

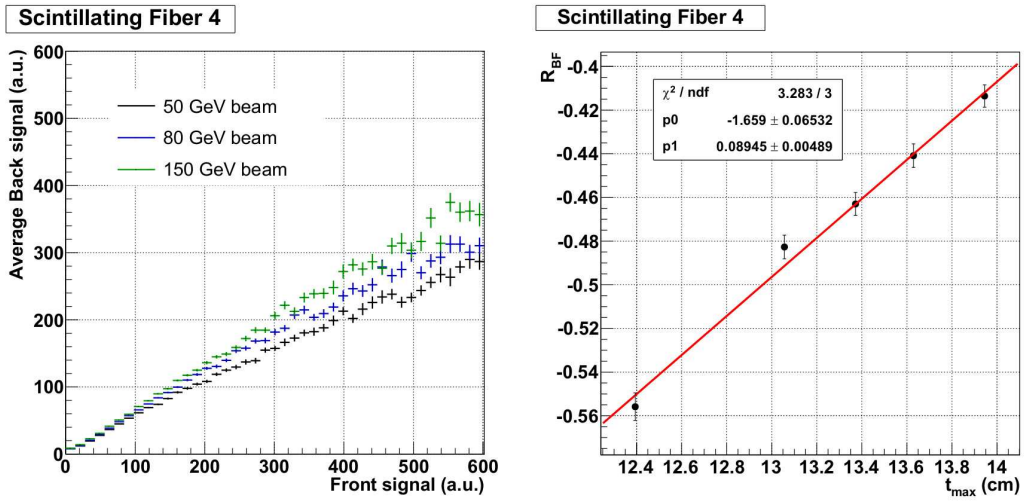

FIGURE 7.11: Front-back correlations for the Ce-doped scintillating crystal fiber. **LEFT:** Correlations between front and back signals of a scintillating fiber for different energies. **RIGHT:** Correlations between R_{BF} and a theoretical t_{max} position for a given beam energy with a superimposed linear fit result. Error bars correspond to the statistical uncertainties on the data points.

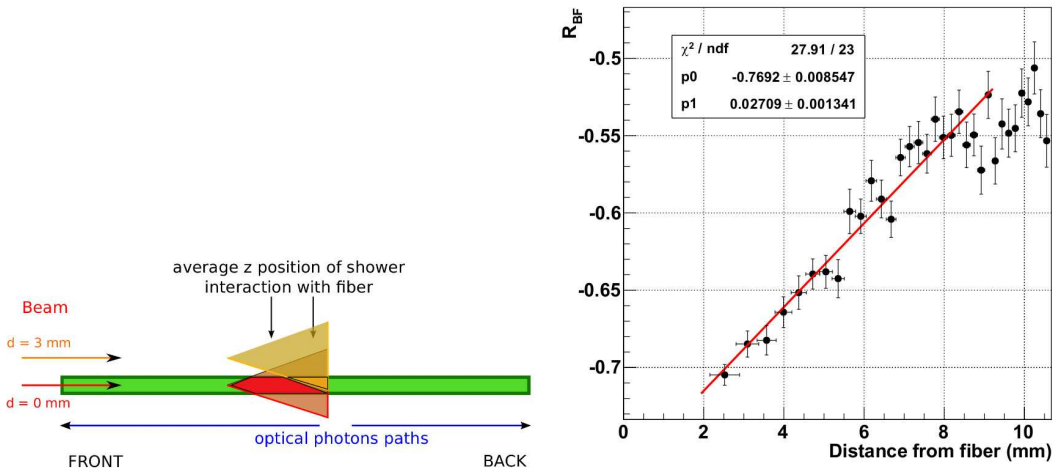

FIGURE 7.12: **LEFT:** Naive sketch representing the drift of the average interaction point of the shower with a given fiber, when the impact point moves away from the center of fiber. **RIGHT:** Correlation plot for the value of R_{BF} and the distance between the impact point and a fiber. The result of a linear fit in the range $2 - 9\,\text{mm}$ is superimposed in red. Error bars represent the statistical uncertainty on the data points.

To study the effect of the impact point on the value of R_{BF}, we selected events within concentric cylinders at a given distance from the selected fiber and calculated the average value of R_{BF} for each ring. Results are shown in the right plot of Fig. **7.12**. As expected, we observe a significant correlation between the distance of the electron impact point from the fiber and the value of R_{BF}. The back signal grows linearly with respect to the front signal, when electrons initialize the shower further from the fiber. In such conditions, only a small fraction of the shower interacts with the fiber reducing the scintillation signal which, in turn, increases the sampling fluctuations.

7.9 Summary and Discussion of Results

The test beam results presented here confirm the potential of LuAG fibers for high energy physics applications. A significant amount of light was extracted from both the Cherenkov and the scintillating fibers. The response of single fibers to electrons depends on the impact point of the particle and thus it can be used to study the transverse profile of the shower. The combination of the signals from clusters of adjacent fibers can be used to build algorithms

which allow an estimation of the particle impact point and angle.

The feasibility of using double readout (i.e. making use of signal from both front and rear ends of each fiber) to increase the knowledge of the shower profile along the fiber axis has been investigated. Good correlations of the back and front signals ratio R_{BF} with the shower maximum position (along z axis) and with the impact point of electron on the mini-CFcal front face (x, y axis) were found. The optimization of the double readout can provide even more information on the longitudinal shower profile without the necessity to increase the longitudinal segmentation and hence the number of channels. More issues related to the real potential of such calorimeter in the context of particle flow algorithms or dual readout corrections (i.e. reading out the scintillation and Cherenkov light separately on an event by event basis to correct for hadronic shower fluctuations) are not addressed here, because of the small dimensions for this prototype and due to the low number of fibers involved. Nevertheless, current data can be used to validate simulation tools in order to investigate new geometries and configurations. A Geant4 simulation[59] has been performed to allow a first comparison with data and to investigate the potential of a larger array of fibers in terms of energy resolution. The same geometry of the mini-CFcal, in terms of fiber packing, has been simulated extending the array of fibers to a 41×41 matrix inserted in a brass absorber with transverse dimensions of 22 cm×22 cm. Such geometry, shown in Fig. **7.13**, left, will be referred to as Geometry A. A different geometry (Geometry B) was also simulated, in which the gap between the fibers and the absorber (resulting from the 0.5 mm layer of Teflon) has been reduced to 0.1 mm. Hexagonal packing was chosen here so that the spacing between fibers centers is reduced to 3 mm (see Fig. **7.13**). In this case, a 123×123 matrix of 22 cm long fibers is needed to fill a brass block of $\sim$ 33 cm×33 cm×22 cm.

Electrons of energy between 1 and 150 GeV, uniformly spread on a $10\,mm \times 10\,mm$ area and with a small angular spread of 5 $mrad$, which aims to reproduce the experimental conditions of the test beam, have been simulated. For Geometry A, the electrons direction was oriented in the same configuration as in the test beam whereas for Geometry B the electrons beam direction was set perpendicular with respect to the fiber axis in order to reduce the non-uniformity of the response. The energy deposited by the electromagnetic shower inside the active volume of LuAG fibers has been measured and allowed to study

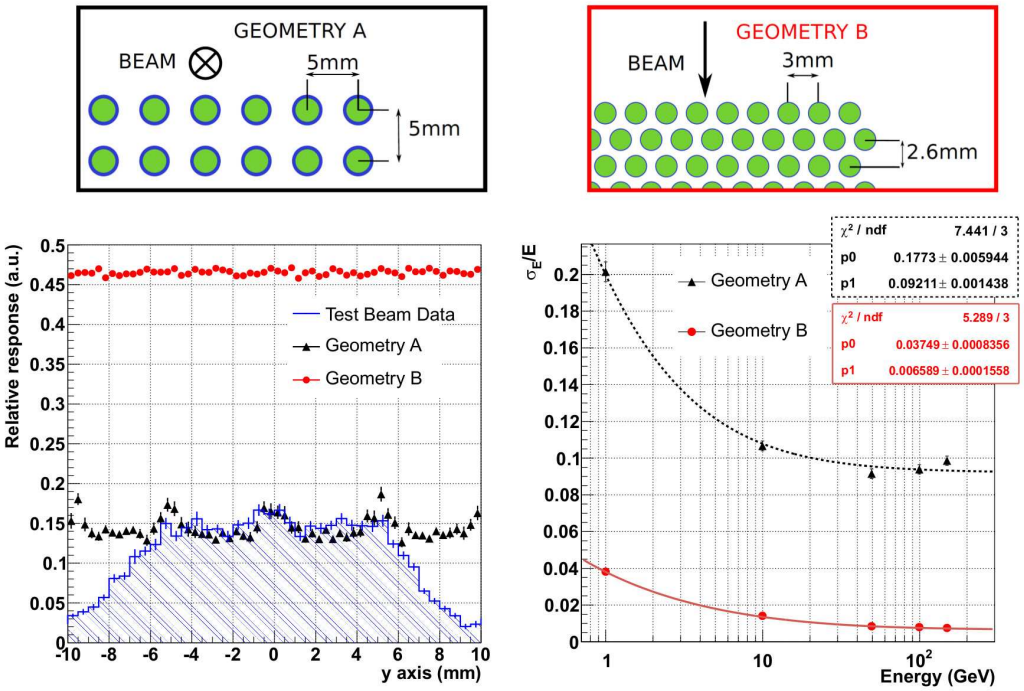

FIGURE 7.13: **TOP LEFT:** Geometry A. **TOP RIGHT:** Geometry B. The blue gaps between fibers, shown in green, and absorber, shown in white, represent the Teflon layers. The beam direction is also shown. **BOTTOM LEFT:** Fraction of electron energy deposited in the array of fibers as a function of a 50 GeV electron impact point along the y axis for Geometry A (black) and Geometry B (red). Experimental data points are shown with a blue line. **BOTTOM RIGHT:** Energy resolution curves for Geometry A (black) and Geometry B (red) at different beam energies fitted using $\sigma_E/E = \sqrt{p_0^2/E + p_1^2}$, where p_0 and p_1 represent the stochastic and constant terms, respectively.

the transverse non-uniformity of the response as shown in Fig. **7.13**.

We can observe that the response of the mini-CFcal decreases when the impact point of electrons is out of the fiber array of ± 5 mm. In both data and simulation of Geometry A the response fluctuates periodically when the impact point moves from the center of the fibers to the brass between adjacent fibers. When the granularity and the packing configuration are improved (for instance, in Geometry B), the total fraction of the shower collected in the active volume is increased by approximately a factor of 3 and the non-uniformity of the response is reduced. The evolution of the energy resolution with respect to the electron energies is shown in the right plot of Fig. **7.13**. Of particular interest is the resolution that

can be achieved with the granularity of Geometry B in a non-pointing fiber configuration which has a stochastic term of $\sim$ 3.7% and a constant term of $\sim$ 0.7% due to partial containment of the shower and sampling fluctuations.

Such a good resolution is achieved by means of rotating the detector by 90° which results in a better transverse uniformity of the response which was one of the main limitations to the energy resolution of Geometry A.

The predicted energy resolution for Geometry A ($\sim$10%) is better than the experimental resolution of the distributions in Fig. **7.9**, which is $\sim 15-20\%$. The difference is related to several factors: a poorer transverse containment of the shower due to the smaller array of fibers in the mini-CFcal, the contribution of the electronic noise, the limited precision of intercalibration coefficients between fibers and other systematics related to the experimental setup and beam quality.

7.10 Perspectives and Outlook

Supported by the results obtained with this first test beam campaign, it is worth while to investigate possible designs to implement this technology in a real calorimeter for high energy physics. Although, in the present study, only the response to electrons has been deeply investigated, the potential of a crystal fiber calorimeter to improve the resolution of hadronic showers using dual readout techniques was previously investigated in [58]. It was demonstrated that a fraction of active volume similar to the one of Geometry B (around 45%) would allow for the application of dual readout corrections which can improve the energy resolution of the hadronic shower reducing the stochastic term below 30%.

In addition to the dual readout potential of this material, the good energy resolution for electromagnetic showers that can be achieved with configurations similar to Geometry B (top right sketch in Fig. **7.13**) suggests the feasibility to integrate an electromagnetic and a hadronic calorimeter into a new type of detector which can satisfy both requirements. In particular, the very peculiar shape of crystal fibers, which can be grown with different diameters and lengths, turns out to be a very flexible tool which makes it possible to optimize their implementation into a calorimeter. A possible way of packing crystal fibers, in order

to fill a big and shaped volume like the one of a real detector, is shown in Fig. **7.14**.

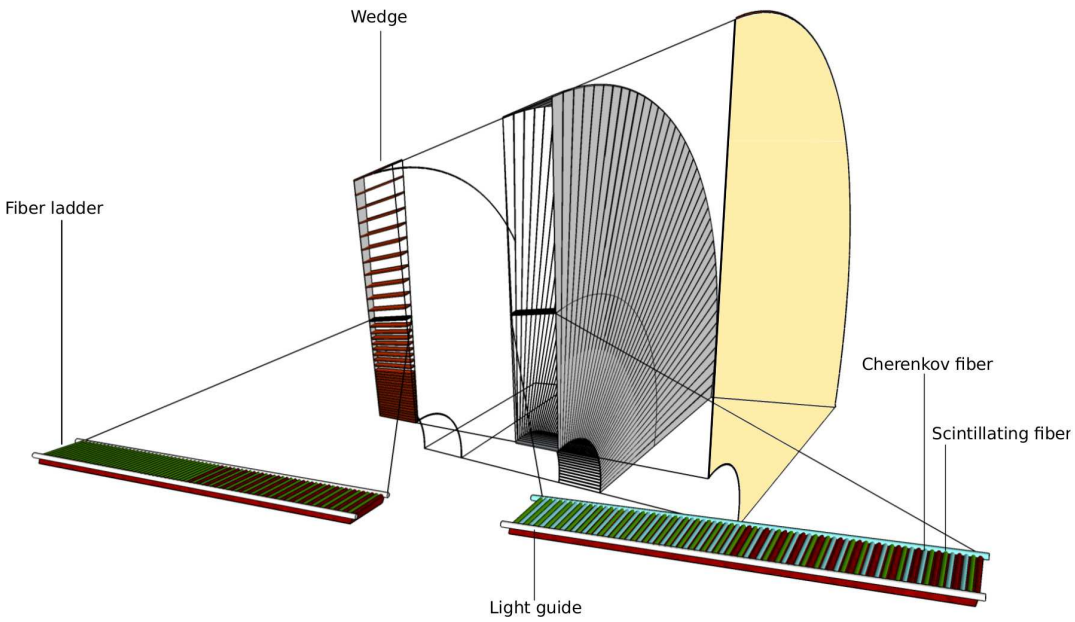

FIGURE 7.14: Possible implementation of crystal fibers into a real calorimeter of $\sim$1.7 m length and external radius varying from 1.2 to 2.4 m shaped into a projective geometry with respect to the interaction point. The basic cell contains several Cherenkov (blue) and scintillating (green) fibers of 2 mm diameter, read out by two separate light guides (white) which transport the signal to the photodetectors. These basic cells are then assembled into shaped wedges to fill the whole detector volume. Two separate layers with high granularity and the second layer could represent a first part of a hadronic calorimeter with lower granularity and dual readout option implemented (i.e. reading out the scintillation and Cherenkov light separately.)

Several fibers of variable length between 1.5 and 7 cm are grouped together into a ladder-like structure in which the signals from all the fibers are readout by means of a light guide, i.e. a wavelength shifter and quartz capillary system (see corresponding section for details), which transports the signal to the photodetector. Within a fiber-ladder, the composition of scintillating and Cherenkov fibers as well as the spacing between them can be varied to optimize the detector perfomance and reduce the cost. The Cherenkov and the scintillating signals could be readout using two separate light guides which collect the light from the two opposite ends of the fibers. This particular ladder-like structure minimizes the optical path of photons inside the active volume of crystal fibers reducing the time jitter

and the light absorption. These fiber-ladders can then be assembled into wedges of different size and shape in order to fit a projective geometry. The length of the ladders and the spacing between them can be used to tune the fiber granularity along the longitudinal and radial coordinates in order to better fit the detector requirements.

7.11 Conclusions

The test beam study presented above, demonstrates the potential of LuAG crystal fibers for high energy physics calorimeters. The two different kinds of fibers tested allow for efficient detection of scintillating and Cherenkov radiation.

The small prototype (mini-CFcal), which was tested at CERN SPS facility with electrons of energies between 50 and 150 GeV, replaced a single crystal of CMS ECAL in size and shape and hence can be considered equivalent to a single calorimetric channel. The measurements of the mini-CFcal were used to reconstruct the energy of electrons with good energy linearity and to study the shower profile laterally and longitudinally due to its high granularity and double readout (front and rear ends of each fiber). Present results have been used to validate a simulation, based on Geant4, which is used to investigate electromagnetic and hadronic calorimeters for high energy physics. By tuning the fraction of active volume and the configuration of fibers inside the detector, a good energy resolution to electromagnetic showers can be achieved. Based on the above results, further test beam studies were planned to deeply investigate different fiber configurations in a larger prototype and its response to electromagnetic and hadronic showers especially in terms of tracking (photon pointing), shower profile reconstruction and dual readout.

Chapter 8

Quartz capillaries

In calorimeters showering particles produce scintillating light inside of a relatively large volume of an active material. The light then has to be transported to the photodetectors. As the size of the light-sensitive window in photodetectors is typically quite small, the light eventually has to be collimated into a thin lightguide. However, the naive design of a gradually shrinking light-transporting channel would be in contradiction with Liouville's theorem, which requires that the phase-space distribution function remain constant along the trajectories of the system. In other words, this naive light transport system would loose photons as the cross-section of the light-pipe goes down. The solution of this problem frequently employed in the detectors is often referred to as wavelength shifting. In a nutshell, the scintillating light is collected by the optical guide made of a material which absorbs the light and re-emits it in form the of less-energetic photons (i.e. bigger, shifted wavelength). This red-shifted light can be further transmitted without any conflict with Liouville's theorem. The compression factor is governed by the exponent of the ratio of the energy shift to thermal noise, and hence even a small red-shift allows for the use of light guides with

cross-sections orders of magnitude smaller than that of the scintillating volume.

There is a wide range of chemicals which exhibit this handy property of red-shifting the light. For many reasons however those substances are not used in pure form (as the macroscopic amounts of those chemicals are non-transparent, lack structural durability, etc.) and therefore the standard wavelenth shifting materials are their weak solutions in transparent plastics rather than pure substances[1]. The wavelength shifting plastic can then be used to produce the core of the optical fiber, which then serves as a (part of the) light guide. This arrangement works perfectly fine for many applications; however, radiation levels which are foreseen to be experienced by the detectors in the high luminosity LHC era are certainly beyond what those materials can tolerate and hence a conceptually new approach needs to be developed.

8.1 Light Emitting Cores

An interesting opportunity originates from the above-mentioned fact that the standard wavelength shifting materials are in fact weak solutions of wavelength shifting chemicals in transparent plastics – it is the plastics which exhibit the radiation damage at first and loose their optical properties. However, even when the plastic foundation of a wavelength shifter looses its transparancy and tends to absorb a higher and higher fraction of the light, the wavelength shifting chemical itself is still in a good shape to serve its purpose. So, the material still red-shifts the light, but cannot transport it. Therefore the problem of radiation damage would be solved if there was an alternative way to transport the signal, once it was ”cooled”.

The conceptual design was proposed by Randal C. Ruchti from the University of Notre Dame in the course of the internal collaboration meetings of the CMS HCAL, and the following presents the initial lab tests for the proof of concept and further beam tests at the H2 facility at CERN.

[1] In some cases the wavelength shifting substances are even diluted in the scintillating plastic itself, if the scintillating light is in the UV range – the UV light is strongly attenuated in many of the materails which are transparent to visible light. Therefore the wavelength shifter is needed even to extract the light from the scintillator before it gets fully absorbed.

If a wavelength shifting fiber is enclosed in a radiation-hard transparent shell, then the scintillating light can penetrate such a shell and be absorbed and re-emitted in the wavelength shifting fiber. As the light gets re-emitted in all directions, part of it is emitted in the directions suitable to be trapped in the shell by total internal reflection. This light hence is further transmitted along the ”complex fiber” and can be either transferred into another light guide or directly registered by a photodetector. As the light mostly travels in a transparent shell, which remains so with irradiation, the degradation of the optical properties of the wavelength shifting plastic in the core of a complex fiber is not supposed to dramaticly affect the performance. It is also possible to fully eliminate the contribution of the light-emitting core to the light transport by reading out the signal only from the radiation hard shell, but not the core. In the case where a light-emitting core is a fiber, this is achieved by placing a mirror at the end of the fiber.

The quartz capillaries looked like a promising candidate for the shell of such a complex fiber. On the market those are offered by various manufacturers and in a wide range of materials including fused silica glasses, which are proven to be radiation hard in the range of doses of interest (for example, see [60]). The complex fibers with light emitting cores utilizing such capillaries are shown in Fig. **8.1** along with a sketch which demonstrates the principle of operation.

8.2 Primary Tasks for the Bench Tests

With this conceptual design in hand, a collection of technical questions had to be addressed. After positively answering the primary question if the design is viable at all, all further issues could be attributed to one of the categories as follows:

- Light emittance by the core.

  This mainly includes radiation damage studies of the wavelength shifter. As the foundation plastic gets less transparent, the amount of light escaping the wavelength shifting core will degrade. However, if the attenuation length of the core material does not go below a certain limit, such degradation can be accounted for by proper re-calibration.

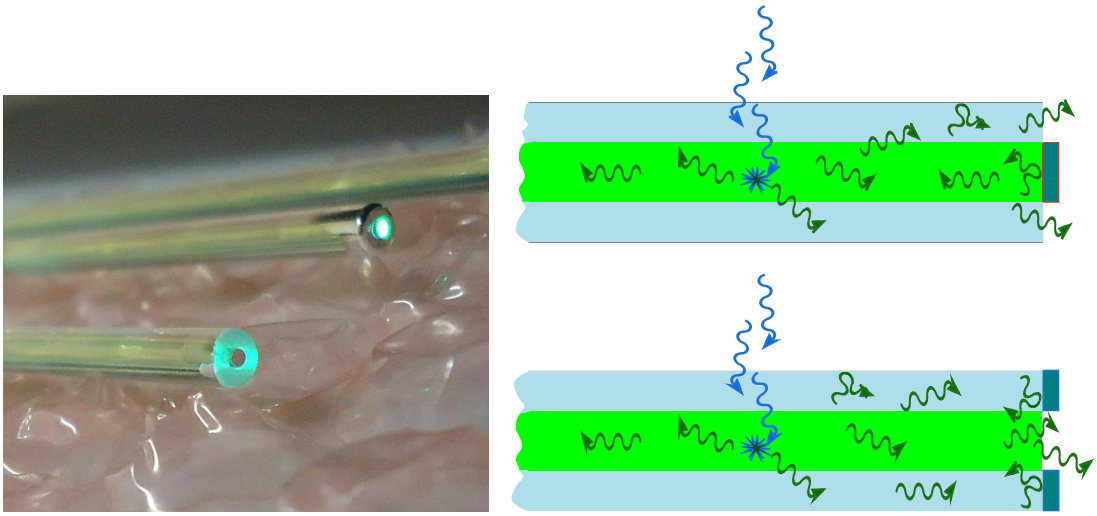

FIGURE 8.1: Quartz capillaries with light emitting cores. **LEFT:** Capillaries for single-side read-out: the core and the shell have mirrors on the opposite ends. **RIGHT:** A sketch of operation: the light is absorbed and re-emitted in random directions at longer wavelength in the core, the fraction which is trapped in the shell then propagates to the ends. **TOP:** Reading out only the shell by placing the mirror on the core's end minimizes the variation of the signal due to the radiation damage of the core. **BOTTOM:** The opposite position of a mirror as an option for the non-readout end.

- Light trapping and propagation by the shell.

  This category includes the issues of optical coupling between the light emitting core and the light transporting shell, conditions of efficient light transport in the shell as well as the attenuation effects in it.

- Reading out the signal from the shell. This category is tightly related to the previous one, as the design of a readout system can help to correct for the attenuation effects. Another important aspect is the pulse shape of the signal, and their timing characteristics in particular.

However, the tests described below represent preliminary studies. They were mostly focused on qualitative analysis of the described design and establishing general principles and limitations for its implementation. The plots in this chapter hence show no error bars: while statistical errors are negligibly small, systematical errors are clearly dominating. One of the main goals of the tests described below is in identifying the possible sources of the

systematical errors. However, precise determination of their values requires independent, broad studies, and only after the final design of the ”light emitting core”-based readout will be settled.

8.3 Laboratory Setup

The laboratory tests of complex fibers with light emitting cores were carried out with the setup shown in Fig. **8.2**. The complex fiber was placed in a light-tight black box and supported at two points close to the ends. A bridge with a build-in LED was installed in the box in such a way that it could slide along the fiber and keep the same distance to the surface of the fiber at the same time. The collimated beam of UV light from the LED was penetrating the fiber perpendicularly to its surface; it simulated scintillation light and could excite the wavelength shifting core of the complex fiber at a desired location along its length by sliding the bridge to the desired position. A PIN diode located at one of the ends of a complex fiber was reading the output from the shell, but not the core of the complex fiber. All the measurements with this setup were performed with the LED permanently on and hence did not include the studies of timing characteristics.

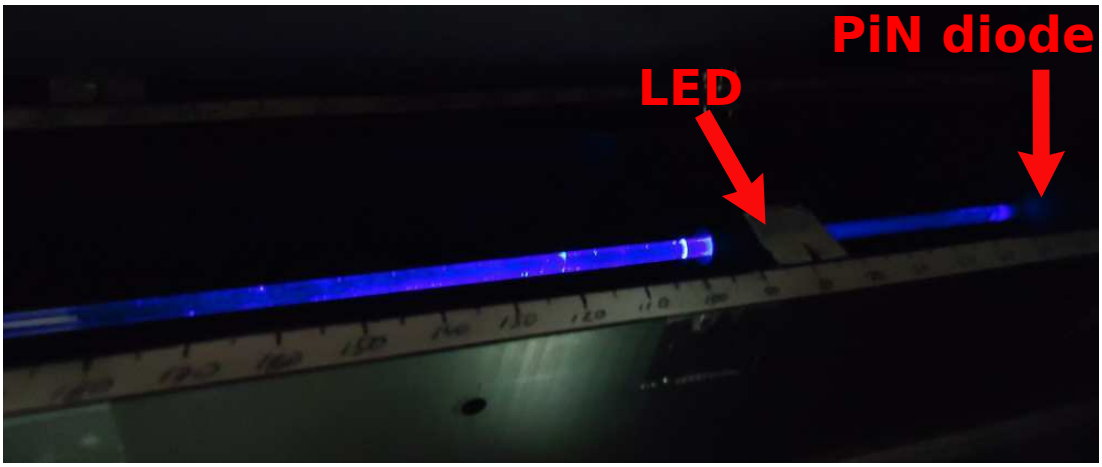

FIGURE 8.2: Laboratory setup for studying the performance of complex fibers with light emitting cores. The wavelength shifting core enclosed in a quartz capillary shell is excited by the UV light of a mobile LED. The light output of the shell is measured by the PIN diode at the end of the fiber.

This setup was used to study various sizes and types of light emitting cores (Y11, SCSF-81MJ, EJ-309, LuAG) and different sizes of quartz capillary shells (with outer ⌀3 mm, inner ⌀1 mm, 2 mm, and with lengths of 20 cm, 25 cm, 30 cm long) as well as the conditions of their performance. The sections below represent only a few instructive examples of measurements to illustrate the principle findings about complex fiber operation.

8.4 Test of wavelength shifting Y11 cores

This wavelength shifting fiber from KURARAY was the first candidate for study as it is this type of fiber that is used in the current design of the CMS HCAL. It is therefore an important and well studied reference material.

Y11 is a bright wavelength shifting fiber with its emission spectrum in the green part of the visible spectrum. It is those fibers that are shown in Fig. **8.1** on the left.

Several fibers of this type were glued into the quartz capillaries with transparent optical glue and tested on the setup described above. The quartz shell was read-out on one end, while the opposite end of the shell was covered with reflective paint. The core had the end close to PIN diode painted. Several effects were observed at this stage.

First of all, from the construction of the fiber with light emitting core it follows that it should be quite sensitive to contaminations of its surface. Indeed, this complex fiber is essentially a kind of un-cladded fiber, as the light-transporting quartz shell acts like a core of a normal fiber. Therefore if the surface of the quartz capillary is contaminated with material with a refractive index in the range between those of the air and quartz, the full internal reflection will not take place for some range of angles of incidence. While this effect is frequently desired in fiber optics[1], in this particular case it only leads to unwanted lowering of light trapping efficiency. If, moreover, the contamination material has a refractive index which is higher than that of the light-transporting shell, then the incident light in a full range of angles of incidence will be able to undergo refraction at this point of the

[1] Cladding fibers with a material of refractive index slightly below than that of the fiber itself is used to suppress the modes highly deflected from the fiber axis – as those modes travel larger distance than those close to fiber axis direction, they cause broadening of the signal and hence limit the number of signals which can be transmitted in a unit of time.

shell-contamination boundary. In practice, a single fingerprint was sufficient to completely mess up the performance. Therefore for all measurements the surface of quartz shells was thoroughly cleaned with ethanol and all fiber-handling operations had to be performed in protective gloves.

Secondly, proper optical coupling between the core and the shell was required (in the case of tests with Y11 cores, optical glue served this purpose), and the quality of such coupling directly affected the measured light output. An example of optical coupling effects on the performance of the complex fiber is demonstrated in Fig. **8.3**. The plots present the PIN diode current as a function of the distance between the LED and PIN diode measured for four different fibers. As mentioned above, the statistical errors are negligibly small, systematical ones come from the pecularities of the fibers: while visual examination of capillaries two and three (shown in yellow and red) did not reveal obvious imperfections (good fibers), the other two (with numbers one and four, shown in blue and green, respectively) displayed cracks and lacunae in the glue (bad fibers). While all fibers demonstrate moderate attenuation, it is clear from the plots that ”good fibers” demonstrate firm attenuation trend, which is easier to correct for, as well as higher light outputs. ”Bad fibers”, on the other hand, demonsrate irregular, non-monotonic attenuation, confirming the importance of high-grade optical coupling between the core and the shell.

8.5 Tests of Liquid Scintillating EJ-309 Core

This liquid scintillator from ELJEN, when excited, emits blue light. A complex fiber with this type of core is shown in Fig. **8.2**. It was included into those studies because of the interesting possibility to build a system with a circulating liquid circuit for light-emitting cores, where radiation-damaged liquid could be pumped out and replaced outside of the long-term shutdowns and maintenance periods, if necessary.

For the tests this viscous liquid was injected into the quartz capillary and sealed there with small rubber corks on both ends. This way the liquid core naturally did not contribute to the output signal. The optical coupling of the core and the shell did not require additional materials. However, removing all the air bubbles without involving a complex dedicated

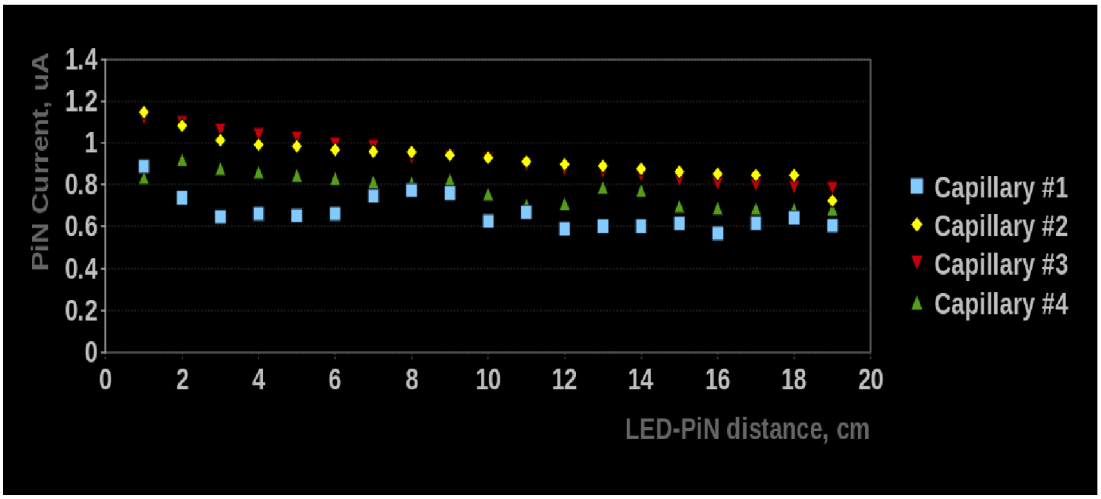

FIGURE 8.3: Light output (PIN diode currents, μA) as a function of distance between LED and PIN diode (in cm) for complex fibers with Y11 core. Fibers 2 and 3 with flawless optical coupling demonstrate monotonic attenuation. Faulty fibers 1 and 4 show non-monotonic result, confirming the importance of a smooth core-shell transition.

technique was impossible due to the significant viscosity of the scintillator and small inner radius of the quartz shell. The effect of non-homogeneity introduced by the bubbles is reflected in Fig. **8.4**. The dependance of the photocurrent on the distance to the photodetector demonstrates systematic discrepancy with monotonic attenuation due to bubbles in the liquid core. The latter effect has to be carefully avoided, especially for the circulating liquid circuit design, where both timely outgassing of the scintillator and studies of cavitational effects in the circuit have to be performed.

8.6 Double-Sided Readout for SCSF-81MJ Scintillating Core

The data shown above represent the results of a single-sided read-out of complex fibers with light emitting cores. Those preliminary results show that the attenuation length of the complex fibers is about 50 cm. However, if double-sided readout is employed instead, the attenuation effect can be partially compensated.

Fig. **8.5** presents the results of single-sided and double-sided readout of a complex fiber

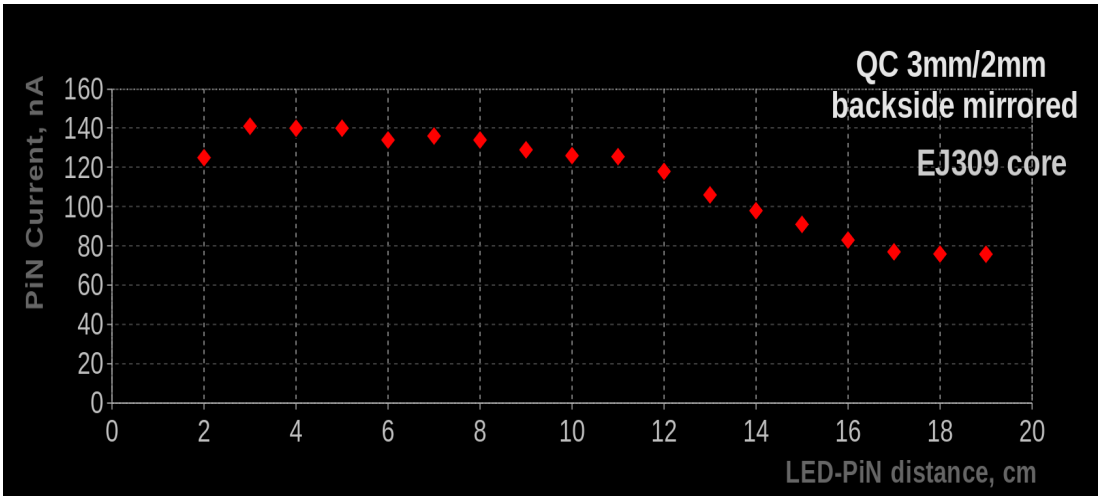

FIGURE 8.4: Light output (PiN diode current, μA) as a function of distance between LED and PiN diode (in cm) for complex fibers with liquid scintillating EJ-309 core.

with the core made of SCSF-81MJ scintillating fiber from KURARAY. The sum of signals from the ends of the fiber remains nearly constant, while the single-sided readout exhibits moderate attenuation of the signal.

It is worth while to note that such summation of the signal can be performed not only on the digitalized signals read out by independent photodetectors. This can also be achieved at the analog level by guiding the signals from both ends to the same photodetector. Such approach can be beneficial in the case of the low light yields and high levels of noise in the front-end electronics.

8.7 Radiation Damage Studies of Y11 Core

The comparison of irradiated and non-irradiated cores of complex fibers is shown in Fig. **8.6**. Wavelength shifting fiber Y11 is used in this case. The optical coupling between the core and the shell is done by means of water.

After the first set of measurements the fiber was irradiated at the PS irradiation facility at CERN with a proton beam up to 40 Mrad. This plot demonstrates the results of measuring the photocurrent for the fiber before and after irradiation and with and without quartz capillary shell. In all cases plots represent the result of a single-sided read-out.

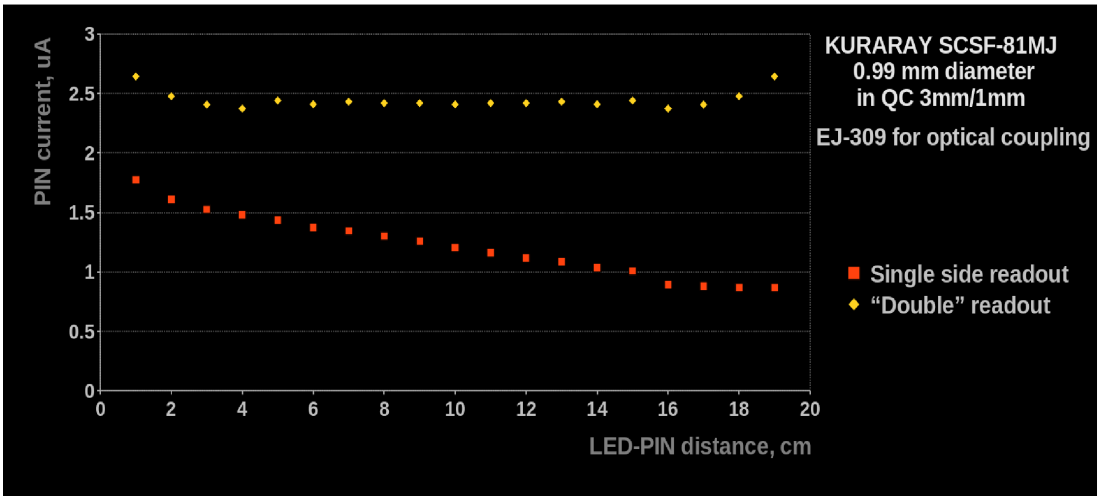

FIGURE 8.5: Light output (PIN diode currents, μA) as a function of distance between LED and PIN diode (in cm) for complex fibers with scintillating SCSF-81MJ core. Single-sided readout demonstates moderate attenuation. Double-sided readout offers signifficant compensation of this effect.

The plot for the non-irradiated fiber without the core (in yellow) stands out and demonstrates signifficantly higher light output. Therefore it might seem at first glance, that the use of a quartz capillary shell is an unnecessary complication of the design. However, one should keep in mind, that the light modes measured in this test differ from the ones measured by means of the quartz capillary shell: the light propagated in the shell was not trapped in the core as it escaped total internal reflection. Therefore it is not possible to compare the light outputs of the fibers with and without quartz shells. Instead, the results of degradation due to the irradiation has to be compared for both cases. Such a comparison shows that the light output for the bare Y11 fiber went down by at least a factor of three, and so did the photocurrent for the quartz-shell enclosed fiber. However, the irradiated complex fiber exibit less of the attenuation.

This result is an improvement already; however, it does not look satisfactory after the big expectations for the radiation hard complex fibers. This is a good chance to stop and re-think the mechanism of light propagation in such a complex fiber. Because there are several components involved, each possessing its own refractive index, the light propagation is more complex than in the case of ordinary fiber. As red-shifted light is emitted in the wavelength shifting fiber, depending on the direction it was emitted relative to the direction

of the fiber, there are different possibilities for its further propagation.

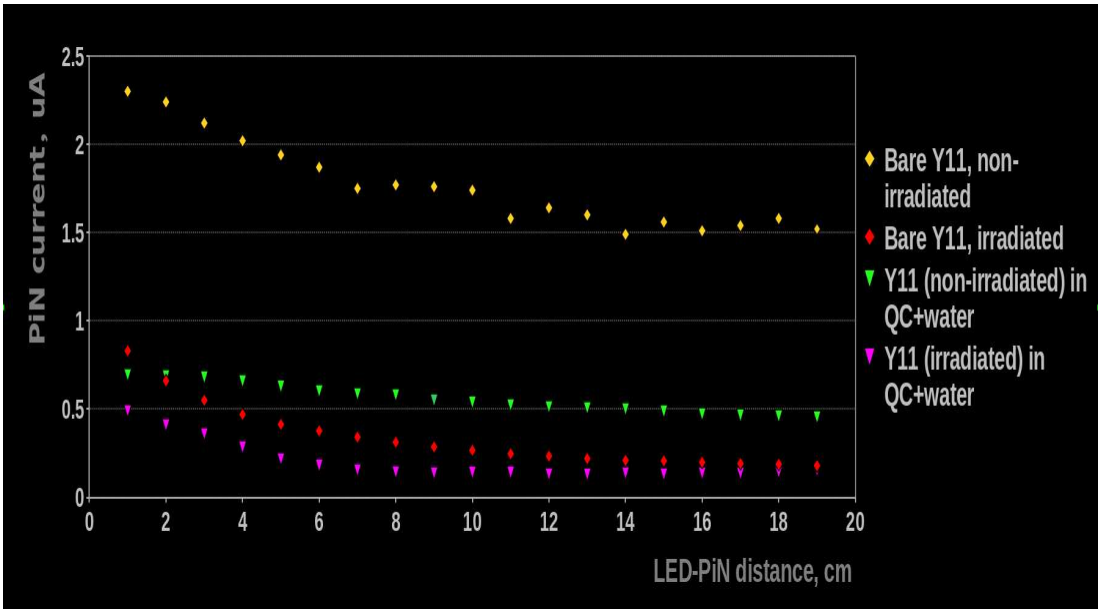

FIGURE 8.6: Light output (PIN diode current, μA) as a function of distance between the LED and PIN diode (in cm) for normal Y11 fibers and same fibers as a core of a complex fiber. The measurements are performend before irradiation and after irradiation with 40 Mrad of proton beam. See test for the discussion of result.

- The light was emitted in the cone close to the axis of the fiber. In this case the light will be trapped in the core, and will continue propagating along the fiber by means of total internal reflection in the fiber. As we do not plan to read out the signal from the light emitting core, this part of the re-emitted light is of a little value to us – this light will eventually be absorbed in the material of the fiber or escape through the non-readout end.

- The light was emitted almost perpendicular to the direction of the fiber. Such light will successfully penetrate through the cladding (or optical coupling substance or both) and the quartz shell and escape detection as well.

- The light was emitted in such a range, that it can escape the core, but undergoes total internal reflection on the boundary between the quartz capillary shell and outer environment. This light will bounce back and, following the laws of geometrical optics,

will make his way back into the light-emitting core. However, in the assumption that the transparancy of the core is highly degraded due to radiation damage, the probability of light attenuation in the core is very high. The solution can be in such a design of the fiber, that the light could undergo several internal reflections before hitting the core again. This can be achieved by

1. Increasing the ratio of quartz shell cross-section to light-emitting core cross-section to increase the fraction of light path in the quartz shell.
2. Off-centering the light-emitting core in the complex fiber to increase the number of reflections between penetrations of the core. It is also possible that the light will undergo total internal reflection on the boundary between the quartz capillary core and light emitting shell.

The proposed options are demonstrated in Fig. **8.7** in comparison with the design used for the studies above. As in the current design the light travels inside of the core material a significant fraction of time. It is not surprising that this design did not show dramatic improvement compared to normal fibers. The partial improvement however can be attributed to partial propagation in the shell, which does not attenuate the light that much. In the case of a relatively thin core off-centered in the quartz capillary shell, the light is capable of undergoing several acts of total internal reflection before penetrating the core. If the light guide with complex fiber is not too long, this might be sufficient to transport light to the photodetector without significant attenuation, as traversing the darkened core is the main source of attenuation.

8.8 Beam Tests in 2012

In 2012 during the fall beam test campaign a set of tests was performed with complex fibers with light-emitting cores. A small module formed by the brass absorber loaded with nine complex fibers was tested for a proof of concept. The complex fibers were based on the light-emitting cores made of ⌀0.99 mm SCSF-81MJ scintillating fibers. The

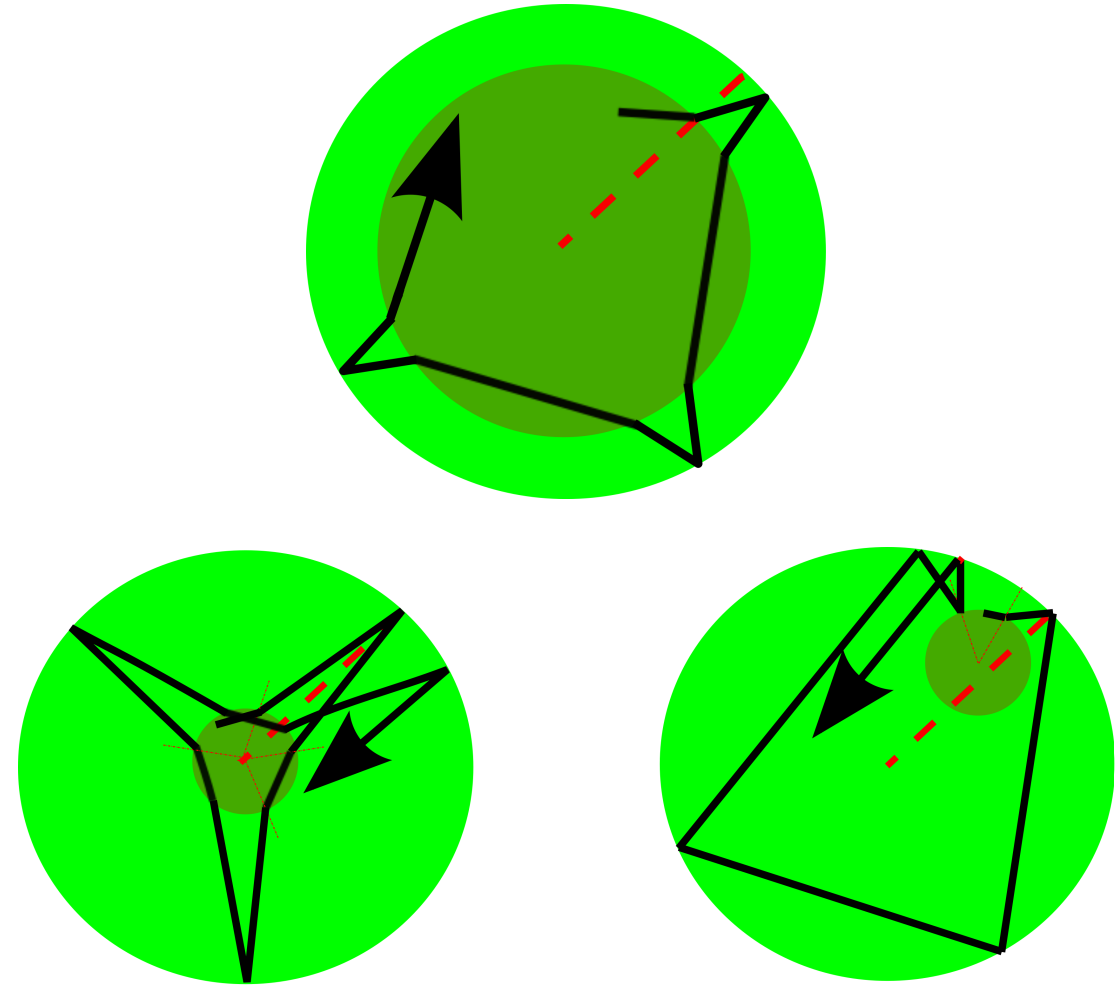

FIGURE 8.7: Cross-sectional view of the **TOP:** current design and **BOTTOM:** two improved designs of the quartz capillaries with light emitting cores. **LEFT:** Decrease in relative size of the light emitting core allows the light to travel a larger fraction of its path through the shell. **RIGHT:** Off-centered position of the light emitting core allows the light to undergo several acts of total internal reflection before penetrating the core.

light-transporting shells used were quartz capillaries: outer $\varnothing 3$ mm, inner $\varnothing 1$ mm. Optical coupling agent between the core and a shell was EJ-309 liquid scintillator. Therefore, light-emitting cores were also an active material for shower detection.

8.8.1 Geometry of the Module and DAQ

The volume of a brass absorber was shaped to reproduce the tapered geometry and size (approximately $3\times3\times22\,cm^3$) of a standard $PbWO_4$ crystal used in the endcap of the elec-

tromagnetic calorimeter of the CMS experiment. In this brass element, 9 complex fibers were inserted into holes of 4 mm diameter and supported at the ends with thin brass washers to prevent contact between the light-transporting shell and the wall of the absorber block in unwanted locations (Fig. **8.8**). The scintillating fibers of the core had mirrors at the ends to avoid direct light transmission from the cores to the optical readout.

The prototype has been tested in the H2 test beam line at the Super Proton Synchrotron (SPS) at CERN. The detailed description of this experimental facility is presented in the relevant section. The module was inserted in the center of a 3×3 matrix of $PbWO_4$ crystals of the ECAL module, very much like the LuAG-based module, described in the previous chapter (Fig. **7.3**, top). The $PbWO_4$ crystals were calibrated in the previous tests of ECAL and their signals were used for centering of the beam on the complex fiber module. An example of the signals from the $PbWO_4$ for a 50 GeV electron beam are shown in Fig. **8.9**. The similar outputs in all channels surrounding the complex fiber module demonstrate proper centering of the beam spot on the module.

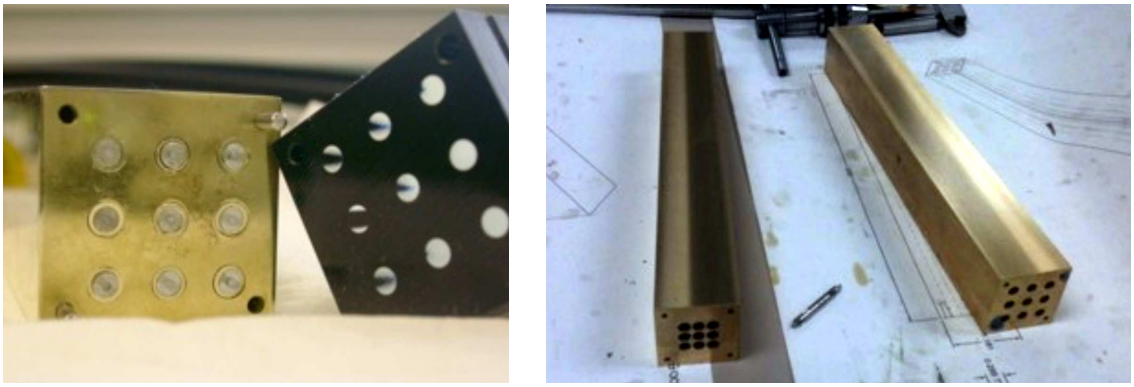

FIGURE 8.8: Tapered brass absorber for the beam tests of complex fibers with light-emitting cores. **LEFT:** Front view of the absorber loaded with the complex fibers. **RIGHT:** Overall view of the absorber prototypes. The one used for the complex fibers beam tests is shown on the right.

For the light extraction, each extremity of the complex fiber module was coupled with Silicon grease (Rhodorsil Paste 7) to 9 clear optical fibers (Fig. **7.3**, bottom left) which then transported the analog signal to silicon photomultipliers, SiPM (Fig. **7.3** on page 118, bottom right). The readout system and data acquisition system in this case are the same as for the mini-CFcal module, as described in detail in section **7.3**.

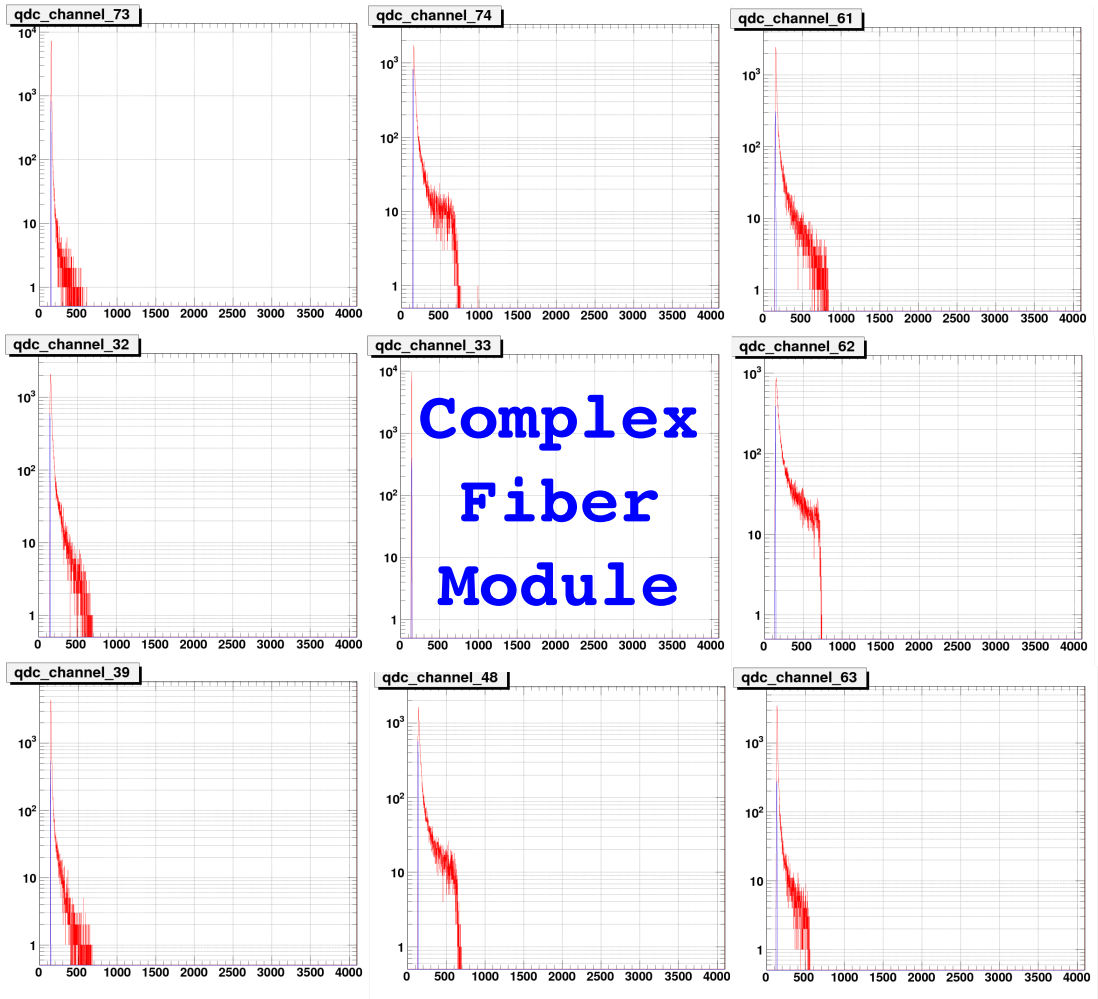

FIGURE 8.9: Signals in the $PbWO_4$ crystals surrounding the complex fiber module validate the proper centering of the beam on the module.

8.8.2 Pulse Shapes and Signal-Pedestal Separation

As it was explained in section 7.4, two wire chambers located upstream from the setup were used to reconstruct hit positions on the module and study the response of the LuAG fibers as a function of such. However, at the time of data accumulation with the complex fiber module the hit information from the upstream wire chamber WCA was unavailable. As a result, such comprehensive study of the complex fiber response is not possible with the data currently available, as the data from a single wire chamber in front of the module does not allow to reconstruct the particle hit position on the complex fiber module.

Instead, the available data is used to demonstrate the timing characteristics of the com-

plex fiber signals and that it is possible to separate the signals of showering particles from the pedestals.

First of all, the reconstructed pulse shapes of the signal (Fig. **8.10**) demonstrate its rather fast decay – most of the signal is deposited within two time slices.

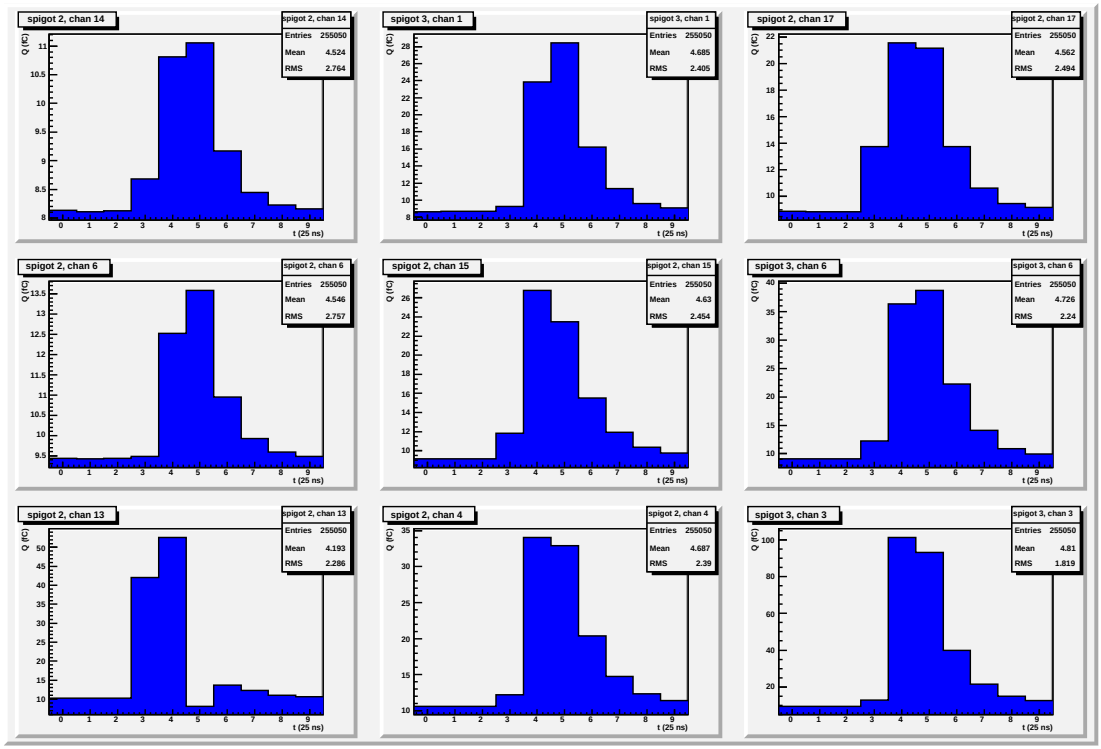

FIGURE 8.10: Pulse shapes from the readout face of the complex fiber module. Binning is governed by the standard LHC clock with 25 ns timeslices. Most of the signal is deposited within two timeslices.

The presented histograms show the integral pulse shape of all the events in the run. However, the question on the possibility to discriminate between the pedestal and signal events on an event-by-event basis remains open. With no access to the information from the second wire chamber, the following approach can shed light on it.

For each event let us integrate the charge produced by each of the readout channels of the module in the entire sampling window. The 2-dimentional histograms of the integrated charge versus hit position in the available wire chamber are shown in Fig. **8.11**. It is clear from those plots, that most of the events produce fairly low signals (if the particle hits the module far from a particular channel, then only the tails of the shower reaches the

channel). Events of this type form a dense cloud along the spatial axis. There are however events producing high signals – those correspond to particles penetrating the module in close proximity of the complex fibers.

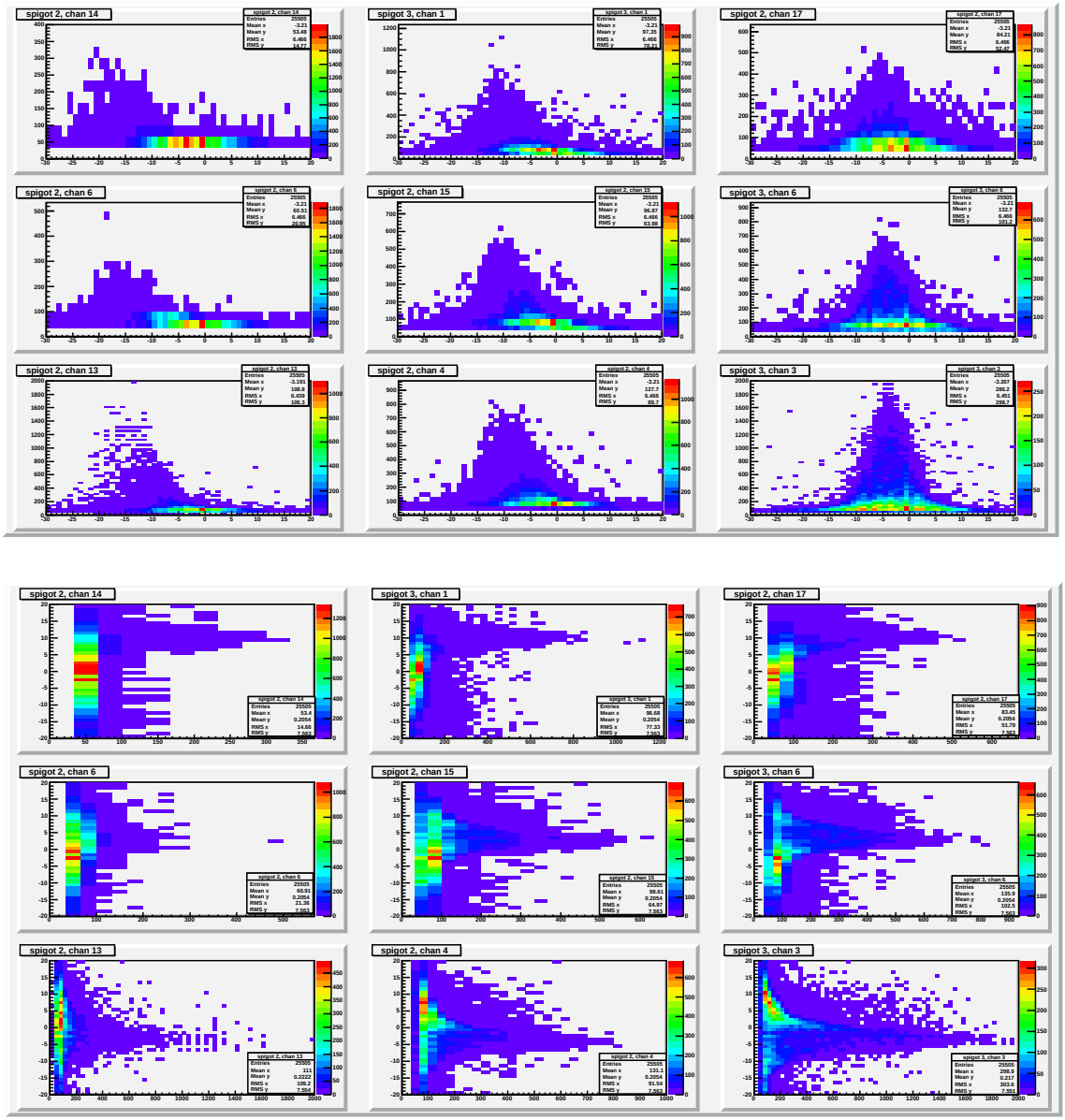

FIGURE 8.11: 2D histograms with integrated signal in the channel versus corresponding hit position in the wire chamber. **TOP:** For hits in the horizontal direction. Horizontal axis corresponds to the wire chamber hits. **BOTTOM:** For hits in the vertical direction. Vertical axis corresponds to the wire chamber hits.

Now those 2D-histograms can be used to produce profile 1D-histograms: for each spa-

tial bin its content is a ”center of mass” of the distribution in the corresponding band of a 2D-histogram, and the error bars are calculated accordingly. An example of such profiles for the horizontal hits in the wire chamber is shown in Fig. **8.12**. As the largest signals are produced by the particles directly hitting the fibers, the maximum of the fitted peak in the profile histograms gives the best estimate for the fiber position. This is in a sense the fiber position measurement in the wire chamber reference frame. Now the results of the fit can be used to select the particles penetrating the module close to the fiber. As an example, Fig. **8.13** demonstrates the signals produced in all front-face read-out channels of the module by particles which produced hits in a wire chamber within a circle $\varnothing 4\,\mathrm{mm}$ centered around the peak position. The green plot for selected events demonstrated much better discrimination from pedestal events than a non-biased sample, which makes it possible to conclude that the tested module based on complex fibers with light emitting cores is capable of discriminating penetrating particles from pedestal events on an event-by-event basis.

8.9 Perspectives and Outlook

The preliminary studies of various complex fibers with light-emitting cores, including those with liquid cores, were conducted to establish the basic principles of operation and limitations. The results of tests confirmed the potential of complex fibers for the readout systems of calorimeters. The importance of proper decontamination of the surface of light-transporting shells as well as homogeneity of the optical coupling agent was demonstrated. Irradiation of the cores based on Y11 wavelength shifter was performed to study the potential for radiation-hard readout. Some improvement compared to conventional fibers was demonstrated. A few improvements of the design of complex fibers were proposed. The beam tests of a complex fiber-based module were conducted, where the light-emitting core of the fibers were serving as an active material of a sampling calorimeter prototype. Promptly decaying pulse shapes confirm the potential of this kind of design for calorimetry. Despite the lack of data from one of the accompanying wire chambers, reasonable discrimination between signal and pedestal events on an event-by-event basis was confirmed.

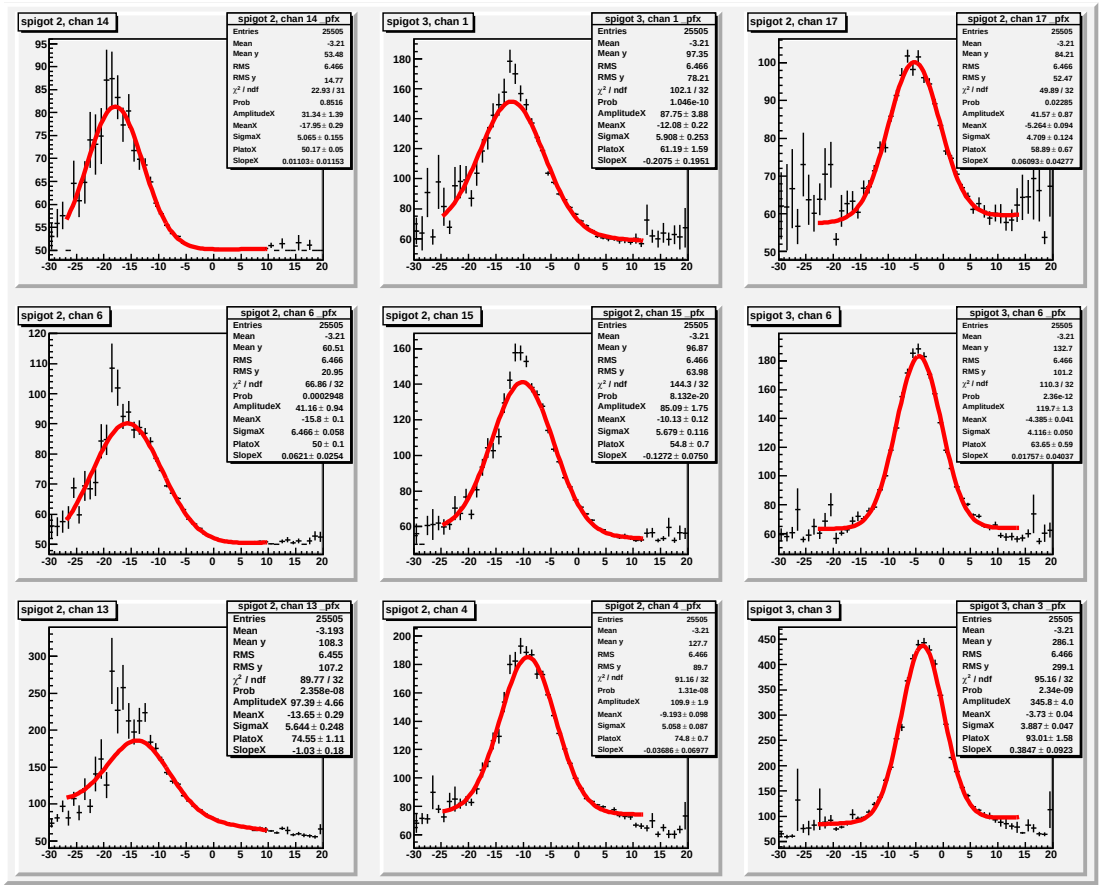

FIGURE 8.12: Spatial profiles of the 2-dimensional histograms of Fig. **8.11**, top. The value of the peak position gives a good estimate of the fiber position.

The perspectives for further studies in this direction include varying the geometrical design of the complex fibers. As it was pointed out above, minimizing the fraction of the cross section occupied by the core, as well as off-centering of the core can improve the attenuation characteristics. The latter besides can improve the light output, provided the off-centered core is located closer to the source of scintillating light (see Fig. **8.14**).

The candidates for such light-transporting shells are available on the market from various manufacturers of fused silica glasses. As an example, see Fig. **8.15**, which was taken from the web site of one of the US manufacturers, Technical Glass Products[61] and represents a small variety of the configurations available off the shelf.

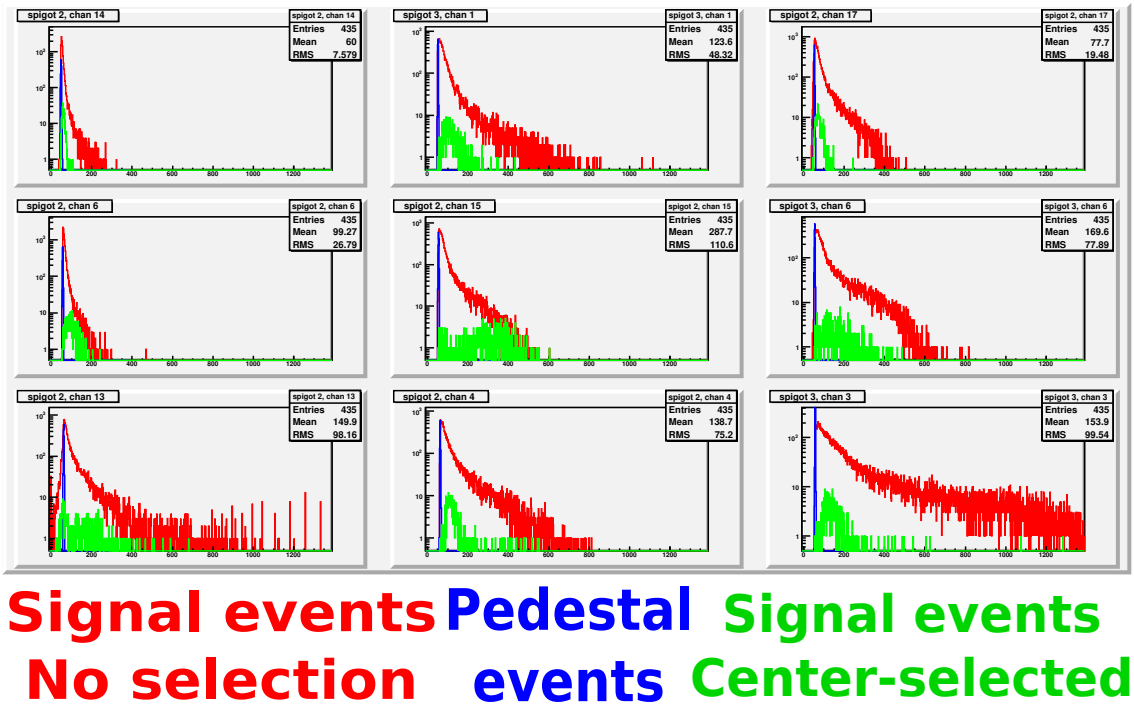

FIGURE 8.13: Integrated signals from the front-face read-out of the complex fiber module. The events selected in a ⌀4 mm spot around the peak maximum from the spatial profile fit of the central fiber (in green). For comparison, the events without any selection are shown in red. The outputs for pedestal events are shown in blue.

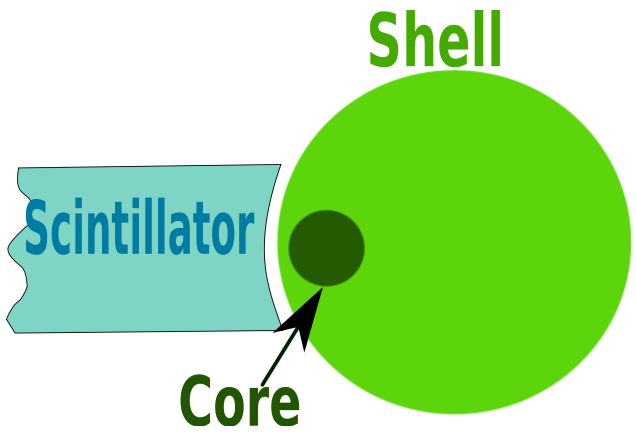

FIGURE 8.14: Sketch of a design for light collection by means of complex fibers with off-centered light-emitting core.

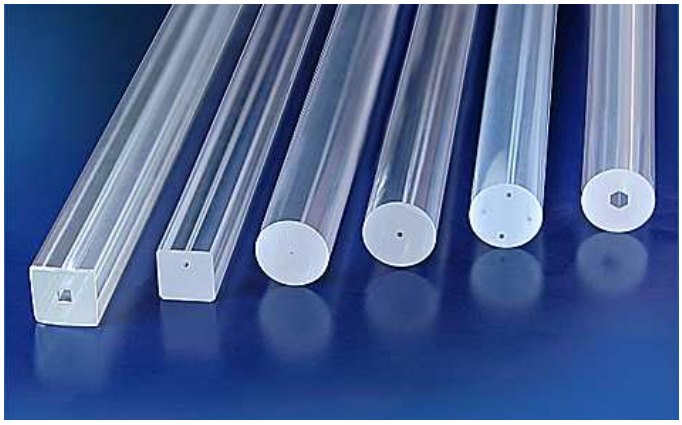

FIGURE 8.15: A variety of precision bore tubing, produced by Technical Glass Products. The picture is taken from [61].

Chapter 9

Beam Tests at FNAL

This chapter does not contain any analysis and rather presents a description of the calorimetric prototype tested in 2014 at the Fermilab test beam facility with an electron beam of up to $32\,\mathrm{GeV}$. It hence rather introduces a direction for the future studies in the field of high-granularity radiation-hard calorimetry.

In accord with the "Geometry B", discussed at the end of the section dedicated to LuAG based mini-CFcal module, the main goal of the beam test in 2014 was exploring the performance of a calorimetric module with transverse orientation of crystal fibers relative to the direction of the beam. The particular spacing of fibers however was slightly different, following the results of GEANT4 simulations for the optimal geometry.

Based on the considerations of convenience of manufacturing, the absorber of the module was formed by a set of brass plates. When fully assembled, it represents a brick of $25.5\,cm \times 16.5\,cm \times 6.5\,cm$ with eight "layers" of cylindrical holes which go all the way through the absorber in the direction of its longest dimension (Fig **9.1**). In each of the layers the adjacent holes have $4\,mm$ spacing between their centers. There are $1.6\,cm$ spacing

in between the planes of the adjacent layers.

In addition, even layers are displaced relative to the odd layers, such that the fibers' locations appear in checkerboard order (Fig. **9.2**, top).

With eight layers of crystal fibers and eight fibers per layer this CFcal module thus has a total of 64 fibers. Both Cherenkov and scintillating fibers are used: the Cherenkov fibers occupy the fourth layer (as seen by the beam), while the rest of the fibers are scintillating.

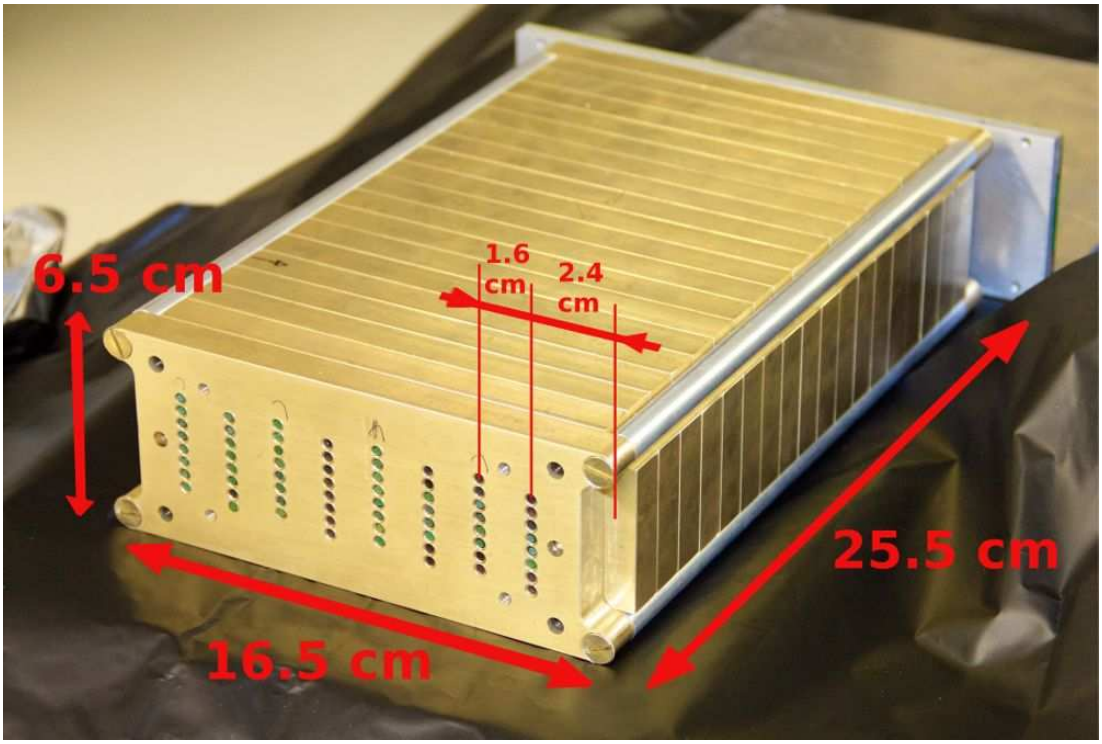

FIGURE 9.1: Absorber assembly for the test beam of CFcal at FNAL in 2014.

The LuAG crystals are wrapped with protective Teflon tape and fed into the brass tubes, which in turn are inserted into the module. The material of the tubes contributes to the absorber. The inner diameter of the tubes is $3\,mm$. One end of each crystal is directly coupled to one of the photodetectors in the SiPM array (Fig. **9.2**, bottom) with optical grease, and the signals from the photodetectors are further handled with the PADE boards, which read out the signal in time slices of $13\,ns$. Hence, each of the 64 crystal fibers is read out separately. The opposite ends of the fibers are used for light injection from the LED pulser for cross-checks and calibration purposes (Fig. **9.3**).

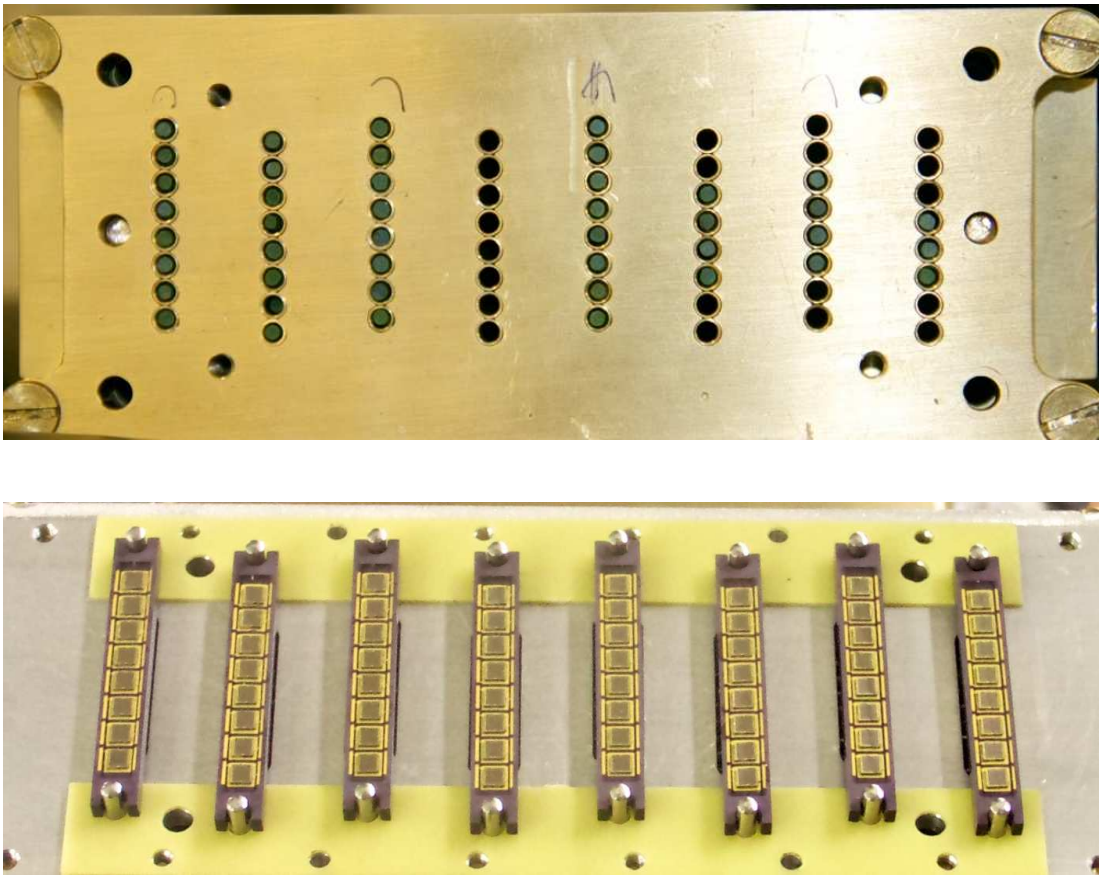

FIGURE 9.2: **TOP:** Side plate of the absorber used for the test beam of CFcal at FNAL in 2014. Some of the LuAG fibers are already loaded into the absorber, and their ends are seen in the holes. **BOTTOM:** SiPM photo detectors are assembled on the plate of matching geometry and couple directly to the fiber ends.

To account for the fact that the electromagnetic shower isn't fully contained in the module of this longitudial size, a tail catcher was used in the setup. A matrix of 3×3 crystals of BaF_2 each measuring $3\times4\times25cm^3$ was positioned behind the CFcal module and read out with PMTs. As the radiation length in BaF_2 crystals is about 2.05 cm, the tail catcher alone provides about 12 radiation lengths of material, which should be enough for complete longitudial containment of the electromagnetic showers.

The readout used in this test beam is much simpler than the one used in the previous test beams, as the photodetectors are basically integrated into the module. This reflects the important properties of the photodetectors used, the SiPMs. First of all, they are relatively radiation hard, and hence do not have to be specifically shielded. Secondly, bias voltage

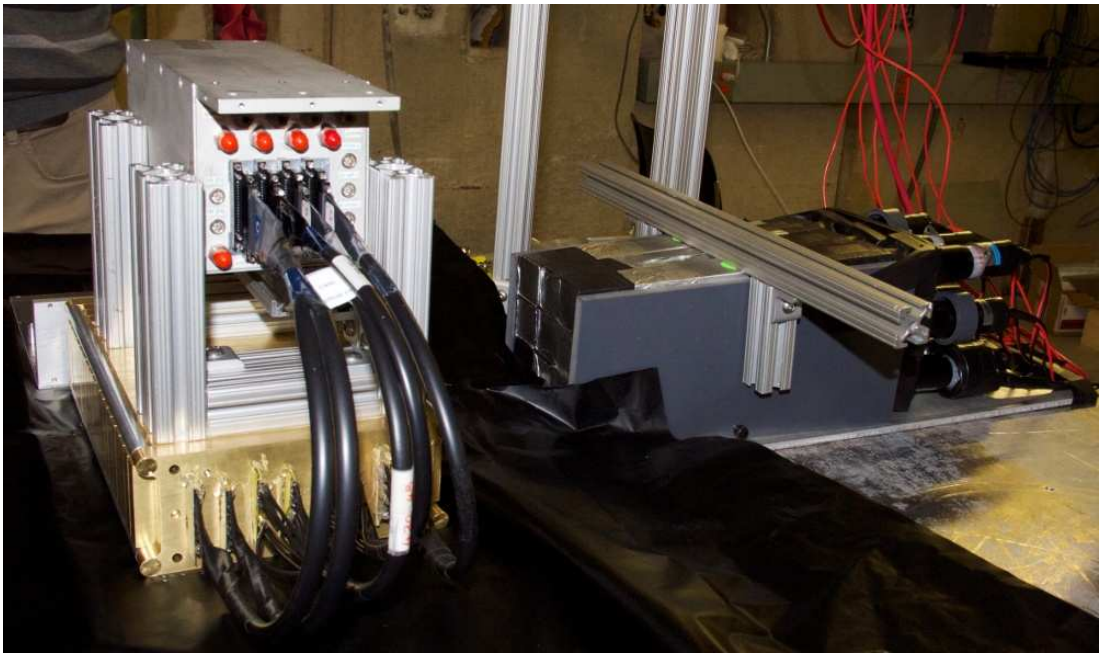

FIGURE 9.3: The entire setup as seen from the light injection side. The beam is coming from the left-hand side and travels horizontally. The brass absorber at the bottom left is loaded with LuAG crystals, the LED pulser on top of it provides the calibration signals. BaF_2 crystals on the right measure the leakage of the shower behind the CFcal module.

and gain of the SiPMs are temperature dependent. Therefore a mechanism which sustains a fixed temperature of the photodetectors is required. However, if the SiPMs are directly coupled to the sufficient thermal mass, such as absorber, the fixed temperature is maintained automatically.

The readout based on the complex fibers (as discussed in the previous chapter) was also tested with this module: a horizontal quartz capillary with a wavelength shifting core made of O-2 from KURARAY was introduced at the end of the LuAG crystals and collected light from all odd or all even layers. Preliminary results confirm that this readout is operational.

Appendices

Appendix A

Search Region Datasets and Triggers

Datasets:	**Triggers:**	**L (fb^{-1})**
/MET/Run2012A-13Jul2012-v1/AOD	HLT_DiCentralPFJet50_PFMET80_v*	0.808
/MET/Run2012A-recover-06Aug2012-v1/AOD	HLT_DiCentralPFJet50_PFMET80_v*	0.082
/MET/Run2012B-13Jul2012-v1/AOD	HLT_DiCentralPFJet50_PFMET80_v*	4.428
/MET/Run2012C-24Aug2012-v1/AOD	HLT_DiCentralPFNoPUJet50_PFMETORPFMETNoMu80_v*	0.495
/MET/Run2012C-PromptReco-v2/AOD	HLT_DiCentralPFNoPUJet50_PFMETORPFMETNoMu80_v*	6.397
/MET/Run2012C-EcalRecover_11Dec2012-v1/AOD	HLT_DiCentralPFNoPUJet50_PFMETORPFMETNoMu80_v*	0.134
/MET/Run2012D-PromptReco-v1/AOD	HLT_DiCentralPFNoPUJet50_PFMETORPFMETNoMu80_v*	6.689
Total Luminosity:		**19.034**

TABLE A.1: Overview of the search region datasets.

Appendix B

Other Data Samples

Datasets:	**L (fb^{-1})**
/SingleElectron/Run2012A-13Jul2012-v1/AOD	0.808
/SingleElectron/Run2012A-recover-06Aug2012-v1/AOD	0.082
/SingleElectron/Run2012B-13Jul2012-v1/AOD	4.428
/SingleElectron/Run2012C-24Aug2012-v1/AOD	0.495
/SingleElectron/Run2012C-PromptReco-v2/AOD	6.397
/SingleElectron/Run2012C-EcalRecover_11Dec2012-v1/AOD	0.134
/SingleElectron/Run2012D-PromptReco-v1/AOD	6.689
Total Luminosity:	**19.034**

TABLE B.1: Overview of the single electron datasets, collected with the trigger: **HLT_Ele27_WP80_v***.

Datasets:	**L (fb^{-1})**
/SingleMu/Run2012A-13Jul2012-v1/AOD	0.808
/SingleMu/Run2012A-recover-06Aug2012-v1/AOD	0.082
/SingleMu/Run2012B-13Jul2012-v1/AOD	4.428
/SingleMu/Run2012C-24Aug2012-v1/AOD	0.495
/SingleMu/Run2012C-PromptReco-v2/AOD	6.397
/SingleMu/Run2012C-EcalRecover_11Dec2012-v1/AOD	0.134
/SingleMu/Run2012D-PromptReco-v1/AOD	6.689
Total Luminosity:	**19.034**

TABLE B.2: Overview of the single muon datasets, collected with the trigger: **HLT_IsoMu24_eta2p1_v***.

Datasets:
/HT/Run2012A-13Jul2012-v1/AOD
/HT/Run2012A-recover-06Aug2012-v1/AOD
/JetHT/Run2012B-13Jul2012-v1/AOD
/JetHT/Run2012C-24Aug2012-v1/AOD
/JetHT/Run2012C-PromptReco-v2/AOD
/JetHT/Run2012C-EcalRecover_11Dec2012-v1/AOD
/JetHT/Run2012D-PromptReco-v1/AOD

TABLE B.3: Overview of the H_T datasets, collected with the prescaled triggers (hence no luminosity is listed).

Datasets e+e
/DoubleElectron/Run2012A-13Jul2012-v1/AOD
/DoubleElectron/Run2012A-recover-06Aug2012-v1/AOD
/DoubleElectron/Run2012B-13Jul2012-v1/AOD
/DoubleElectron/Run2012C-24Aug2012-v1/AOD
/DoubleElectron/Run2012C-PromptReco-v2/AOD
/DoubleElectron/Run2012C-EcalRecover_11Dec2012-v1/AOD
/DoubleElectron/Run2012D-PromptReco-v1/AOD
Datasets $\mu + \mu$
/DoubleMu/Run2012A-13Jul2012-v1/AOD
/DoubleMu/Run2012A-recover-06Aug2012-v1/AOD
/DoubleMu/Run2012B-13Jul2012-v1/AOD
/DoubleMu/Run2012C-24Aug2012-v1/AOD
/DoubleMu/Run2012C-PromptReco-v2/AOD
/DoubleMu/Run2012C-EcalRecover_11Dec2012-v1/AOD
/DoubleMu/Run2012D-PromptReco-v1/AOD
Datasets $\mu + (\gamma$ or e)
/MuEG/Run2012A-13Jul2012-v1/AOD
/MuEG/Run2012A-recover-06Aug2012-v1/AOD
/MuEG/Run2012B-13Jul2012-v1/AOD
/MuEG/Run2012C-24Aug2012-v1/AOD
/MuEG/Run2012C-PromptReco-v2/AOD
/MuEG/Run2012C-EcalRecover_11Dec2012-v1/AOD
/MuEG/Run2012D-PromptReco-v1/AOD

TABLE B.4: Overview of the datasets for triple lepton control regions.

Trigger:	**Leptons**	**L (fb^{-1})**
/HLT_Ele17_CaloIdT_CaloIsoVL_TrkIdVL_TrkIsoVL_Ele8$\cdots$ $\cdots$_CaloIdT_CaloIsoVL_TrkIdVL_TrkIsoVL	eee	19.034
/HLT_Mu17_Ele8_CaloIdT_CaloIsoVL_TrkIdVL_TrkIsoVL	eeμ, $\mu\mu$e	19.034
/HLT_Mu8_Ele17_CaloIdT_CaloIsoVL_TrkIdVL_TrkIsoVL	eeμ, $\mu\mu$e	19.034
/HLT_Mu17_Mu8	$\mu\mu\mu$	19.034

TABLE B.5: Luminosity for each of the triggers for the triple lepton control region.

Appendix C

Monte Carlo

Datasets:	Cross Section (pb)	# of Events, $\times 10^6$
/ZJetsToNuNu_50_HT_100_TuneZ2Star_8TeV_madgraph/Summer12_DR53X-PU_S10_START53_V7A-v1/AODSIM		
/ZJetsToNuNu_50_HT_100_TuneZ2Star_8TeV_madgraph/Summer12_DR53X-PU_S10_START53_V7A-v1/AODSIM	449.8	24.
/ZJetsToNuNu_100_HT_200_TuneZ2Star_8TeV_madgraph/Summer12_DR53X-PU_S10_START53_V7A-v1/AODSIM		
/ZJetsToNuNu_100_HT_200_TuneZ2Star_8TeV_madgraph_ext/Summer12_DR53X-PU_S10_START53_V7A-v1/AODSIM	189.7	10.
/ZJetsToNuNu_200_HT_400_TuneZ2Star_8TeV_madgraph/Summer12_DR53X-PU_S10_START53_V7A-v1/AODSIM		
/ZJetsToNuNu_200_HT_400_TuneZ2Star_8TeV_madgraph_ext/Summer12_DR53X-PU_S10_START53_V7A-v1/AODSIM	46.1	9.7
/ZJetsToNuNu_400_HT_inf_TuneZ2Star_8TeV_madgraph/Summer12_DR53X-PU_S10_START53_V7A-v1/AODSIM		
/ZJetsToNuNu_400_HT_inf_TuneZ2Star_8TeV_madgraph_ext/Summer12_DR53X-PU_S10_START53_V7A-v1/AODSIM	6.398	5.1
/DYJetsToLL_HT_200To400_TuneZ2Star_8TeV_madgraph/Summer12_DR53X-PU_S10_START53_V7A-v1/AODSIM		
/DYJetsToLL_HT_200To400_TuneZ2Star_8TeV_madgraph_ext/Summer12_DR53X-PU_S10_START53_V7A-v1/AODSIM	24.14	6.9
/DYJetsToLL_HT_400ToInf_TuneZ2Star_8TeV_madgraph/Summer12_DR53X-PU_S10_START53_V7A-v1/AODSIM		
/DYJetsToLL_HT_400ToInf_TuneZ2Star_8TeV_madgraph_ext/Summer12_DR53X-PU_S10_START53_V7A-v1/AODSIM	3.361	2.7
/DY1JetsToLL_M-50_TuneZ2Star_8TeV_madgraph/Summer12_DR53X-PU_S10_START53_V7A-v1/AODSIM	722	25
/DY1JetsToLL_M-50_TuneZ2Star_8TeV_madgraph/Summer12_DR53X-PU_S10_START53_V7A-v1/AODSIM	722	25
/DY2JetsToLL_M-50_TuneZ2Star_8TeV_madgraph/Summer12_DR53X-PU_S10_START53_V7A-v1/AODSIM	219	22
/DY2JetsToLL_M-50_TuneZ2Star_8TeV_madgraph/Summer12_DR53X-PU_S10_START53_V7A-v1/AODSIM	219	22
/DY3JetsToLL_M-50_TuneZ2Star_8TeV_madgraph/Summer12_DR53X-PU_S10_START53_V7A-v1/AODSIM	65.7	11
/DY3JetsToLL_M-50_TuneZ2Star_8TeV_madgraph/Summer12_DR53X-PU_S10_START53_V7A-v1/AODSIM	65.7	11
/DY4JetsToLL_M-50_TuneZ2Star_8TeV_madgraph/Summer12_DR53X-PU_S10_START53_V7A-v1/AODSIM	27.27	6.4
/DY4JetsToLL_M-50_TuneZ2Star_8TeV_madgraph/Summer12_DR53X-PU_S10_START53_V7A-v1/AODSIM	27.27	6.4

TABLE C.1: Overview of the datasets for $Z \longrightarrow \nu\overline{\nu}$ and $Z \longrightarrow l^+l^-$ MC.

Datasets:	**Cross Section (pb)**	**# of Events,** $\times 10^6$
/QCD_HT-250To500_TuneZ2Star_8TeV-madgraph-pythia6/Summer12_DR53X-PU_S10_START53_V7A-v1/AODSIM	282×10^3	27
/QCD_HT-500To1000_TuneZ2Star_8TeV-madgraph-pythia6/Summer12_DR53X-PU_S10_START53_V7A-v1/AODSIM	8.63×10^3	31
/QCD_HT-1000ToInf_TuneZ2Star_8TeV-madgraph-pythia6/Summer12_DR53X-PU_S10_START53_V7A-v1/AODSIM	213	14
/QCD_Pt-50To80_TuneZ2Star_8TeV_pythia6/Summer12_DR53X-PU_S10_START53_V7A-v2/AODSIM	8.11×10^6	6.0
/QCD_Pt-80To120_TuneZ2Star_8TeV_pythia6/Summer12_DR53X-PU_S10_START53_V7A-v3/AODSIM	1.03×10^6	6.0
/QCD_Pt-120To170_TuneZ2Star_8TeV_pythia6/Summer12_DR53X-PU_S10_START53_V7A-v3/AODSIM	156×10^3	6.0
/QCD_Pt-170To300_TuneZ2Star_8TeV_pythia6/Summer12_DR53X-PU_S10_START53_V7A-v2/AODSIM /QCD_Pt-170To300_TuneZ2Star_8TeV_pythia6_v2/Summer12_DR53X-PU_S10_START53_V7A-v1/AODSIM	34.4×10^3	26
/QCD_Pt-300To470_TuneZ2Star_8TeV_pythia6/Summer12_DR53X-PU_S10_START53_V7A-v2/AODSIM /QCD_Pt-300To470_TuneZ2Star_8TeV_pythia6_v2/Summer12_DR53X-PU_S10_START53_V7A-v1/AODSIM /QCD_Pt-300To470_TuneZ2Star_8TeV_pythia6_v3/Summer12_DR53X-PU_S10_START53_V7A-v1/AODSIM	1.71×10^3	29
/QCD_Pt-470To600_TuneZ2Star_8TeV_pythia6/Summer12_DR53X-PU_S10_START53_V7A-v2/AODSIM	113	4.0
/QCD_Pt-600To800_TuneZ2Star_8TeV_pythia6/Summer12_DR53X-PU_S10_START53_V7A-v2/AODSIM	27.0	4.0
/QCD_Pt-800To1000_TuneZ2Star_8TeV_pythia6/Summer12_DR53X-PU_S10_START53_V7A-v2/AODSIM	3.53	4.0
/QCD_Pt-1000To1400_TuneZ2Star_8TeV_pythia6/Summer12_DR53X-PU_S10_START53_V7A-v1/AODSIM	0.736	4.0
/QCD_Pt-1400To1800_TuneZ2Star_8TeV_pythia6/Summer12_DR53X-PU_S10_START53_V7A-v1/AODSIM	34×10^{-3}	2.0
/QCD_Pt-1800_TuneZ2Star_8TeV_pythia6/Summer12_DR53X-PU_S10_START53_V7A-v1/AODSIM	1.85×10^{-3}	0.98

TABLE C.2: Overview of the datasets for the QCD MC.

Datasets:	Cross Section (pb)	# of Events, $\times 10^3$
/TTZJets_8TeV-madgraph_v2/Summer12_DR53X-PU_S10_START53_V7A-v1/AODSIM	0.206	210
/ttbarZ_8TeV-Madspin_aMCatNLO-herwig/Summer12_DR53X-PU_S10_START53_V19A-v1/AODSIM	0.206	140

TABLE C.3: Overview of the datasets for the $t\bar{t}Z$ MC.

Datasets:	Cross Section (pb)	# of Events, $\times 10^6$
/W1JetasToLNu_TuneZ2Star_8TeV-madgraph/Summer12_DR53X-PU_S10_START53_V7A-v1/AODSIM	8.17×10^3	23
/W2JetasToLNu_TuneZ2Star_8TeV-madgraph/Summer12_DR53X-PU_S10_START53_V7A-v1/AODSIM	2.65×10^3	33
/W3JetasToLNu_TuneZ2Star_8TeV-madgraph/Summer12_DR53X-PU_S10_START53_V7A-v1/AODSIM	785	16
/W4JetasToLNu_TuneZ2Star_8TeV-madgraph/Summer12_DR53X-PU_S10_START53_V7A-v1/AODSIM	324	13

TABLE C.4: Overview of the datasets for the W MC.

Datasets:	Cross Section (pb)	# of Events, $\times 10^6$
/WWJetsTo2L2Nu_TuneZ2Star_8TeV-madgraph/Summer12_DR53X-PU_S10_START53_V7A-v1/AODSIM	5.82	1.9
/WZJetsTo2L2Q_TuneZ2Star_8TeV-madgraph/Summer12_DR53X-PU_S10_START53_V7A-v1/AODSIM	2.46	3.2
/WZJetsTo3LNu_TuneZ2Star_8TeV-madgraph/Summer12_DR53X-PU_S10_START53_V7A-v1/AODSIM	1.19	2.0
/ZZJetsTo2L2Nu_TuneZ2Star_8TeV-madgraph/Summer12_DR53X-PU_S10_START53_V7A-v1/AODSIM	0.388	0.95
/ZZJetsTo2L2Q_TuneZ2Star_8TeV-madgraph/Summer12_DR53X-PU_S10_START53_V7A-v1/AODSIM	1.34	1.9
/ZZJetsTo4L_TuneZ2Star_8TeV-madgraph/Summer12_DR53X-PU_S10_START53_V7A-v1/AODSIM	0.213	4.8

TABLE C.5: Overview of the datasets for the WW, WZ, ZZ MC.

Datasets:	**Cross Section (pb)**	**# of Events,** $\times 10^6$
/TTJets_MassiveBinDACAY_TuneZ2Star_8TeV-madgraph-tauola/Summer12_DR53X-PU_S10_START53_V7A-v1/AODSIM		
/TTJets_MassiveBinDACAY_TuneZ2Star_8TeV-madgraph-tauola/Summer12_DR53X-PU_S10_START53_V7A-v2/AODSIM	234	6.9
/TT_CT10_TuneZ2Star_8TeV-powheg-tauola/Summer12_DR53X-PU_S10_START53_V7A-v1/AODSIM		
/TT_CT10_TuneZ2Star_8TeV-powheg-tauola/Summer12_DR53X-PU_S10_START53_V7A-v2/AODSIM	234	28
/TT_CT10_AUET2_8TeV-powheg-herwig/Summer12_DR53X-PU_S10_START53_V7A-v1/AODSIM	234	22
/TTJets_SemiLeptMGDecays_8TeV-madgraph/Summer12_DR53X-PU_S10_START53_V7A_ext-v1/AODSIM		

TABLE C.6: Overview of the datasets for the $t\bar{t}$ MC.

Datasets:	**Cross Section (pb)**	**# of Events,** $\times 10^6$
/T_t-channel_TuneZ2Star_8TeV-powheg-tauola/Summer12_DR53X-PU_S10_START53_V7A-v1/AODSIM	56.4	3.8
/Tbar_t-channel_TuneZ2Star_8TeV-powheg-tauola/Summer12_DR53X-PU_S10_START53_V7A-v1/AODSIM	30.7	1.9
/TToDilepton_tW-channel-DR_8TeV-powheg-tauola/Summer12_DR53X-PU_S10_START53_V7A-v1/AODSIM	1.18	3.0
/TbarToDilepton_tW-channel-DR_8TeV-powheg-tauola/Summer12_DR53X-PU_S10_START53_V7A-v1/AODSIM	1.18	3.0

TABLE C.7: Overview of the datasets for the single top MC.

Datasets:	**Cross Section (pb)**	**# of Events,** $\times 10^3$
/TTWJets_8TeV-madgraph/Summer12_DR53X-PU_S10_START53_V7A-v1/AODSIM	0.232	190

TABLE C.8: Dataset for the $t\bar{t}W$ MC.

Datasets:
/SMS-8TeV-Pythia6Z_T2tt_mStop-150to475_mLSP-1/Summer12-START52_V9_FSIM-v1/AODSIM
/SMS-8TeV-Pythia6Z_T2tt_mStop-500to800_mLSP-1/Summer12-START52_V9_FSIM-v1/AODSIM
/SMS-T2tt_mStop-150to350_mLSP-0to250_8TeV-Pythia6Z/Summer12-START52_V9_FSIM-v1/AODSIM
/SMS-T2tt_mStop-375to475_mLSP-0to375_8TeV-Pythia6Z/Summer12-START52_V9_FSIM-v1/AODSIM
/SMS-T2tt_mStop-500to650_mLSP-0to225_8TeV-Pythia6Z/Summer12-START52_V9_FSIM-v1/AODSIM
/SMS-T2tt_mStop-500to650_mLSP-250to550_8TeV-Pythia6Z/Summer12-START52_V9_FSIM-v1/AODSIM
/SMS-T2tt_mStop-675to800_mLSP-0to275_8TeV-Pythia6Z/Summer12-START52_V9_FSIM-v1/AODSIM
/SMS-T2tt_2J_mStop-750_mLSP-25_TuneZ2star_8TeV-madgraph-tauola/Summer12_DR53X-PU_S10_START53_V7C-v1/AODSIM
/SMS-T2tt_2J_mStop-500_mLSP-300_TuneZ2star_8TeV-madgraph-tauola/Summer12_DR53X-PU_S10_START53_V7C-v1/AODSIM
/SMS-T2tt_2J_mStop-600_mLSP-50_TuneZ2star_8TeV-madgraph-tauola/Summer12_DR53X-PU_S10_START53_V7C-v1/AODSIM
/SMS-T2tt_2J_mStop-400_mLSP-150_TuneZ2star_8TeV-madgraph-tauola/Summer12_DR53X-PU_S10_START53_V7C-v1/AODSIM
/SMS-T2bw_2J_mStop-100to475_mLSP-0to375_x-025_TuneZ2star_8TeV-madgraph-tauola/Summer12-START53_V7C_FSIM-v1/AODSIM
/SMS-T2bw_2J_mStop-100to475_mLSP-0to375_x-050_TuneZ2star_8TeV-madgraph-tauola/Summer12-START53_V7C_FSIM-v1/AODSIM
/SMS-T2bw_2J_mStop-100to475_mLSP-0to375_x-075_TuneZ2star_8TeV-madgraph-tauola/Summer12-START53_V7C_FSIM-v1/AODSIM
/SMS-T2bw_2J_mStop-500to800_mLSP-0to700_x-025_TuneZ2star_8TeV-madgraph-tauola/Summer12-START53_V7C_FSIM-v1/AODSIM
/SMS-T2bw_2J_mStop-500to800_mLSP-0to700_x-050_TuneZ2star_8TeV-madgraph-tauola/Summer12-START53_V7C_FSIM-v1/AODSIM
/SMS-T2bw_2J_mStop-500to800_mLSP-0to700_x-075_TuneZ2star_8TeV-madgraph-tauola/Summer12-START53_V7C_FSIM-v1/AODSIM

TABLE C.9: Dataset for the signal MC.

Appendix D

BDT Input Variables

T2bW input variables:

- Missing transverse energy $\not{E}_T$
- Number of jets, reconstructed with anti-k_T with $R = 0.5$
- Number of b-tagged jets of medium quality (”CSV medium working point”)[62]
- Leading quark likelihood of all jets in the event[34]
- Second leading quark likelihood of all jets in the event[34]
- $\prod_{i=1}^{n} jet(quark\ \ likelihood)_i$[34]
- $\frac{\sum(jet(p_T)_i)}{\sum(jet(p_T)_j)}$, $i : |\Delta\phi(\not{E}_T,\ jet_i)| < \frac{\pi}{2}$, $j : |\Delta|phi(\not{E}_T,\ jet_j)| > \frac{\pi}{2}$
- RMS$(p_T(jet))$
- RMS$(p_T(jet) * \Delta\phi(\not{E}_T + \pi,\ jet))$
- Invariant mass of two leading b-tagged jets (CSV medium working point)
- Transverse mass of the b-tagged jet (CSV medium working point) nearest to $\not{E}_T$: $\sqrt{2 * p_T(jet) * \not{E}_T(1 - \cos(\Delta\phi))}$
- RMS$(p_T(jet) * \Delta\eta(b - jet,\ jet))$, where $b - jet$ is a leading b-tagged jet (CSV, medium working point)

- Invariant mass of a pair of jets with highest p_T, all jets are uniquely paired with the nearest neighbor

T2tt input variables:

- Missing transverse energy $\not{E}_T$
- Number of jets, reconstructed with anti-k_T with $R = 0.5$
- $\prod_{i=1}^{n} jet(quark\ \ likelihood)_i$[34]
- Transverse mass of the b-tagged custom "picky" jet nearest to $\not{E}_T$: $\sqrt{2 * p_T(jet) * \not{E}_T(1 - \cos(\Delta\phi))}$
- Location of activity peak in $|\eta|$ of the event
- Distase between two activity peaks in $|\eta|$ in the event
- Number of customly resonstructed top pairs (CORRAL WP98)[16]
- Invariant mass of a reconstructed top pair
- Ratio of p_T of a sub-leading top to leading top: $\frac{p_T(t_2)}{p_T t_1}$
- Area of the ellipse in the $\eta - \phi$ space, covered by top candidates
- $\Delta\phi(\not{E}_T,\ t_2)$
- "Thin quality" of t_2
- "Fat quality" of t_2
- p_T for each of the jets contributing to the top pair candidate
- $Min[\Delta R(jet_i,\ jet_j)]$, i,$j \in t_1$
- $Min[\Delta R(jet_i,\ jet_j)]$, i,$j \in t_2$
- $Min[\Delta\phi(\not{E}_T,\ jet_i)]$, $i \in t_2$

- Maximum discriminator value for ”picky” b-tagged jet for each of the top candidates of a top pair

All top-tag related quantities are calculated for a leading top pair candidate only, with t_1 standing for the top candidate with highest discriminator value.

Appendix E

BDT Input Variables for Lepton Vetos

5.1 Electron and Muon Veto

Variable	e	μ
p_T	✓	✓
d_{xy}	✓	✓
d_z	✓	✓
SIP 3D	✓	✓
Relative PF iso on charged (CHS subtracted)	✓	✓
Relative PF iso on neutral	✓	✓
$\Delta R(l$, nearest-jet)	✓	✓
$p_T^l/p_T^{nearest-jet}$	✓	✓
CSV b-tagged value of nearest b-jet	✓	✓
Fraction of energy lost by Bremsstrahlung	✓	
$\tilde{\chi}^2$ (both KF and GSF tracks)	✓	
Number of tracker layers with measurements	✓	
$\Delta\eta$(super-cluster,track) at vertex	✓	
$\Delta\eta$(super-cluster,track) on calo surface	✓	
$\Delta\phi$(super-cluster,track) at vertex	✓	
$\sigma_{i\eta i\eta}$	✓	
(Super-cluster energy)/momentum (E/p)	✓	
1/E - 1/p	✓	
(electron cluster energy)/(momentum on calo surface)	✓	
(pre-shower)/(raw energy) of the super-cluster	✓	

TABLE E.1: Input variables for the BDT used to veto electrons and muons.

5.2 Tau Veto

Input variables for the BDT used to veto τ:

- p_T of the track;
- $|\eta|$ of the track;
- ΔZ – the distance to the primary vertex; suppresses fake τ;
- Charged isolation: the integral p_T of all charged particles within the cones $\Delta R < 0.1,\ 0.2,\ 0.3,\ 0.4$;
- Total isolation: the integral p_T of all particles within the cones $\Delta R < 0.1,\ 0.2,\ 0.3,\ 0.4$;
- Distance in the $\eta - \phi$ plane to the nearest track with $p_T > 1$ GeV;
- Distance in the $\eta - \phi$ plane to the jet axis; suppresses fake τ;
- CSV b-tag disctiminator of the jet.

Appendix F

MC reweighting: Top, W, Z($\rightarrow \nu\overline{\nu}$) + jets

6.1 Control Regions

$t\bar{t}$

- Muon, which is the only lepton;
- At least three jets in the barrel with $p_T \geq 30\,\text{GeV/c}$;
- At least one tight and two medium tagged b-jets.

W

- Muon, which is the only lepton;
- $m_T(W) \geq 40\,\text{GeV/c}^2$;
- b-tag veto (medium working point) for non-b-specific SFS.

Z

- Two leptons even, same flavor;
- $80\,\text{GeV/c}^2 < m(ll) < 100\,\text{GeV/c}^2$;
- b-tag veto (medium working point) for non-b-specific SFS.

6.2 Scale Factor Sets

Scale Factor Set	Process	Observable	Parameterization
ttSpectrum	$t\bar{t}$	$p_T(l, \not\!\!E_T, closest\ b-tag)$; p_T of the other b-tag; $p_T(l, \not\!\!E_T)$.	p_T of a leading top p_T of the other top
ttNJ	$t\bar{t}$	# of jets: $p_T \geq 30$ GeV/c # of jets: $p_T \geq 70$ GeV/c $p_T(l, \not\!\!E_T)$	# of radiated jets: $p_T \geq 30$ GeV/c # of radiated jets: $p_T \geq 70$ GeV/c p_T of a leading top
zRecoil	Z	# of jets H_T $p_T(l, l)$	# of jets H_T $p_T(Z)$
zNJ	Z (b veto)	# of jets: $p_T \geq 30$ GeV/c # of jets: $p_T \geq 70$ GeV/c $p_T(l, l)$	# of jets: $p_T \geq 30$ GeV/c # of radiated jets: $p_T \geq 70$ GeV/c $p_T(Z)$
zNb	Z	# of jets # of tight b-tags # of med. (non-tight) b-tags $p_T(l, l)$	# of jets # of b-jets # of non-b b-tagged jets $p_T(Z)$
zHTb	Z	# of jets # of medium b-tags H_T $p_T(l, l)$	# of jets # of b-jets H_T $p_T(Z)$
wRecoil	W (b veto)	H_T $p_T(l, \not\!\!E_T)$	H_T $p_T(W)$
wNb	W	# of jets # of tight b-tags # of med. (non-tight) b-tags $p_T(l, \not\!\!E_T)$	# of jets # of b-jets # of non-b b-tagged jets $p_T(W)$
wNJ70	W	# of jets: $p_T \geq 30$ GeV/c # of jets: $p_T \geq 70$ GeV/c $p_T(l, \not\!\!E_T)$	# of jets: $p_T \geq 30$ GeV/c # of jets: $p_T \geq 70$ GeV/c $p_T(W)$

TABLE F.1: Scale factor sets

Bibliography

[1] Fabjan, C. W. et al., , Nucl. Instrum. and Meth., **141**, 61 (1977).

[2] P. Mockett, *A review of the physics and technology of high-energy calorimeter devices*, Proc. 11th SLAC Summer Inst. Part. Phy., July 1983, SLAC Report No. 267 (July 1983), p.42.

[3] N. Akchurin et al., *Hadron and jet detection with a dual-readout calorimeter*, Nucl. Instrum. and Meth. in Phys. Res., **A 537** (2005), 537-561.

[4] S. L Wu, G. Zobernig, *A Method of Three-Jet Analysis in e^+e^- Annihilation*, Z. Phys., **C2**, 107 (1979).

[5] G. Sterman, S. Weinberg, *Jets from Quantum Chromodynamcs*, Phys. Rev. Lett. **39**, 1436 (1977).

[6] G. P. Salam, G. Soyez, *A practical Seedless Infrared-Safe Cone jet algorithm*, JHEP **0705** (2007) 086; **arXiv:**0704.0292.

[7] T. Sj*ö*strand, *The Lund Monte Carlo for e^+e^- jet physics*, Comp. Phys. Commun. **28** (1983) 229.

[8] W. Bartel *et al* [Jade Collaboration], *Experimental Studies on Multi-Jet Production in e^+e^- Annihilation at PETRA Energies*, Z. Phys, C **33** (1986) 23.

[9] S. Catani, Y. L. Dokshitzer, M. Olsson, G. Turnock, B. R. Webber, *New clustering algorithm for multi-jet cross-sections in e^+e^- annihilation*, Phys. Lett. **B269** (1991) 432.

[10] S. Bethke, Z. Kunszt, D. E. Soper, W. J. Stirling, *New jet cluster algorithms: Next-to-leading order QCD and hadronization corrections*, Nucl. Phys. **B370** (1992) 310.

[11] S. D. Ellis, D. E. Soper, *Successive Combination Jet Algorithm For Hadron Collisions*, Phys. Rev. D **48**, 3160 (1993); **arXiv:**9305266.

[12] Yu. L. Dokshitzer, G. D. Leder, S. Moretti, B. R. Webber, *Better Jet Clustering Algorithms*, J. High energy Phys. **8** (1997) 1; **arXiv:**9707323.

[13] M. Wobisch, T. Wengler, *Hadronization Correction to Jet Cross Sections in Deep-Inelastic Scattering*, **arXiv:**9907280.

[14] CMS Collaboration, *A Cambridge-Aachen (C-A) based Jet Algorithm for boosted top-jet tagging*, CMS PAS JME-09-001 (2009).

[15] M. Cacciari, G. P. Salam, G. Soyez, *The Anti-k_T Jet Clustering Algorithm*, JHEP **04** (2008) 063, doi:10.1088/1126-6708/2008/04/063, **arXiv:**0802.1189.

[16] S. A. Koay, T. Medvedeva, C. Tully, *CORRAL: A Comprehensively Optimized Resonance Reconstruction ALgorithm*, **CMS-AN-13-143** (2013).

[17] J. Thaler, K. Tilburg, *Identifying boosted objects with N-subjettiness*, Journal of High Energy Physics, 2011 (2011), No. 3, 1-28.

[18] Web page: linac2.home.cern.ch/linac2/sources/source.htm

[19] M. Benedikt, P. Collier, V. Mertens, J. Poole, K. Schindl, *LHC Design Report, V3, The LHC Injection Chain*, CERN-2004-003.

[20] M. Hone, *The Duoplasmatron Ion Source for the New CERN Linac Preinjector*, CERN/PS/LR 79-37 (1979); C. E. Hill, *Ion and Electron Sources*, CERN Accelerator School 1994, Proceedings pp. 95-112, CERN 96-02.

[21] Edited by S. Gilardoni and D. Manglunki, *Fifty years of the CERN Proton Synchrotron*, volume II, CERN, Geneva, 2013, CERN-2013-005.

[22] K. Hanke, *Past and Present Operation of the CERN PS Booster*, International Journal of Modern Physics A, Vol. 28, No. 13 (2013) 1330019.

[23] K. Hanke, *The PS Booster hits 40*, CERN Courier, Aug 23, 2012: http://cerncourier.com/cws/article/cern/50562.

[24] Edited by S. Gilardoni and D. Manglunki, *Fifty years of the CERN Proton Synchrotron*, volume I, CERN, Geneva, 2011, CERN-2011-004.

[25] Dôme, G., *The SPS acceleration system travelling wave drift-tube structure for the CERN SPS*. CERN report CERN-SPS-ARF-77-11 in proceedings of Proton Linear Accelerator Conference, Chalk River, Canada, 14 - 17 Sep 1976, pp. 138-47.

[26] D. Ramos, *Modeling of the RF-shield sliding contact fingers for the LHC cryogenic beam vacuum interconnects using implicit finite element formulations*. Proceedings of EPAC 08, Genoa, Italy.

[27] Brüning, O. (ed.); Collier, P. (ed.); Lebrun, P. (ed.); Myers, S. (ed.); Ostojic, R. (ed.); Poole, J. (ed.); Proudlock, P. (ed.), *LHC Design Report, V1*. CERN report CERN-2004-003-V-1.

[28] L. Borrello, A. Messineo, E. Focardi, A. Macchiolo, "Sensor design for the CMS Silicon Strip Tracker", *CMS Note* **2003-020** (2002).

[29] CMS Collaboration, *Interpretation of Searches for Supersymmetry*, **CMS-PAS-SUS-11-016** (2013).

[30] ATLAS Collaboration, *Search for squarks and gluinos with the ATLAS detector in final states with jets and missing transverse momentum using 4.7 fb^{-1} of sqrt(s)=7 TeV proton-proton collision data*, **arXiv:**1208.0949.

[31] CDF Collaboration, *Search for Scalar Top Quark Production in $p\overline{p}$ Collisions at $\sqrt{s} = 1.96$ TeV*, **arXiv:**1203.4171.

CDF Collaboration, *Search for Pair Production of Supersymmetric Top Quarks in Dilepton Events from p and anti-p Collsions at $\sqrt{s}$=1.96 TeV*, Phys. Rev. Lett. **104** (2010) 251801, doi:10.1103/PhysRevLett.104.251801, **arXiV:**0912.1308.

D0 Collaboration, *Search for pair production of the scalar top quark in the electron+muon final state*, Phys. Lett. **B 696** (2011) 321-327, doi:10.1016/j.physletb.2010.12.052, **arXiv:**1009.5950.

D0 Collaboration, *Search for pair production of the scalar top quark in muon+tau final states*, Phys. Lett. **B 710** (2012) 578-586, doi:10.1016/j.physletb.2012.03.028, **arXiv:**1202.1978.

ATLAS Collaboration, *Search for supersymmetric partner to the top quark in final states with jets and missing transverse momentum at sqrt(s)=7 TeV with the ATLAS detector*, **arXiv:**1208.1447.

ATLAS Collaboration, *Search for direct top squark pair production in final states with one isolated lepton, jets, and missing transverse momentum in $\sqrt{s}$=7 TeV pp collisions using 4.7 fb-1 of ATLAS data*, **arXiv:**1208.2590.

ATLAS Collaboration, *Search for a heavy top-quark partner in final states with two leptons with the ATLAS detector at the LHC*, **arXiv:**1209.4186.

CMS Collaboration, *Search for Supersymmetry with the Razor Variables at $\sqrt{s}$ = 7 TeV*, **CMS-PAS-SUS-11-016**, (2012).

CMS Collaboration, *Search for supersymmetry in final states with missing transverse energy and 0, 1, 2, or 3 b jets in 7 TeV pp collisions*, **CMS-PAS-SUS-11-022** (2012).

[32] M. Cacciari and G. P. Salam, *Pileup subtraction using jet areas*, Phys. Lett. B **659** (2008) 119-126, doi:10.1016/j.physletb.2007.09.077, **arXiv:**0707.1378v2.

CMS Collaboration, *Determination of Jet Energy Calibration and Transverse Momentum Resolution in CMS*, submitted to JINST (2011), **arXiv:**1107.4277.

[33] T. Hastie, R. Tibshirani, J. Friedman, *The Elements of Statistical Learning. Data Mining, Inference, and Prediction*, 2nd edition, Springler Series in Statistics, Springer (2008).

[34] CMS Collaboration, *Performance of quark/gluon discrimination using pp collision data at* $\sqrt{s} = 8$ *TeV*, CMS PAS JME-13-002 (2013).

[35] A. Adair, B. Akgun, R. Bellan, K. Ecklund, L. Gouskos, J. Incandela, S. A. Koay, S. Lowette, N. MvColl, T. Medvedeva, S. Mullin, P. Padley, R. Rossin, C. Tully, *Scalar Top Quark Search with Jets and Missing Transverse Momentum in pp Collisions at* $\sqrt{s} = 8$ *TeV*, CMS AN AN-13-090.

[36] Web page:

https://twiki.cern.ch/twiki/bin/view/CMSPublic/SWGuideMuonId.

[37] R. Bellan, M. D'Alfonso, J. Incandela, S. A. Koay, S. Lowette, N. McColl, S. Mullin, V. Pavlunin, R. Rossin, *Scalar Top Quark Search with Jets and Missing Transverse Momentum in* pp *Collisions at* $\sqrt{s} = 7$ *TeV*, CMS AN AN-11-498, CMS PAS SUS-11-030.

[38] G. D'Agostini, *A multidimensional unfolding method based on Bayes´ theorem*, Nucl. Instrum. and Meth. in Phys. Res. A**362** (1995), 487-498.

[39] web page:
https://twiki.cern.ch/twiki/bin/view/CMS/EgammaCutBasedIdentfication.

[40] web page:
https://twiki.cern.ch/twiki/bin/view/CMSPublic/SWGuideMuonId.

[41] N. Davidson et al., *Universal Interface of TAUOLA Technical and Physics Documentation*, Comput. Phys. Commun. **183** (2012) 821-843, doi:10.1016/j.cpc.2011.12.009, **arXiv:**1002.0543.

[42] A. L. Read, *Modified frequentist analysis of search results (The* CL_s *method)*, (2000). CERN-OPEN-2000-205.

G. Cowan, K. Cranmer, E. Gross, O. Vitells, *Asymptotic formulae for likelihood-based tests of new physics*, Eur. Phys. J, C71 (2011) 1554, **arXiv:**1007.1727.

web page:
https://twiki.cern.ch/twiki/bin/viewauth/CMS/SWGuideHiggsAnalysisCombinedLimit.

[43] W. Beenakker, R. H*ö*pker, M. Spira, *PROSPINO a program for the PROduction of Supersymmetric Particles In Next-to-leading Order QCD,* **arXiv:**1202.1487.

[44] E. Hazen, J. Rohlf, S. Wu, A. Baden, T. Grassi, *The CMS HCAL data concentrator: A modular, standards-based implementation,* 7th Workshop on Electronics for LHC Experiments,Proceedings p.347-350.

[45] Web page: http://gatignon.web.cern.ch/gatignon/EastAreaUpgradeLS1spec-V3.pdf http://sba.web.cern.ch/sba/BeamsAndAreas/East/East.htm

[46] J. Wenninger, *Introduction to Slow Extraction to the North Targets,* http://jwenning.home.cern.ch/jwenning/documents/TrainingOP/Training-Slow-2007.ppt (April 2007).

[47] P. Grafström, Web page:
http://sba.web.cern.ch/sba/Documentations/Target/T2/T2_multi_purpose.pdf

[48] Web page:

http://sba.web.cern.ch/sba/BeamsAndAreas/H2/h2fm06.pdf

[49] Web page: http://eagroup.home.cern.ch/eagroup/EAbeatch.html

[50] Web page:

https://wikis.cern.ch/pages/viewpage.action?pageId=14942273

[51] Web page:

http://gatignon.web.cern.ch/gatignon/partprod.html

[52] Web page:

http://abwww.cern.ch/ap/dist/cesar/cesar-t4wobbling/PRO/WobblingConfig EditorGui.jnlp

[53] Web page:

https://espace.cern.ch/sba-workspace/EHN1%20%20H2%20H4%20H6%20H8/Forms/AllPages.aspx

[54] Web page:

http://slwww.cern.ch/ pcrops/releaseinfo/pcropsdist/cesar/cesar-wobbling/PRO/WobblingConfigManager.jnlp

[55] Web page:

http://slwww.cern.ch/ pcrops/releaseinfo/pcropsdist/cesar/cesar-app-ea/PRO/BlAndCurrentConversion.jnlp

[56] M. Lucchini, T. Medvedeva, K. Pauwels, C. Tully, A. Heering, C. Dujardin, K. Lebbou, P. Lecoq, E. Auffray *Test beam results with LuAG fibers for next-generation calorimeters*, JINST, **8**, P10017 (2013).

[57] E. Hazen, J. Rohlf, S. Wu, A. Baden, T. Grassi *The CMS HCAL data concentrator: A modular, standards-based implementation*, 7th Workshop on Electronics for LHC Experiments, Proceedings p.347-350.

[58] G. Mavromanolakis, E. Auffray, P. Lecoq *Studies on sampling and homogenous dual readout calorimetry with meta-crystals*, JINST, **6**, P10012 (2011).

[59] GEANT4 collaboration, S. Agostinelli et al., *GEANT4: A simulation toolkit*, Nucl. Instrum. Meth. **A 506**, 250 (2003).

[60] M. Hoek et al., *Radiation hardness study on fused silica*, Nucl. Instrum. Methods Phys. Res., **A 595**, 190 (2008).

Web page:

http://nuclear.gla.ac.uk/ mhoek/talks/2007/mhoek_rich07.pdf

[61] Web page: http://www.technicalglass.com

[62] CMS Collaboration, *Identification of b-quark jets with the CMS experiment*, submitted to the Journal of Instrumentation, CERN-PH-EP/2012-262, CMS-BTV-12-001, **arXiv:**1211.4462.